On the evolution of star forming galaxies:

the metallicity of dwarfs and the effect of environment on local luminous IR galaxies

Abiy G. Tekola

Supervisors:
A/Prof Patrick Woudt (UCT)
Dr. Petri Väisänen (SAAO[1])
Dr. Alexei Kniazev (SAAO)

Submitted in total fulfilment of the requirements
of the Degree of Doctor of Philosophy

May, 2011

Department of Astronomy
University of Cape Town (UCT)

[1]South African Astronomical Observatory

Declaration

I know the meaning of plagiarism and declare that all of the work in the dissertation (or thesis), save for that which is properly acknowledged, is my own.

Dedication

This work is dedicated to millions of Africans who have the potential and the talent but not the opportunity to pursue their dream.

Acknowledgement

I would like to thank Dr. Petri Väisänen, my main supervisor, first of all for introducing me to this fascinating science and then leading me to the successful completion of this work. In fact, Petri was not only my supervisor but also a good friend during the last four years. This PhD work would not have been possible without his constant encouragement, support, continuous follow up, and life-enriching and unforgettable advice from his wealth of experience. I learned from him what it means to have a balanced life. I also want to thank Petri's wife Minna and his four kids for the good and enjoyable time I have spent with them during the past four years.

I take this opportunity to give a well-deserved and special thanks to A/Professor Andreas Berlind, my co-supervisor at Vanderbilt University. Andreas's willingness to be my co-supervisor and hosting me at Vanderbilt for one year led me to the most interesting adventure of my life in extragalactic astronomy (understanding of the environments of galaxies). His guidance, patience and words of encouragement made this work a reality. Even after I returned from Vanderbilt, Andreas was always willing to advise me, reading my thesis and papers despite his time constraints.

Dr. Alexei Kniazev, also my co-supervisor, is acknowledged for his support, guidance and of course his sense of humour. I thank him especially for his time to read my chapters within a very short period of time and giving me very valuable suggestions. I have learned a lot from all our discussions and conversations.

I would like to express my appreciation to A/Prof Patrick Woudt's willingness to be my UCT official supervisor, for reading my final thesis chapters, advising and facilitating my submission and corrections even after the examination process of the thesis.

My appreciation goes to my three unanimous thesis examiners who were willing to spend their precious time reading this thesis and make their comments in time. Their comments, suggestions and criticism improved the quality of this thesis very much.

I would like to take this opportunity to thank the entire astronomy research group and the Bridge community at Vanderbilt for their warm reception and hospitality during my one year visit there. I want to single out Alyce Dobyns for making my stay in Nashville a pleasant and memorable experience and a life without hassle.

Fellow country men and good friends Getachew Mekonnen and Amare Abebe deserve my words of appreciation for being next to me especially during the last two very difficult weeks of finishing this thesis and helping in proofreading the chapters. Fellow students: Paul Kotze, Ewald Zietsman, Ihab Riyad, Deatrick Foster, Marissa Kotze and the entire Malagasy community: Ander,

Ando, Zara and Solohery have been of great support during this PhD work and I would like to say thank you very much to them.

I would like also to thank the entire SAAO staff (the astronomers, the IT crowd, the administration, the SALT guys). Working together, all these people made the observatory a very suitable and convenient place for students. My four years stay at SAAO remains as one of the most enjoyable and memorable time of my life. I would specifically like to name some people whose encouragement, support and friendship was very important for me during this work: Professor Patricia Whitelock, Mr. Kevin Govender, Dr. David Buckley, Dr. Christian Hettlage and Dr. Bonita De Swardt. I would like to say thank you to them.

Most importantly, I would like to acknowledge the support I got during this PhD from NASSP and the people in NASSP (Professor Peter Dunsby, Penny Middelkoop, Nicky Walker). You guys have been doing a great work through NASSP and here is now one of your fruit! I would like to acknowledge grants from Ford Foundation through NASSP[2], NRF[3], IAU[4], AGAP[5], Multi-wavelength grant, SAAO , Vanderbilt University and VIDA[6].

My fellow Ethiopian friends here in Cape Town, Nashville and Ethiopia [7]deserve a special words of appreciation. I feel I was protected with their company and presence around me. They are great friends! I wonder how many times they organized a fare-well party for me but only to see me back in Cape Town in few months time. Now that I am leaving UCT for good, can I have one more party please?

The encouragement, love, prayers and support I got from my family and my wife's family was indeed very instrumental during the last four years. You guys are always in my heart.

I want to say thanks to Abigya (Abigail), my wife. Her unconditional love and support during these four difficult years were my power house to push forward. Especially when I was approaching the finish line and things got really difficult, her encouragement and prayers kept me going strong. This PhD would have been impossible without her patience to wait for me this long away from her. She is indeed an excellent wife!

Last but not least, I thank the one who created this Universe, including me and the galax-

[2]National Astrophysics and Space Science
[3]National Research Foundation
[4]International Astronomical Union
[5]Astronomy for Geographical Advantage Program
[6]Vanderbilt Initiative in Data-intensive Astrophysics
[7]They are too many to name all but Kaleab made a special request so that his name appears in this thesis somehow, so here you go Kaleab at least you are in the footnote

ies I study. I have learned that He is beyond my wildest imagination! I am grateful for all his provisions in life including families and friends.

Abiy G. Tekola

Abstract

This thesis, entitled "*On evolution of star forming galaxies: the metallicity of dwarfs and the effect of environment on local luminous infrared galaxies*" is divided into two main areas. First a detailed study of the environment and star formation relationship of local Luminous Infrared Galaxies (LIRGs), with infrared (IR) luminosity (L_{IR}) between $10^{11}L_{\odot}$ and $10^{11}L_{\odot}$, where $L_{\odot}$ is solar luminosity was carried out. Secondly, a chemical abundance analysis was done on three Local Volume dwarf irregular galaxies.

In the first part, various redshift surveys were used to quantify the environment around LIRGs. It was found that $L_{IR} \sim 10^{11}L_{\odot}$ is a remarkable luminosity point among IR galaxies. Above this level, the IR luminosity of galaxies increases monotonically with their environment. On the other hand, IR galaxies whose $L_{IR} \leq 10^{11}L_{\odot}$ show no dependence of star formation on environment. These latter galaxies live in an environment similar to a transition between field and group while LIRGs live in group environment. The environment scale we studied was 2 Mpc which means that the star formation of LIRGs is affected not only by their immediate surroundings but also by the larger scale.

It was found that local LIRGs exhibit a similar star formation-density relationship with that found in many studies of high redshift star forming galaxies. This suggests that local luminous LIRGs could be the remnant of a process that transformed high redshift star forming galaxies into the present day gas-poor and non-star forming galaxies.

The dark matter haloes of galaxy systems the luminous infrared galaxies are associated with were also used to quantify their environment. It was found that the low-L_{IR} LIRGs are slightly more likely to live in an environment which is between field and group. Given the star formation-density correlation found above, the result is consistent with what is found when the density is quantified using number counts of galaxies.

Moreover, the dark matter halo study of the LIRGs suggested that those galaxies that live close to the centre of the group haloes form stars at higher rates than those that are far out from the centre. This result is in agreement with the star formation-environment correlation in group size environments in the local Universe.

In the second part of the thesis, a small size spectroscopic data set of dwarf irregular galaxies was studied. The data were acquired with the Southern African Large Telescope with the main objective of calculating the chemical abundances and extinction information of the galaxies. The metallicity and associated temperature and electron densities were calculated using a direct method based on a number of detected optical lines. The results were compared to the

known metallicity-luminosity relationship of dwarf irregular galaxies. Two of the galaxies fit the relation very well. However, one of the galaxies deviates considerably, and it was suggested that this galaxy, though it is a dwarf irregular, could have a different star formation history for various reasons. The metallicity gradient was also investigated for this particular galaxy and it was found that there is a declining gradient similar to spiral galaxies. This study is considered as a pilot project for a future spectroscopic survey of star forming galaxies using the Southern African Large Telescope, and the results found to be very encouraging.

20^{th} of May, 2011

Abiy G. Tekola

Contents

List of Tables

List of Figures

1 Introduction

1.1 The Expanding Universe and growth of structure

Since the pioneering work of Edwin Hubble in 1929, it has been known that the Universe is expanding. Hubble used a few galaxies from the local Universe to show that galaxies move away from us with a speed proportional to their distance: $V = Hd$, where H is Hubble's constant, V is the speed of recession and d is the distance from us. One implication of Hubble's finding is that galaxies were closer to each other in the past than they are now. This in turn suggests a time when all of them were together in the distant past and that, according to the most favored theory of the birth of the Universe, marks the beginning of space-time, i.e. the Big-Bang. The discussion below in this Section follows the treatment by Sparke & Gallagher (2007) & Peacock (2002).

The evolution of the Universe since the Big-Bang was governed by the relative importance of matter and radiation energy densities. At the early time of the birth of the Universe, the former scaled as $\rho_m = a^{-3}$ and the later as $\rho_r = a^{-4}$, where a is a scale factor. During this period, the Universe was extremely hot and dominated by radiation pressure. As time went on, however, the expansion progressed and, since matter density decreases more slowly than radiation density, at about 1 million years after Big-Bang, the matter energy density became more important than the radiation energy density and the Universe became matter dominated.

Everything that we see in the present Universe originated from small density fluctuations arising from quantum fluctuations in the otherwise homogeneous and smooth early Universe at the Big-Bang. These density fluctuations grew up, due to gravitational instabilities, to form

various complex structures such as galaxies, clusters and walls as the Universe expanded. Slightly overdense regions attract matter from their surrounding and grow slowly. These overdensities are described by a density contrast, $\delta(x)$, defined relative to the mean density of the Universe, ρ_o, and the actual density of the fluctuation, $\rho(x)$, as:

$$\delta(x) = \frac{\rho(x)}{\rho_o} - 1. \tag{1.1}$$

In a very simplistic approach, the growth of the initial density contrast of matter to form large scale structures is heavily dependent on the relative strength of the effect between gravitational pull of the matter itself and radiation pressure. The physical size of the gravitating structure must be greater than a certain characteristic length called Jeans length, λ_J, in order for it to be gravitationally unstable and start to collapse. The size of λ_J is normally given as:

$$\lambda_J = c_s \sqrt{\frac{\pi}{G\rho}}, \tag{1.2}$$

where c_s is sound speed, ρ is density and G is gravitational constant. The corresponding mass, M, inside λ_J is given as:

$$M_J = \frac{\pi}{6} \lambda_J^3 \rho_m. \tag{1.3}$$

Depending on the relative importance of radiation and matter at the different epochs of the Universe (expansion phase of the Universe), both the λ_J and M_J scale differently. This in turn dictates what size of density fluctuations can collapse and grow to form bigger size structures and what size of density fluctuations die off. For example, in the early radiation-dominated period of the Universe, λ_J and ρ_m scale as a function of a^2 and a^{-3} respectively and hence the Jeans mass grows as a^3.

Among the different competing theories to explain the growth of structures in the Universe, Λ cold dark matter (ΛCDM) is the most accepted and successful theory. This theory is entirely based on non-relativistically moving (the reason for the name "cold") dark matter particles and also incorporates the accelerating expansion of the Universe in it (the reason for the Λ prefix).

The formation of gravitationally bound dark matter systems called *haloes* precede the growing and collapse of baryonic matter into galaxies (White & Rees 1978). Dark matter haloes are formed when the initial small scale fluctuations grow and undergo violent relaxation and virialization to finally form a bound and well-settled system. The physical size (radius) of these haloes is determined by the virialization process that they undergo (Efstathiou & Silk 1983, White & Rees 1978). The physical boundary of virialized haloes is an iso-density surface in which the density is nearly 200 times that of the critical density of the Universe and the radius at which this happens is called the virial radius, R_{vir}. This is because a spherical region gets virialized when its mean enclosed density is about 200 times the mean density of the universe

(see the spherical collapse model by Gunn & Gott 1972) . The virial radius in terms of the mean density and the halo mass can then be simply worked out to be

$$R_{vir} = (\frac{3}{4\pi}\frac{M_{virial}}{200\bar{\rho}})^{1/3}, \tag{1.4}$$

where M_{virial} is the virial mass and $\bar{\rho}$ is the mean density of the Universe.

In the context of ΛCDM, it is in these haloes, whose physical size is determined by Equation 1.4, that galaxies are formed from baryonic matter and evolve (Ostriker et al. 1974) immediately after matter is decoupled from radiation. As gas (baryonic matter) collapses inside dark matter haloes, much of the potential energy released during the process is radiated and the gas cools. This cooled gas sinks towards the centre of the potential well of the dark matter halo and eventually turns into stars in the core of haloes (White & Frenk 1991). The centre of the halo is therefore dominated by baryonic matter even though the total halo is dominated by non-baryonic matter.

As time goes on, dark matter haloes containing galaxies are hierarchically and gradually merging to form more complex systems like groups, clusters and walls (White & Rees 1978). It is believed that this merging and interaction of haloes with other haloes plays a crucial role in shaping the various properties of galaxies, for example their star formation (SF) properties and perhaps their morphology. Regarding the latter, it is still not, however, clear whether the morphology they have is something they acquired at their birth (nature scenario) or it is something they acquired as time went on through various processes shaped (nurture scenario) (see e.g. White 1983).

1.2 Galaxy classification and the Hubble diagram

Galaxies appear to have different types of morphologies. From visual inspection, one can tell that some galaxies are featureless and elliptical, some are disky with spiral arms and others are irregular or peculiar. Based on these features, Edwin Hubble classified galaxies for the first time into different classes and this classification is referred to as the Hubble sequence or the Hubble tuning-fork diagram (see Fig 1.1) (Hubble 1926; 1936).

The Hubble scheme of galaxy classification is completely based on morphology and it has four broad classes, i.e. ellipticals, spirals, lenticulars, and a class of galaxies called irregulars that do not fit into any of the three major classes.

- *Elliptical*: these are galaxies with almost smooth and elliptical isophotes. They are divided in to subclasses E0, E1, E2, etc...depending on their ellipticity; as the number after "E" grows, they progressively get more elongated.

- *Spirals*: these are galaxies with a disk and spiral arms. Depending on the existence of a bar-like structure at their centre, they are divided into barred (SB) and unbarred spirals

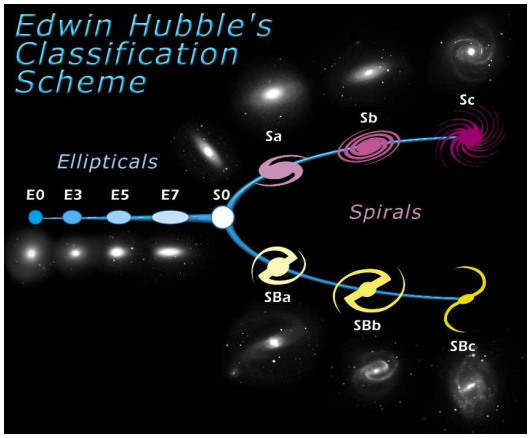

Figure 1.1: A schematic representation of the Hubble sequence of galaxy classification (Hubble's tuning-fork diagram).

(S). In each of these two subclasses, spirals are further divided in to SBa, SBb, SBc (the barred ones) and Sa, Sb, Sc (the unbarred ones). This classification is based on the fraction of the light at the centre and the tightness with which the spiral arms are wound.

- *Lenticulars*: these are galaxies that are intermediate between ellipticals and spirals. They have a smooth light distribution like ellipticals and also have a disk like spirals but no spiral arms.

- *Irregulars*: these galaxies have neither a disk nor a bulge and are not considered to be part of the above three classes. Generally they appear patchy and dominated by HII regions and they include star-burst galaxies such as the very dusty and luminous infrared galaxies. Though they were not included in the original Hubble's classification, these days they are often included at the end of the spiral sequence.

Ellipticals and lenticulars are usually referred to as early-type galaxies whereas spirals and irregulars are referred to as late-type galaxies. Although the majority of galaxies fall under the classification scheme of Hubble, there are some with completely different morphologies that do not fit anywhere. Interacting and merging galaxies fall under this class.

It seems that many of galaxy properties including their spectral energy distribution (SED), colour, luminosity, gas content, environment and metallicity appear to show a systematic change along the Hubble sequence (Holmberg 1958). In Figure 1.2, we present the systematic change of the SED along the Hubble sequence. One can note that there is indeed a correlation between the spectral and morphological type. The blue part of the spectrum gets stronger and stronger from the early-type ellipticals to the late-type spirals to the star-bursts. On the other, hand along the same sequence, the red spectral end gets weaker and weaker. The light in the late-type

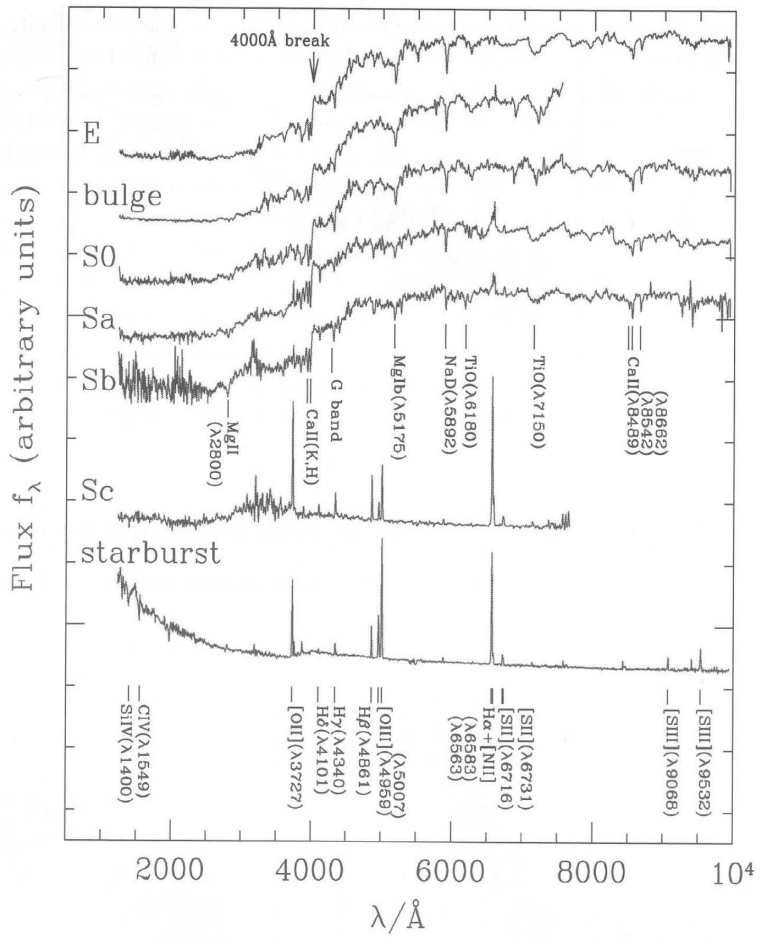

Figure 1.2: Spectra of different types of galaxies from the ultraviolet to the near-infrared. The SED change systematically as one goes from ellipticals to spirals to star-bursts (adopted from Mo et al. (2010)).

spirals and star-bursts are emitted mainly by young hot stars whereas in the elliptical case, it is emitted by the old stars.

Moreover, the redder early-type galaxies tend to be very luminous while the bluer late-type ones are less luminous. When it comes to their environment, early-type galaxies seems to dwell in denser environments (such as clusters) than the late-type ones (Dressler 1980). In terms of the metallicity content (O/H), it appears that late-type galaxies are less abundant in metals than early-type galaxies (Roberts & Haynes 1994). In Figure 1.3, we show how the metallicity changes along the Hubble sequence.

Though Hubble originally thought that his classification scheme might also show an evolu-

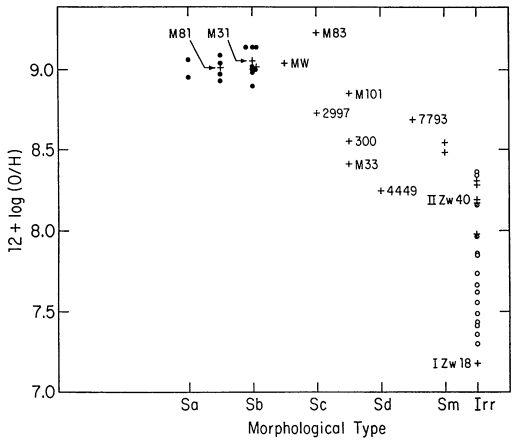

Figure 1.3: The metallicity of galaxies follows the Hubble sequence. The metallicity is represented by the oxygen abundance relative to hydrogen (O/H) (adopted from Roberts & Haynes (1994)).

tionary sequence, evolution along the sequence from early-type ellipticals to late type spirals and star-bursts does not seem physically possible. On the other hand, evolutionary sequences the other way around seem generally possible. For example, late-type gas-rich spirals turning to early-type ellipticals through a violent phase of star-bust (very luminous inrared galaxies) because of merging is both theoretically and observationally supported (Toomre & Toomre 1972).

Galaxy evolution and transformation from one Hubble type to another is driven by various processes that originate both from inside of individual galaxies and from their surrounding environments. These processes include SF processes (secular evolution), chemical evolution, interactions and merging with other galaxies. In this chapter, we will review briefly two of these factors: environmental and chemical effects. In the first case we will give a general description of the different types of environmental effects and then we discuss one of the two main objectives of this work which is the SF property of luminous infrared galaxies in connection to environment. We will then shift to the chemical evolution of galaxies and we discuss it in the context of dwarf irregular galaxies which are the other subject of this work.

1.3 Galaxy environment

The “environment” of a galaxy can have different definitions according to the context it is used. However, all the working definitions eventually agree that the issue is related to the mass distribution around a galaxy. Some galaxies live in isolation without significant effect of others and such galaxies are referred to as living in "field environment". Others live with a relatively small number of galaxies bound gravitationally and this is termed as "group environment"

whereas others live in a very dense environment bound together gravitationally and such an environment is referred to as "cluster environment".

When galaxies live together in the same potential well, they interact gravitationally with their neighbours and affect each other. The interaction results in the redistribution of their gas, changing internal structures, mass loss and even merging depending on various parameters of the interacting galaxies. Different observational evidences confirm that different aspects of galaxy formation, transformation and evolution processes are at least partially driven by interactions galaxies have with their neighbours (see, e.g. Joseph 1989, Dressler 1980, Moore et al. 1996, Mihos & Hernquist 1996, Trentham & Mobasher 1998).

The interaction of galaxies is mainly driven by two mechanisms: dynamical friction and tidal forces. Dynamical friction is normally a gravitational drag when galaxies move near another galaxy (see discussion in Mihos 2004, Mo et al. 2010). In the process, galaxies lose their momentum and kinetic energy and they get closer and eventually merge. Tidal stripping, on the other hand, represents the unequal gravitational force experienced by different parts of a galaxy. During this process, that part of the galaxy that felt the maximum force will be stripped off its gas and stellar content (see the the different tidal features during the interaction of two gas-rich galaxies in Figure 1.4). Below we discuss some of the most important environmental factors that give rise to evolution and transformation of galaxies by either fueling or shutting off SF.

1.3.1 Galaxy harassment

In an environment where galaxies are populated very densely (cluster environment), the typical velocity dispersion of stars and the interstellar medium (ISM) inside a galaxy is much smaller than the typical velocity of the galaxies themselves ($\sim 1000\ km\ s^{-1}$). Most interactions are fly-by interactions that leave the internal gas content of the interacting galaxies unbound, fragile and more vulnerable to disruptions, even when such a disruption does not happen in the first interaction. Any subsequent interactions of such galaxies would result in a complete disruption and shutdown of SF (Farouki & Shapiro 1981, Richstone 1976).

1.3.2 Ram-pressure stripping

When a gas-rich galaxy moves in the intracluster medium (ICM), the galaxy experiences a shock-wave generated by the medium. The galaxy as a result feels a strong drag by the shock wave. The consequence of this process is the stripping of the gas content of the galaxy and shutting down of any on-going SF in the galaxy (Gunn & Gott 1972). This explains why cluster environments are often short of gas-rich star forming galaxies.

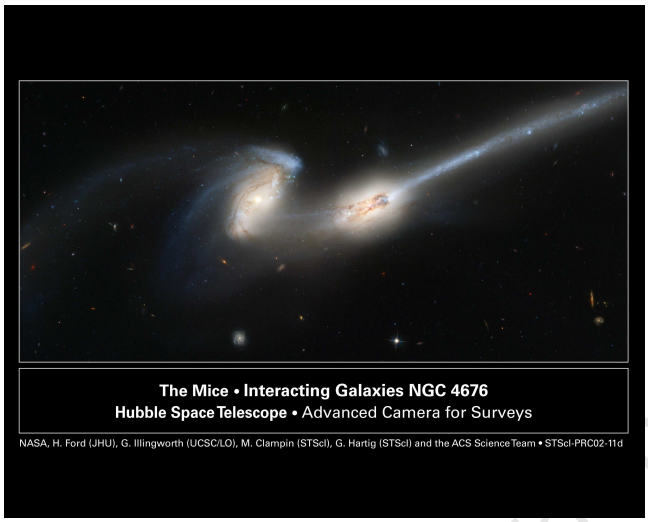

Figure 1.4: NGC 4676 is an interacting system between two gas-rich galaxies. All the tidal features seen in the image are indications for the interaction. (courtesy of Hubble images).

1.3.3 Galactic cannibalism

Most big galaxies have satellite galaxies moving around them in a bound orbit. As satellite galaxies move around the central galaxy, due to dynamical friction, the orbit decays and stars are stripped off from the outer part of the satellite galaxy. As this process continues, the satellite galaxy will be disrupted completely (Richstone 1976). Galactic cannibalism often does not result in any morphological change in the central galaxy.

1.3.4 Merging

Merging is by far the most effective mechanism of galaxy transformation and evolution. In the hierarchical scenario of structure formation, it plays a crucial role in the assembly of galaxies and dark matter haloes. At least some of the present day ellipticals are, for example, believed to be formed through merger processes involving gas-rich spirals (Toomre & Toomre 1972).

Merging is defined as the complete merging of two or more galaxies to form one galaxy. Merging galaxies must have a relatively small velocity dispersion ($< 500\ km\,s^{-1}$) because dynamical friction (the driving force of merging) scales as the inverse of the dispersion velocity v^{-2} (Binney & Tremaine 1987). As a result merging is more efficient in group environments, where the velocity dispersion is of the order of 500 $km\,s^{-1}$ or less, than in clusters where the dispersion velocities are in the order of 1000 $km\,s^{-1}$ or even more.

Merging is an efficient mechanism for intense SF seen in the Universe. Merger studies between two gas-rich disk galaxies using numerical simulations have demonstrated that during the process of merging, the disks of the galaxies become very unstable and develop bars (Noguchi & Ishibashi

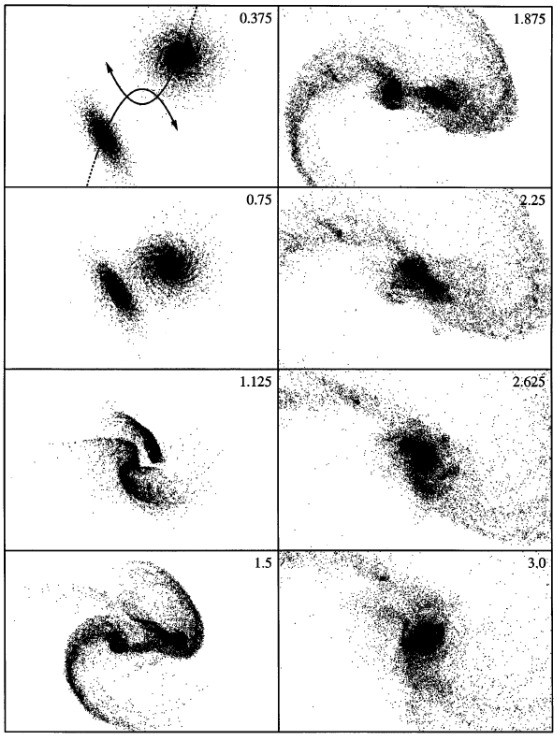

Figure 1.5: Evolution of the gas distribution in the merger of two gas-rich disk galaxies projected onto the orbital plane, as simulated by Barnes & Hernquist (1996).

1986, Barnes & Hernquist 1996). The bar and the gaseous component respond differently to the tidal interaction and will have different phases. Later, this phase difference results in a torque that removes angular momentum from the gas and pushes it to the central region of the merger remnant. Subsequently, at the central region there will be a large concentration of gas (Negroponte & White 1983). According to the Kennicutt-Schmidt law (see Chapter 2 Section 2.6.5 for a brief explanation of it), the surface density of the gas in the central region is enough to give rise to intense SF. Figure 1.5 shows different stages of the interaction between two gas-rich disk galaxies.

In the case where the central gas loses further angular momentum, the gas flows even further very close to the centre and might result in a localised star-burst (Mihos & Hernquist 1994; 1996), and/or the growth of black holes, creating intense nuclear activity (Debuhr et al. 2010).

Mergers do not always result in intense SF and their response depends on the different interaction parameters such as the velocity and mass of the progenitors (see discussions in Mihos 2004, Mo et al. 2010). If the masses of the merging galaxies are close to equal ($m/M \approx 1$) the merger is strong (such a merger is called a *major merger*) while if m/M$<$0.3, the interaction is essentially similar to galactic cannibalism and the effect on the bigger component is very mild

(such a merger is called a *minor merger*) (Mihos 2004). Major galaxy mergers in many cases result in transforming the morphology and other properties of both or all of the interacting galaxies. The outcome of a merger also depends on how strong the merger is. A strong merger between two gas-rich galaxies could lose most of the system's gas at the first stage of the interaction and the gas might not be reacquired at the final stage to fuel up SF (Di Matteo et al. 2007). It is also known that the efficiency of merger-driven SF is dependent on the type of environment in which the merger system is taking place. A major merger is twice or more efficient in initiating SF if it takes place in the tidal field of a group or a cluster (Martig & Bournaud 2008).

1.3.5 Local density measurement

There are various ways of quantifying the local density of galaxies (Cooper et al. 2005). These include group or cluster membership, distance to nearest cluster, void membership, distance to N^{th} nearest neighbour and number count in a metric aperture. The first three methods are sensitive to the large scale environment of galaxies while the last two are sensitive to local environments in the range between 1 to 5 Mpc. A detailed description of the common methods of estimating galaxy density can be found in Cooper et al. (2005). Below, potential biases and how they influence density measurements are discussed.

Redshift space distortion

Redshift space distortion biases density estimation of galaxy environment by affecting proper distance measurements from cosmological redshift. Normally, redshift measurements are not distance measurements. They are velocity measurements but they can be converted to distance. The conversion, however, is not straightforward because of the existence of peculiar velocity of galaxies. At relatively low redshift, a galaxy with redshift z and peculiar velocity, $\boldsymbol{v}_r$ has its distance d given as:

$$d = cz/H_o + \boldsymbol{v}_r/H_o, \tag{1.5}$$

where c is speed of light, H_o is the present cosmological constant.

The effect of peculiar velocity is either to add or to subtract from the cosmological velocity of galaxies. Consequently, the distribution of galaxies in redshift Universe shows a "distortion" as compared to their true distribution in three dimensional space. Groups of galaxies appear to be stretched radially resulting in the so called "fingers of God" effect. The effect of peculiar motion of galaxies is very high in dense regions such as groups ($\boldsymbol{v}_r \sim 500\ kms^{-1}$) and clusters ($\boldsymbol{v}_r \sim 1000\ kms^{-1}$) and also in low redshift Universe where the cosmological recession is very low. Since most redshift surveys are shallow and subject to significant redshift space distortion, it is important to account for such effects while using redshift as a measure of distance.

A cylindrical metric aperture oriented in the line-of-sight direction deals with redshift space distortion effects much better than any of the other density estimation techniques such as the n^{th}-nearest neighbour Distance. Since the maximum effect of redshift space distortion is felt in cluster environments ($\bar{v}_r \sim 1000\ km\ s^{-1}$) where galaxies move with higher peculiar velocity than in poor environment, an allowance of $\pm 1000\ km\ s^{-1}$ or more from the centre of the cylinder reduces the maximum effect caused.

Survey edge effects

The other issue that potentially biases galaxy density estimation is survey edge. Generally, density estimates near the edge of a survey measure an apparent under-density in case the apertures do not entirely fall inside the survey volume. This effect is even worse at higher redshift end of surveys as the size of the survey edge grows with redshift. While small size apertures generally reduce edge effects, it is also possible to reduce the problem to some extent using other methods.

One way of avoiding edge effects is to remove galaxies very near the edge of a survey. If, however, this would reduce the number of galaxies considerably (which is the case especially for the bright galaxies that are found at high redshift near the survey edge in a flux limited sample), it is also possible to avoid the effect by scaling the estimated density measure.

Redshift dependent incompleteness

In any survey (flux or volume limited survey), the fraction of galaxies declines with redshift even above the limiting magnitude at each redshift and this introduces redshift dependent incompleteness Cooper et al. (2005). As a result, galaxies at higher redshift appear to be at a lower density environment than those at low redshift. In the case of volume-limited surveys, the effect becomes important only when the redshift range is quite big. Otherwise, it can be neglected without resulting in any noticeable consequences.

It is common to avoid these kinds of effects by selecting a volume limited sub-sample which includes everything above a certain luminosity limit and below a certain redshift. However, this reduces the number of sources included in the sub-sample considerably especially if the volume limited sample is made at higher redshift which is the case in this work. In such cases, it is still possible to make use of the entire sample (flux or volume limited) with a correction for the redshift dependent incompleteness (see for example Blanton et al. 2003, Cooper et al. 2005).

Correcting for redshift dependent selection effects and edge effects

Generally, for any given survey subject to redshift dependent incompleteness effect, the corrected density estimate per volume ($X_0(\alpha, \delta, z)$) can be presented as:

$$X_0(\alpha, \delta, z) = \frac{X_z(\alpha, \delta, z)}{s(z)w(\alpha, \delta)}, \tag{1.6}$$

where $X_z(\alpha, \delta, z)$ is the observed number count per volume, $s(z)$ is a selection function that accounts for the redshift dependent incompleteness and $w(\alpha, \delta)$ is a factor that accounts for the incompleteness from field to field. The latter incompleteness effect is a function of declination and right ascension and is usually negligible. The above equation is then rewritten without the $w(\alpha, \delta)$ term as

$$X_0(z) = \frac{X_z(z)}{s(z)}. \tag{1.7}$$

Ideally, $s(z)$ can be determined from the redshift evolution of the luminosity function of the galaxies in the survey to estimate the theoretical number count of galaxies at a certain luminosity and redshift. In practice, however, it is very difficult to estimate the redshift evolution of luminosity functions especially at higher redshift as any observations at higher redshift are often limited to brighter objects.

Alternatively, $s(z)$ can also be estimated based on a distribution of points in space that have the same redshift distribution with the real galaxies but no clustering nature at all unlike the real galaxies. It is, however, important to note that this approach deals with the incompleteness only above the magnitude (luminosity) limit at each redshift of a given sample.

Having said this much about quantifying galaxy environment with a number count of individual galaxies, we return to the very essential definition of "environment of galaxies" that we presented at the very start of our discussion. It is mentioned that the environment of galaxies refers to the overall mass concentration around a given galaxy. Therefore, with clear understanding of the overall dynamical mass concentration around galaxies, one can also characterise the environments of galaxies.

1.4 Dark matter and environment

With the assumption of Newtonian gravity, the rotational velocity profile of spiral galaxies indicates that there must be a big fraction of mass that cannot be seen but interacts only gravitationally with its surrounding environment (Roberts & Rots 1973, Rubin et al. 1978). This mysterious mass exists in a form of matter completely different from the ordinary matter from which luminous bodies such as stars, galaxies, etc. are formed. Most of the matter in the Universe is in this mysterious form of matter. It dominates the total matter content of the Universe by contributing about 80% of it. Ordinary matter (stars, galaxies, etc.) contribute only 20% of the total mater content of the Universe (Spergel et al. 2007).

The size of the dark matter halo of galaxies correlates with their various properties through the dependence of galaxy properties with their environment. More massive haloes host more

galaxies than smaller size haloes. This means the size of the dark matter halo is correlated with the number of galaxies (environment inside the halo) it contains. As a result, a galaxy living in a high mass halo is living in a denser environment than a galaxy living in a smaller size halo. This in turn means that measuring galaxy density around galaxies, to some extent, at least means measuring the mass of the underlying dark matter halo (Berlind et al. 2005). However, this is not completely true because there is a bias between the dynamical mass and luminous mass of the Universe.

1.4.1 Mass bias

The fact that different galaxies cluster differently implies that different galaxies trace the underlying dynamical mass not in exactly the same way. This difference seems to be colour and luminosity dependent (Loveday et al. 1995, Hermit et al. 1996). Differently selected galaxies therefore show different mass bias. For example, red and "dead" elliptical galaxies trace the mass better than the active blue galaxies (Dressler 1980).

In terms of the galaxy and dark matter (dynamical mass) density fluctuation terms, the bias parameter, b, is given as:

$$\delta_g(X) = b^2 \delta_m(X), \tag{1.8}$$

where $\delta_g(X)$ is the galaxy density fluctuation term and $\delta_m(X)$ is the galaxy density fluctuation term. The existence of mass bias is one of the stumbling-blocks in reconciling theoretical results with observational results concerning any physical property of galaxies related to their underlying dark matter mass.

1.5 Luminous Infrared Galaxies

Luminous Infrared Galaxies (LIRGs) are galaxies with $10^{11} L_{\odot} \leq L_{(8-1000)\mu m} \leq 10^{12} L_{\odot}$, where $L_{(8-1000)\mu m}$ is the far-infrared luminosity (Sanders & Mirabel 1996). Hereafter, we refer to this luminosity as L_{IR}. Their far-infrared energy output represents the bulk of their total energy and sometimes it even reaches as much as 99% of their bolometric luminosity (Example Arp 220=IC 453 (Soifer et al. 1984)). The source of this enormous IR energy is dust enshrouded circumnuclear SF together with a varying active galactic nuclei (AGN) contribution especially at higher L_{IR} values (see Section 1.5.4 for brief discussion about AGN).

1.5.1 Historical background of LIRGs

While the contribution of the Infrared Astronomical Observatory (IRAS) [1] in revolutionising the understanding of the infrared (IR) activity of extragalactic sources is not questioned, the first observations of IR sources trace back to the late 1960s. It was already known that galaxies emit strongly in IR wavelengths, as much as they do in optical, before the IRAS era (Becklin & Neugebauer 1969). During the same time, it was well understood that the physical process responsible for the IR emission in strong IR galaxies such as Seyfert galaxies is not synchrotron radiation but a thermal radiation emitted by dust in the nuclear region and the origin of the emission is both SF and AGN activity with different proportions (Rees et al. 1969, Burbidge & Stein 1970). Following the understanding of the nature of IR emission, interaction of galaxies was suggested as a possible triggering mechanism behind the IR activity, whether it was AGN or star-burst origin (Toomre & Toomre 1972). At about the same time, the first observations of galaxies emitting above $10^{11}L_{\odot}$ in far-infrared were taken. Kleinmann & Low (1970), among 33 galaxies studied at wavelengths of $1-25\ \mu m$, found strong IR emission ranging from $10^{7}L_{\odot}$ to $10^{15}L_{\odot}$ with QSO 3C-273 being the strongest emitter.

However, after IRAS was launched, the discovery of sources with $L_{IR} \geq 10^{10}L_{\odot}$ and $L_{IR}/L_{B} \geq 1$, where L_B is the luminosity in blue band, became normal (Soifer et al. 1984) with the first group to be discovered being 86 galaxies selected from the IRAS mini-survey. Almost all of the 86 galaxies had $L_{IR}/L_{B} = 1-50$ and a handful of them had $L_{IR} \geq 10^{12}L_{\odot}$. Later, Rowan-Robinson et al. (1991) reported the discovery of a high redshift (z=2.286) IRAS source with $L_{IR} = 3 \times 10^{14}L_{\odot}$.

1.5.2 Energy production and SED of LIRGs

Often the broad band SED of IR galaxies is just the IR emitting component added onto an otherwise normal galaxy SED that is contributed from various other sources within a galaxy such as from old stellar populations and interstellar medium. The main difference with non-IR galaxies is reflected in the infrared part.

Though the contribution from AGN is very minimal especially in low L_{IR} LIRGs, as L_{IR} increases the contribution gets higher (Veilleux et al. 1999, Vega et al. 2008) and its presence is seen by components coming from warm dust peaking at shorter wavelengths (typically about $25\mu m$) than the star-burst component (typically peaking at about $60-100\mu m$). Therefore, at higher luminosity, their SED is a hybrid from SF and AGN, with the higher contribution being from the former.

An example of a broad band SED of a local LIRG with $log(L_{IR}/L_{\odot}) = 11.44$ (NGC0034) is shown in Figure 1.6. An attempt is made to decompose the SED into the different main components using models by Vega et al. (2008). The IR emission from SF can be decomposed

[1] IRAS is first infrared satellite with mid and far-infrared sensitivity in four bands $12\mu m$, $25\mu m$, $60\mu m$ and $100\mu m$ and surveyed 96% of the sky

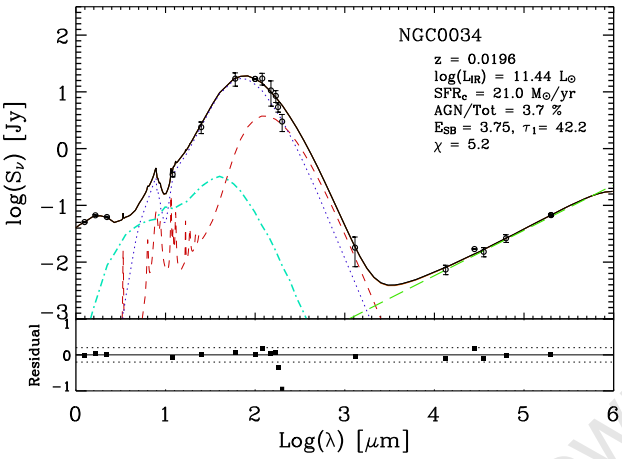

Figure 1.6: *Top panel*: Comparison between the broad band SED (open circles) and the best fit model (thick solid line). The different emission components of the star-burst are: the diffuse medium (short dashed line), the molecular clouds (dotted line), and the non-thermal radio emission (long dashed line). The additional emission from the AGN is indicated by a dot-dashed line. The stellar component is in the total curve but not shown separately. *Bottom panel*: The residuals between models and data are shown in the bottom panel. The thin dotted lines in the residual plot represent ±20% of the residual values (adopted from Vega et al. (2008)).

into a molecular cloud part and diffuse dust. In the radio regime, the SF also produces non-thermal synchrotron radio emission. On the other hand, the AGN process depending on its strength contributes mainly in the mid and far-infrared (small in this case).

In the IR regime of the SED, superimposed on the continuum broad spectrum, there are also different absorption and emission features characterising the SED of LIRGs. A shallower broad absorption feature by amorphous silicates is a prominent feature at about 9.7 μm and the various poly-aromatic hydrocarbon (PAH) emission lines spanning the wavelength range of $5 - 25$ μm are also common features (e.g. Popescu et al. 2011).

1.5.3 Star formation in LIRGs

The fact that LIRGs and Ultraluminous Infrared Galaxies (ULIRGs), defined as IR galaxies with $10^{12} L_{\odot} \leq L_{IR} < 10^{13} L_{\odot}$, are dominated by high optical-depth circumnuclear dust, a reprocessed far-infrared emission is used as a tracer of their obscured SF (Kennicutt 1998a). As new stars form in a dusty galaxy, they emit in ultraviolet (UV) and heat the surrounding dust. The hot surrounding dust eventually re-radiates part of the UV light in far-infrared.

Not all the UV light is reprocessed to emerge as an IR emission. Depending on the opacity of the dust, a varying fraction of the UV emission might make its way out of the surrounding

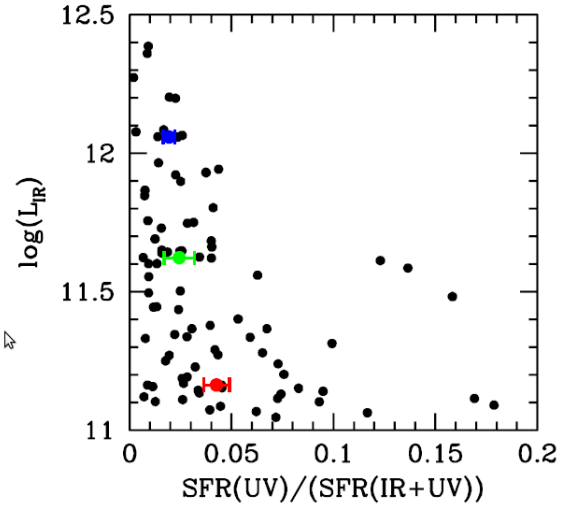

Figure 1.7: The fraction of the contribution from FUV to the observed SFR against L_{IR} among the galaxy sample in the Great Observatory All-sky LIRGs survey (GOALS) (Armus et al. 2009) LIRGs decline with L_{IR}. Median ratios of the SFRs are shown for each luminosity bin (red: $10^{11}L_{\odot} < L_{IR} < 10^{11.4}L_{\odot}$, green: $10^{11}L_{\odot} < L_{IR} < 10^{11.8}L_{\odot}$ blue: $L_{IR} > 10^{11.8}L_{\odot}$ along with 1σ standard deviations of the mean (adopted from Howell et al. (2010)).

dust resulting in a systematic underestimation of star formation rate (SFR) measured by the reprocessed IR emission.

The reliability of using the IR flux to measure SFR is estimated using the infrared excess (IRX) index. IRX is defined as the ratio of IR (=integrated flux $8-1000\mu m$) to FUV luminosity. LIRGs have IRX values ranging from between 1.08 and 3.42, implying that up to a maximum of 75% of UV emission is reprocessed and reappears as IR emission. In terms of their SFR, the contribution of FUV to the SFR of LIRGs is found to vary between 0.2% to 17% (Howell et al. 2010). Generally, the fraction of UV light that emerged without being reprocessed declines with L_{IR} in LIRG regime and becomes very minimal for ULIRGs (see Figure 1.7).

Another effect to the systematic underestimation of the SFR is the effect of dust heating by old stellar population. This introduces an additional IR emission by the dust from non-star forming origins, and as a result, a systematic overestimation of the SFR happens especially in galaxies with different episodes of SF. What is good about these two counteracting effects is that

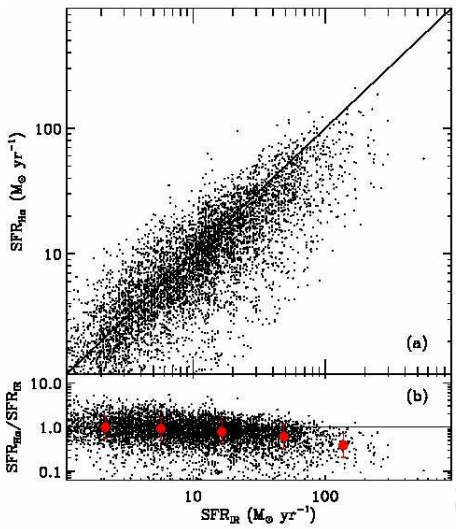

Figure 1.8: The SFR calculated using L_{IR} and H_α for IRAS galaxies are quite similar. The L_α is found for all of the galaxies from a cross match with SDSS (adopted from Kennicutt et al. (2009)).

their effects are approximately of the same magnitude and cancel each other out. Because of this, often the IR SF estimate is consistent with SF from other indicators such as H_α (Kennicutt et al. 2009, Chary & Elbaz 2001).

Figure 1.8 demonstrates a comparison of SFR calculated for IRAS galaxies using L_{IR} and L_{H_α}. The L_{IR} is related to SFR using relationships relating the two quantities from (Kennicutt et al. 2009) and given as:

$$\frac{SFR}{1\,M_\odot\,yr^{-1}} = \frac{L_{IR}}{2.2\times10^{43}\,erg\,s^{-1}} = \frac{L_{IR}}{5.8\times10^{9}\,L_\odot}, \tag{1.9}$$

and L_{H_α} is related to SFR using relationships from (Kennicutt et al. 2009) and given as:

$$SFR_{H_\alpha}(M_\odot yr^{-1}) = 7.9\times10^{-42}L_{H_\alpha}, \tag{1.10}$$

where SFR_{H_α} is the SFR from H_α luminosity and L_{H_α} is the H_α luminosity. The comparison revealed that the two methods agree reasonably well except at the higher end of the SFR. At the higher SF end in the lower panel of the same figure, it is shown that the SFR_{H_α}/SFR_{IR} is below one implying an underestimation of SFR calculated from L_{H_α}. This underestimation is suggested to be because of uncertain extinction corrections to H_α in high L_{IR} galaxies.

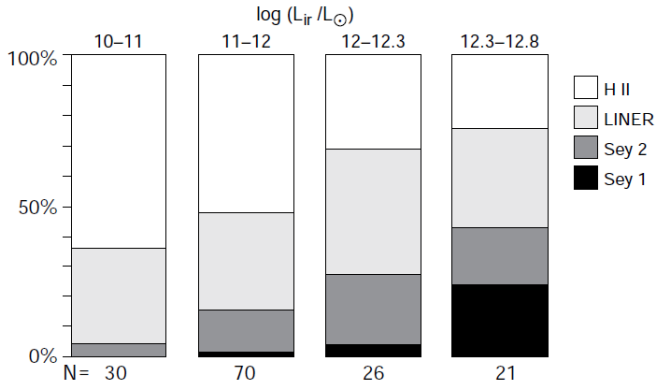

Figure 1.9: The Figure shows that the fraction of AGN hosting galaxies increases with L_{IR} though it is not clear what the percentage of the total IR emission is of AGN origin (adopted from Veilleux et al. (1999)).

1.5.4 AGN activity and SFR in LIRGs

High L_{IR} LIRGs and almost all ULIRGs are powered by energy coming from an AGN in addition to the usual main energy source, SF (e.g. Sanders & Mirabel 1996, Nardini et al. 2009, Veilleux et al. 1999). As accreting matter spirals into the central black hole (the AGN), because of loss of angular momentum, about 10% of its rest mass energy ($\sim 0.1mc^2$) is converted into potential energy and radiated at long wavelength range. Part of this radiation is emitted in the UV. Therefore, UV emission is not always 100% from SF but it could also be from AGN activity. As a result, the possibility of AGN contamination is always a concern and can cause an overestimation of the true SFR.

The contribution of AGN to the energy production of LIRGs and ULIRGs is not constant (e.g Vega et al. 2008, Veilleux et al. 1999). It increases with L_{IR}. Observations from optical spectroscopy show that the presence of Seyfert[2] galaxies increases from $\sim 4\%$ to $\sim 45\%$ when the IR luminosities of galaxies increase from $log(L_{IR}/L_{\odot}) = 10 - 11$ to $log(L_{IR}/L_{\odot}) \geq 12.3$. The contribution from genuine SF to the IR luminosity of an individual strong ULIRG can sometimes be below 50% (e.g. Nardini et al. 2009, and references therein) while with typical LIRGs there would be signs of AGN activity, that would not be the dominant IR emission mechanism.

[2]Types of AGN

1.6 Cosmic Star Formation, Environment and LIRGs

1.6.1 The decline of cosmic SFR

The global SFR has been declining since $z \sim 1$ (about 8 Gyr) almost by an order of magnitude to its present SFR value (Lilly et al. 1996, Madau et al. 1998, Bell et al. 2005, Pérez-González et al. 2005, Le Floc'h et al. 2005). Other observations also agree on the decline although they seem to suggest a delayed time $z \sim 0.6$ (about 6 Gyr) for the start of the decline (Heavens et al. 2004, Tresse et al. 2007).

The total population of IR emitters evolves with redshift and the evolution is stronger for LIRGs and ULIRGs as compared to galaxies whose IR emission is $L_{IR} \leq 10^{11} L_{IR}$ (fainter than LIRGs)[3] (Le Floc'h et al. 2005). Figure 1.10 demonstrates the evolution of the global SFR with redshift and the relative contribution of different star forming galaxies. The contribution for the IR energy density by LIRGs drops by more than an order of magnitude between one and zero. On the other hand, the same energy density drops only by a factor of less than one for fainter IR emitting galaxies and the transition between the two populations seems to occur at about $z \sim 0.5$. Though the relative importance of ULIRGs is rising between $0 \leq z \leq 1$, their dominance in the cosmic SFR seems to come only at later stage between redshifts of 2-3 (Cowie et al. 2004, Le Floc'h et al. 2005, Blain et al. 2002).

The rapid decline of the number density of luminous IR sources (LIRGs) implies a shift of SF mode from violent and bursting at $z \sim 1$ and above to a modest and quiescent mode at $z \sim 0$. This shift in SF mode might give an indirect clue to explaining the actual reason why the global SFR is declining. One way of understanding this decline is to understand the global evolution of the different physical processes driving SF. This includes: environmental factors (major mergers, tidal interactions, ram pressure stripping, galaxy harassment) (de Ravel et al. 2009, Lin et al. 2008), gas consumption (Bell et al. 2005) and the secular evolution of bars (Sheth et al. 2008). Given the interacting nature (environmental factor) of LIRGs which are an important galaxy population in the evolution of cosmic SF, the major merger rate stands in the for front in addressing the issue.

Mergers undoubtedly play a prominent role in the evolution of galaxies through cosmic time (Ilbert et al. 2006, Tresse et al. 2007). However, its contribution to the evolution of cosmic SFR is not well understood partly because identifying galaxy mergers especially at high redshift is a difficult task. There are two different arguments about the evolution of the merger rate. The first argument is that the average merger rate is constant since $z \sim 1$ and consequently, merging has little or no effect on the declining global SFR (Bundy et al. 2004, Elbaz et al. 2007). There is observational evidence in support of this argument showing the presence of a high fraction of star forming galaxies with undisturbed morphology at high redshift (Bell et al. 2005, Elbaz et al. 2007). Besides, at intermediate redshifts, $z \sim 0.5$, more than half of the LIRG population

[3]These galaxies form stars in a very quiescent mode

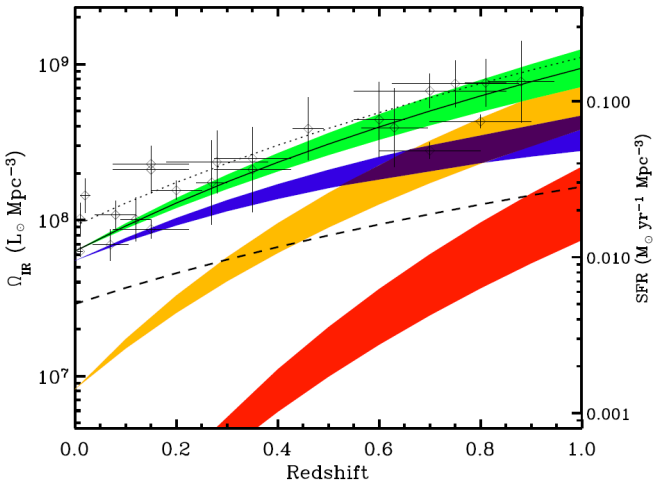

Figure 1.10: The total co-moving IR luminosity density of the Universe has declined with redshift. LIRGs dominate the IR energy density at high redshift while normal galaxies dominate at low redshift. The green shaded region represents the evolution of the total IR energy density. The blue, yellow and red shaded regions represent the contribution from low luminosity ($L_{IR} \leq 10^{11} L_\odot$) galaxies, LIRGs and ULIRGs respectively towards the total IR density at different redshift (adopted from Le Floc'h et al. (2005))

appear normal spiral in their morphology (Melbourne et al. 2005). These findings suggest that the importance of mergers in the global SFR in the redshift range $0.5 \leq z \leq 1$ is not significant and call for other possibilities.

On the other hand, studies conducted using physical proximity between galaxies (close pairs) concluded that close pair interactions or mergers are an important mode of SF for LIRGs and ULIRGs at high redshift (Bridge et al. 2007). A close look at mergers by de Ravel et al. (2009) both in potential star forming galaxy population (late type galaxies) and early type galaxies revealed that the fraction of close pairs in the former evolved more strongly than in the latter (see Figure 1.11).

A similar but more holistic aspect that can lead to a better understanding of why the global SFR is declining is the understanding of the relationship between local environment and SFR of galaxies at both high and low redshift Universe. Recent studies suggest that there is fundamental difference between the SF density relationship at the two redshifts and refer to the situation as the "reversal of SF density relationship" (e.g. Elbaz et al. 2007).

1.6.2 The reversal of SF density relationship.

In low redshift Universe, SFR and local environment of galaxies are anti-correlated (Gómez et al. 2003, Kauffmann et al. 2004). Strongly star forming galaxies seem to prefer relatively low

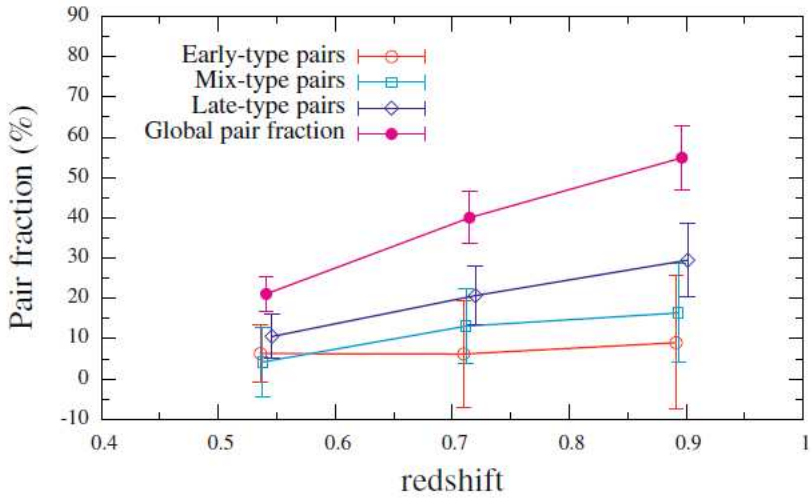

Figure 1.11: The redshift evolution of close pairs for different Hubble types of galaxies. The evolution is stronger for late-type galaxies and weaker (non-existent) for early-type galaxies (adopted from de Ravel et al. (2009)).

density environments while weakly star forming galaxies seem to dominate cluster environments. This trend, however, is reversed at high redshift Universe. SFR increases with environmental richness in the high redshift Universe (Elbaz et al. 2007, Tran et al. 2010, Li et al. 2011) although a similar result by Cooper et al. (2008) suggested that depending on the population of galaxies, one can see both an increasing and decreasing trend. Cooper et al. using the n^{th} neighbour density estimation, found a "V" shaped trend between environment and SFR with the SFR of red sequence galaxies decreasing with density and blue cloud galaxies increasing with density. Figure 1.12 illustrates the comparison of the relationship at high and low redshift Universe. A trend similar to the case in local Universe is also witnessed based on data at $z = 0.75$ by Finn et al. (2005).

A weakening of large scale structure formation process is proposed as a possible explanation for the observed reversal (Elbaz et al. 2007). For example, one particular cluster Elbaz et al. (2007) considered showed that it is made of three separate groups with highly star forming galaxies, such as LIRGs, located in their cores. The groups seem still in the process of forming the cluster. Knowing that high star forming galaxies do not seem to reside in clusters at local Universe, their result could mean that, in the local Universe the observed SFR-density relation is a reflection of weakened structure formation. This could further imply that majority of SF in the present day Universe is not driven by the process of cluster formation. It is rather taking place in individual groups and field galaxies and hence we observe the opposite SFR-density

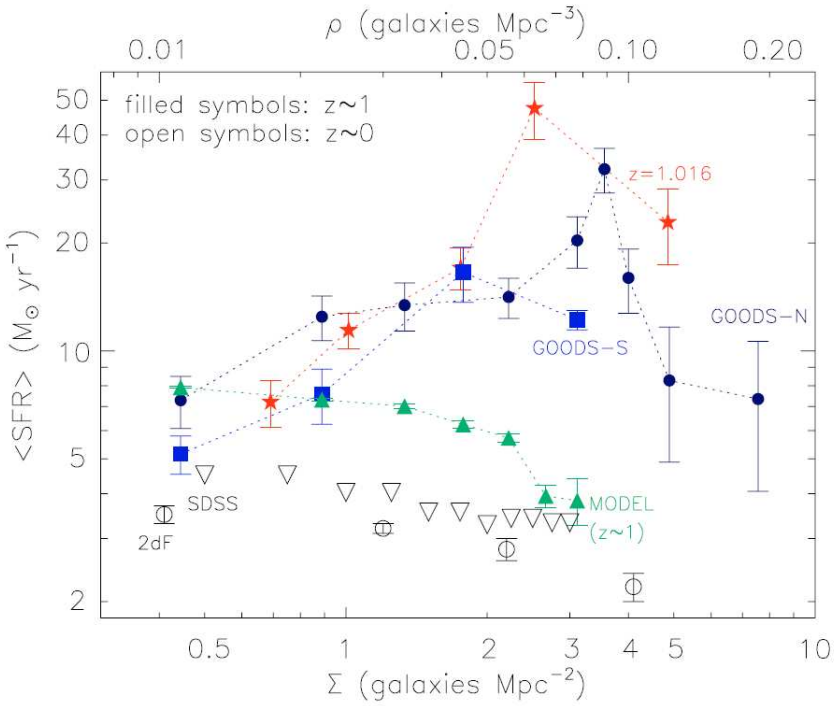

Figure 1.12: The SFR and local density of galaxies are related in different ways at local and high redshift Universe (adopted from Elbaz et al. (2007)).

trend.

However, other studies based on stellar mass limited samples found that the SF-density relationship at high redshift is not any different to the case at lower redshift Universe (Holden et al. 2007, Patel et al. 2009). And still some argue that these differences between high and low redshift SF-environment trends are only apparent and are a result of mass downsizing and selection effects operating together (Sobral et al. 2010). At high redshift Universe, because of higher luminosity detection limits, surveys are naturally biased to probing higher mass regime. On the contrary, at the low redshift Universe one can easily probe a wider mass range. When we add the effect of mass down-sizing to this, the contradicting results may not be surprising. As a result, a better detection limit especially at high redshift Universe is required in order to better understand these processes. Surprisingly, there are even other studies that found no correlation between environment and SFR at high redshift Universe (e.g. Finn et al. 2005, Cucciati et al. 2006, Patel et al. 2009, Tasca et al. 2009, Feruglio et al. 2010).

Despite the importance of LIRGs in the global SF history of the Universe and their strongly interacting nature (and hence strong connection to their environment), so far not much is known about their environment. Of course being high star forming galaxies, one expects that cluster environment is maybe too chaotic to allow LIRGs to form stars at the level they do (see Sec-

tion 1.3). A SF activity of their level and nature is also uncommon in a field environment. Therefore, with the common SF environment knowledge from other types of galaxies in the local Universe, one could obviously suspect that local LIRGs must live in a group environment; this, however, has not been shown convincingly to date.

Generally in the local Universe, LIRGs seem to be found in a wide range of environments. Tacconi et al. (2002), by correlating a small sample of LIRGs and ULIRGs to the NED galaxy clusters and groups, found that LIRGs and ULIRGs are found only in the field or in small groups of galaxies (less than ten members). There is also observational evidence that shows some LIRGs living in an environment such as on the outskirts of clusters (Laag 2006, Duc et al. 2004, Lemonon et al. 1998, Kleinmann et al. 1988). A recent study found that the L_{IR} values do not seem also to be correlated with their local environment for local LIRGs (Hwang et al. 2010).

In the high redshift Universe, on the other hand, some studies found that the L_{IR} values of LIRGs are correlated with the richness of their environment. Elbaz et al. (2007), studying a high redshift cluster, observed that the L_{IR} values of LIRGs increases as they are closer to the centre of small groups forming the cluster. However, another study indicates that there is no correlation between the local environments of LIRGs, quantified by the projected third neighbour, and their L_{IR} values (Marcillac et al. 2008) (see Figure 1.13). The same work further concluded that the local environments of high redshift LIRGs and ULIRGs are intermediate between field and group environments. Caputi et al. (2009) in turn found that their sample of LIRGs at redshifts $0.6 < z < 0.8$ lived in overdense and more passive environments, while ULIRGs were at under-dense and more active environments, compared to other galaxies with similar masses. On the other hand Finn et al. (2010) claimed that the fraction of LIRGs in a redshift range of $0.4 < z < 0.8$ is higher in fields than in clusters.

All the above results show that the environments of local LIRGs are not well explored and understood and there quite a number of controversies in the matter. This thesis tries to address this issue with a large set of data.

1.7 Dwarf irregular galaxies and their chemical abundances

Dwarf galaxies are often defined as galaxies with $M_B \geq -18$ mag (Sandage & Binggeli 1984) and in the lower end they could have a luminosity as low as $M_v \sim -2.6$ mag (Willman et al. 2005). Though there is wide variation in their structure and other physical properties such as morphology, dwarf galaxies are generally small in size, less massive, less luminous than other galaxies and not much evolved (typically they have 1/10 of solar metallicity or even less) (Kunth & Östlin 2000). Among themselves, they have a wide range of gas fractions and variations in their physical appearance. The most vivid distinction among them is seen between the gas-rich star forming dwarfs irregulars (dIrr), and the gas-poor dwarf spheroidal (dSph) and dwarf ellipticals (dE).

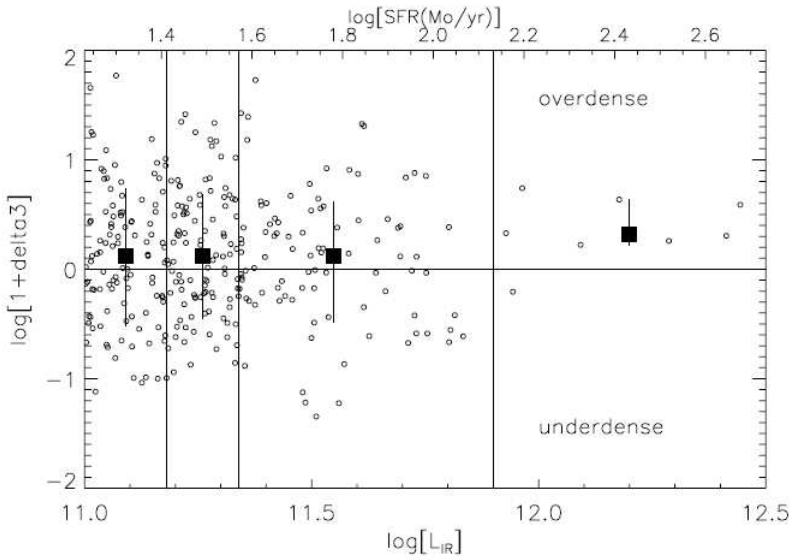

Figure 1.13: The correlation between L_{IR} and the local environments of high redshift LIRGs and ULIRGs. The result shows there is very weak or no correlation at all between the two quantities (adopted from Marcillac et al. (2008)).

dE have no sign of recent SF, are dominated by old stellar populations (Yoshii & Arimoto 1987) and in most cases appear featureless and diffuse in their physical appearance (Mateo 1998). They seem to share many physical properties including a similar metallicity-luminosity relationships with elliptical galaxies (Caldwell & Bothun 1987). Despite these similarities, they do not appear to have an evolutionary link (Bender et al. 1992, Graham 2005). dSph, like the dE, show no sign of current SF and do not have much gas content. However, dSph show some sign of several past bursts of SF in the past. They have a very large dynamical mass-to-light ratio which implies that they are unusually dark matter dominated (Mateo 1998). The main difference between dSph and dE is that dSph seem to be less luminous than dE.

As their name implies, dIrr are very asymmetrical in their appearance and have messy internal structure, with numerous loops and filamentary structures (e.g., Large and Small Magellanic Clouds). Their chaotic internal structure is explained in terms of numerous activities ranging from supernova explosions and stellar winds to random motion of gases (Mac Low & Ferrara 1999). They have a high fraction of gas (HI) and their gas extends far out beyond the optical disk (Wilcots & Hunter 2002, Hunter & Wilcots 2002). For example, the HI distribution in IC 10 and NGC 6822, both dIrr, extends up to ten times their optical light. They are dominated by recent SF and as a result, they contain one or more bright HII regions and appear bluer than their cousins dE and dSph in most cases. These galaxies are less dusty as a consequence of their lower metallicity content and hence they are not prominent in the IR band.

1.7.1 Star formation in dIrr

As it is mentioned above, dIrr galaxies have a high fraction of gas and are dominated by recent SF activity. However, there are different views regarding their SF mechanism. Their internal structure is very chaotic and they do not seem to have any well organised structure like spiral arms and hence their SF mechanism cannot be driven by spiral density waves (Spitzer 1978, Hirashita 2000).

Some believe that the driver of SF in dIrr galaxies is a stochastic self-propagating SF process triggered by supernova explosions, stellar winds or some other internal process such as random motion of the gas (Recchi & Hensler 2007, Spitzer 1978). According to this model, SF at one area leads to supernovae explosions and gas outflows which push material to another area and triggers SF there. In this manner, SF propagates around the different areas in the galaxy.

It is also possible that SF in dIrr galaxies could be triggered by environmental factors. Because of their loosely bound internal structure and their low potential, dIrr can easily be perturbed by any external factors and are less efficient in resisting any environmental factor that could trigger SF. Different studies found strong signs of interaction (Brosch et al. 2006, Moiseev et al. 2010, and references therein). Pustilnik et al. (2001) studied the environments of blue compact galaxies, which are the closest cousins of dIrr galaxies, and found that about 80% of the galaxies in their sample have either interacting neighbours with strong tidal action or have merger morphologies and concluded that environment plays a strong role.

Some studies, however, reported that the SF history of dIrr in a dense environment does not seem to be much different from the SF properties of galaxies in less dense environments. For example, it was found that the dIrr galaxies in the Virgo cluster have comparable oxygen abundances at a given luminosity with dIrr from the field environment (Lee et al. 2003). Figure 1.14 shows a comparison of the metallicity-luminosity relationship between field and cluster dIrr and it is found that they seem to follow more or less the similar trend. Their metallicity-luminosity relationship does not discriminate between galaxies with clear interaction features (positive tidal index) and galaxies with no obvious interaction features (negative tidal index) (Lee et al. 2007). This result again strengthens the idea that the environment does not have an obvious influence on dIrr galaxies.

1.7.2 HII regions and metallicity in dIrr

HII regions are ionized gas clouds associated with recent SF. In star forming regions, the ultraviolet emission from young stars (typically O or B stars with temperatures greater than $10^4 K$) ionizes the surrounding gas which is mainly neutral (HI) and molecular (H_2) hydrogen. Eventually when the knocked off electrons during the ionization process recombines with the different ions, the result gives rise to the Balmer recombination line and the different forbidden lines seen in HII regions. The common strongest emission lines include the hydrogen Balmer lines (H_α, H_β, H_γ, H_δ), [NII] at 6583 Å, [OII] at 3726 and 3729 Å, [OIII] at 4959 and 5007 Å and [SII] (at

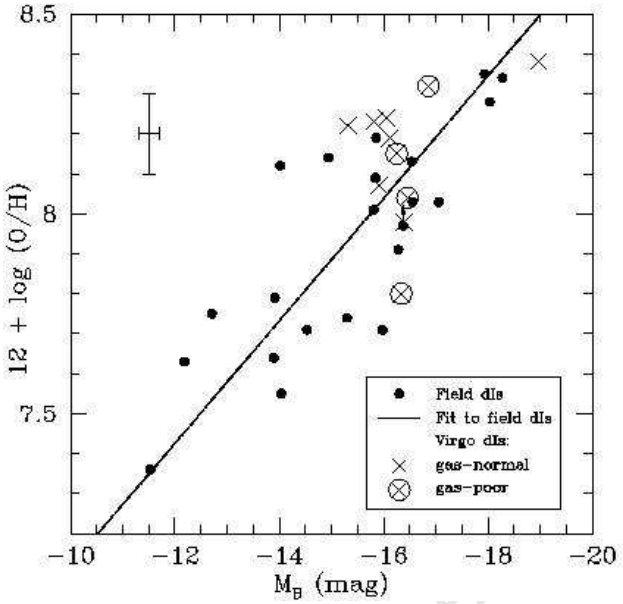

Figure 1.14: The oxygen abundance vs. absolute luminosity in B for field and Virgo dIrr. The filled circles are field dIrr and the solid line is their best fit. The crosses represent the Virgo dIrr (gas normal) and the crosses enclosed by circles are the gas-poor Virgo galaxies. The error bars indicate typical uncertainties for the oxygen abundance and the absolute magnitude (adopted from Lee et al. (2003))

.

6716 and 6731 Å).

Since the bulk of ionizing UV light is contributed by young stars, the emission lines in HII regions are a good tracer of SF in galaxies. Moreover, the emission lines are a very useful diagnostic tool for the different physical conditions in the gas. For example, [SII]λ6716 and [SII]λ6731 are sensitive to the electron density and they can be used to determine the density of HII regions. This is because they are emitted at different levels but with nearly the same excitation energy, so that their relative ratio is a diagnostic of the collisional de-excitation, or the density, of the gas (Stasińska 2002). On the other hand, the emission lines such as [OIII]$\lambda\lambda$4959, 5007 and [NII]$\lambda\lambda$6548, 6583 are sensitive to temperature (Aller 1984) and they can be used to calculate temperatures. The strength of the emission lines are also used to determine the abundance of different elements in galaxies (Stasińska 2002).

The key relevance of studying HII regions in extragalactic astronomy, in addition to the fact that they are bright enough to be easily observed, is their strong association with chemical evolution and heavy metal enrichment which are driving the general evolution of galaxies in the Universe. They are sites of heavy-element production through sequences of SF that use up the

material produced from the previous episode of SF processes and become mixed up with the ISM through various mechanisms such as supernova explosions, stellar wind, etc. The elements heavier than H and He in stars and the ISM are the cumulative product of previous generations of stellar process.

Understanding the chemical evolution of galaxies requires the knowledge of the production rate and distribution of chemical elements, especially the heavy elements[4]. One way of doing this is determining the abundance of metals (for example (O/H) for oxygen abundance) and various other important elements such as Fe, N and Ne. The abundance can be inferred from the strength of the emission lines using various methods. The variants are used depending on the strength of the different emissions in the HII spectra which in turn depend on the metallicity and brightness of the system under consideration. We will discuss below few of the methods very briefly.

The direct method of abundance determination

This method is the most reliable method since the electron temperature is determined directly from the temperature sensitive line ratios such as [OIII](λ5007,4959/λ4363), and the abundance is calculated from these temperatures[5]. The dependency between abundance (metallicity) and temperature comes from the fact that higher metallicity in HII regions increases nebular cooling (as the cooling is via metals) and this establishes a relationship between HII electron temperature and metallicity (Stasińska 2002).

In galaxies with low metallicity content (12+log(O/H)$\leq$8.5)[6], all the emission lines that are important to employ the direct method of metallicity are strong. A typical spectrum of an HII region of a galaxy with low metal content is shown in the upper panel of Figure 1.15. The plot clearly shows that the [OII], [OIII] lines, the Balmer and Paschen series and the weak auroral lines of [OII] and [SII] are detectable. As a result, in low metallicity HII galaxies, the direct method of metallicity determination can easily be applied.

In metal rich galaxies (12+log(O/H)$\geq$8.5), the most important lines for the application of the direct method of abundance determination, especially the forbidden auroral line, [OIII]λ4363, are weak. The lower panel of Figure 1.15 shows a typical spectrum of an HII region with high metal content and one can note the difference between the spectra of high and low metallicity HII regions. Moreover, the temperature cooling is high in high metallicity (12+log(O/H$\geq$8.5) regions. As a result, the abundance determination using a direct measurement of electron temperature is not efficient in metal rich HII regions.

[4]astronomy anything heavier than hydrogen and helium are called "metal" unlike the traditional meaning of the word.

[5]The reason why it is called the direct method is just because the temperature is directly inferred from the emission lines

[6]The metal rich and metal poor metallicity ranges are not always standard and different works use different range but generally they are not much different.

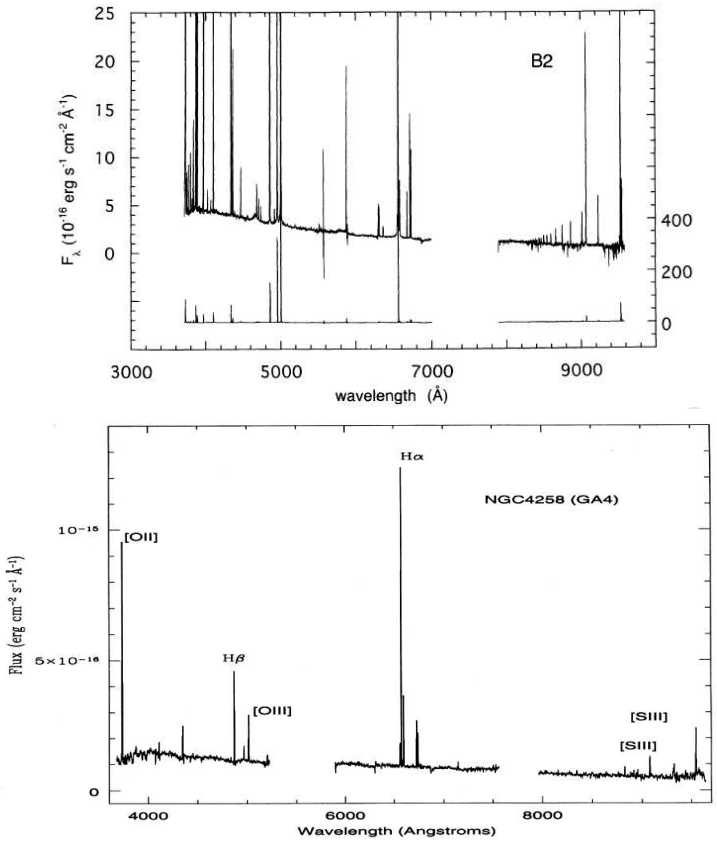

Figure 1.15: *Upper panel*: Spectrum of knot A of NGC2363, which is a metal poor galaxy (adopted from Gonzalez-Delgado et al. (1994)). *Lower panel*: Spectrum of the spiral disc of NGC4258, which is a metal rich galaxy. (adopted from Díaz et al. (2000))

However, once the temperature is known, the abundance determination can be carried out in various ways. For example, the abundance of a collisionally exited ion X relative to H^+ (given as $\frac{N(X^{+i})}{N(H^+)}$) is related to its T_e through the volume emission coefficient ϵ. The relationship can be given as:

$$\frac{N(X^{+i})}{N(H^+)} = \frac{I(\lambda)}{I(H\beta)} \frac{\epsilon(H\beta)}{\epsilon(\lambda)}, \tag{1.11}$$

where $\epsilon(H\beta)$ is the volume emission coefficient of $H\beta$ and $I(\lambda)$ is the intensity of the ion X. The emissivity ϵ is function of the electron temperature and its dependence is

$$\epsilon(\lambda) \propto T_e^{-0.5} e^{-\chi/\kappa T_e}, \tag{1.12}$$

where κ is the excitation energy of the upper level for the transition of the ion. The treatment followed in here is discussed thoroughly in Esteban et al. (2004), Osterbrock & Ferland (2006).

The other option to determine abundance is using grids of photoionization models (or model fitting) that are built by taking into account all of the most important physical processes controlling the ionization and temperature of the HII region and assume ionization and thermal equilibrium in the gas (Ferland 1995, Ratag et al. 1997).

As it is discussed above, the direct method of abundance determination does not work well unless the temperature sensitive lines (for example, [OIII]λ4363) are bright enough to be detected. These lines cannot be detected when the HII region itself is either not bright enough intrinsically or when it is metal rich and consequently very cool. The reason for latter is as metallicity increases electron temperature decreases and as a result the temperature sensitive lines become too faint to measure. In such cases, one needs to rely on other methods. Bellow we discuss an alternative method we have used in this work in the absence of the temperature sensitive line [OIII]λ4363.

The R_{23} method

In the absence of emission lines such as [OIII]λ4363, the abundance calculation must therefore be done using other empirical methods based on the intensities of strong optical lines. One of the empirical methods which could be used in abundance estimation for metal-rich (12+log(O/H)$\geq$8.5) galaxies is the R_{23}-method (see the works by Kobulnicky et al. 1999, Tremonti et al. 2004). It involves R_{23}=([OII] λ3727+[OIII]$\lambda\lambda$4959,5007)/Hβ parameter and it is well calibrated by various authors on various occasions (e.g. Oey & Shields 2000, Pilyugin et al. 2010) and seems to work very well especially in the higher metallicity regime, where 12+log(O/H)>8 (Yin et al. 2007). However, there have also been attempts to use it in the lower metallicity regions (e.g. Skillman et al. 1989).

The R_{23} produced abundances are not always consistent with abundances determined using the direct method. Sometimes, the discrepancy is large; the R_{23} method can overestimate log(O/H) by a factor of up to 0.5 dex (Kennicutt et al. 2003, Bresolin et al. 2004). It is argued that part of this difference arises as a result of using the R_{23} method at the metallicity region where it is not appropriate to use it (Pilyugin 2003). In fact, this problem is mentioned as being the culprit for the double metallicity gradients seen in some disk (or spiral) galaxies (Pilyugin 2003).

There are also additional methods which use different, easily detectable, lines to estimate abundances depending which lines are strong in the spectra of HII regions. These include the N2 index method which uses the ([NII]λ6583/Hα) and the S2 index method which uses the ([SII]$\lambda\lambda$6717,6731)/Hα line ratio (for detail discussions of these methods, see Yin et al. 2007, Pilyugin & Mattsson 2010).

1.7.3 The metallicity-luminosity relationship in dIrr

The metallicity of dIrr shows correlation with their mass. The smaller systems have lower metallicity (Lequeux et al. 1979). However, this relationship is often presented as a metallicity-luminosity relationship as the mass of a galaxy is a poorly understood quantity of a galaxy and a galaxy luminosity is strongly correlated with its mass (Richer & McCall 1995, Skillman et al. 1989). This relationship shows more scatter at low luminosities and it is argued that this scatter is partly because of uncertain measurements of metallicity as well as luminosity at the low luminosity end (Richer & McCall 1995, Pilyugin 2001).

The physical mechanism driving metalicity-luminosity relationship is not fully understood and perhaps it could be that different physical mechanisms are responsible. The popular explanation for the observed metallicity-luminosity relationship attributes the trend to the ability of galaxies to maintain their metallicity content against anything driving metals out of them. The driving forces could be supernova explosions, stellar winds or galactic winds (Dekel & Silk 1986, Larson 1974). Higher mass galaxies have a stronger resistance to the out-flow due to their high potential well than small mass systems and as a result they have more metals than the small ones. Other theories relate the issue with the evolution of the galaxies along their luminosity sequence. It could be that the higher luminosity dIrr evolved much faster and produced a lot of metals, while the low luminosity ones are still in their early phase of evolution and have not produced much metals yet (see the review by Garnett 2004).

The metallicity-luminosity relationship of dIrr galaxies is used to understand various issues ranging from their evolutionary sequence to their SF properties to chemical enrichment of their interstellar medium. Below we will review the evolutionary connection between dIrr and dSph using this relationship.

1.7.4 An evolutionary connection between dIrr and dSph

dSph galaxies have more similarities to dIrr than to normal elliptical or any other galaxies (Kormendy 1985) and hence it is believed that there is an evolutionary connection between dIrr and dSph. The dSph galaxies are assumed to be the more evolved form of dIrr that have lost their gas content due to different reasons ranging from internal processes (supernova explosions, stellar wind, etc) to external factors (ram-pressure stripping) (Kormendy & Djorgovski 1989, Grebel et al. 2003). On the contrary, some have suggested that these two types of galaxies do not have any evolutionary connection and that they only represent two forms of parallel dwarf galaxies. According to the latter theory, both dSph and dIrr lose their gas due to the reasons mentioned above, but for some reason the dIrr manage to retain some of it (Dekel & Silk 1986).

If dIrr are destined to be dSph by exhausting their gas through SF or by removing their gas through some mechanism, then one expects dSph to show a similar metallicity-luminosity relationship to that of dIrr, but shifted to lower luminosity. According to this scenario, at a given luminosity, dSph appear to be more metal rich than dIrr. However, if dSph is found to have lower

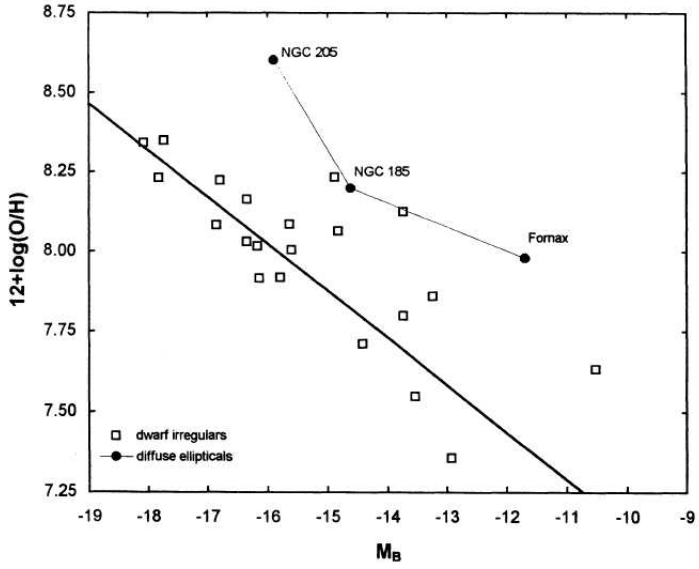

Figure 1.16: The metallicity-luminosity relationship of dIrr and dSph galaxies. According to this plot it seems that dSph are an evolved remnant of the dIrr (adopted from Richer & McCall (1995))

metallicity than dIrr at a given luminosity, any evolution of dSph to dIrr is impossible. Richer & McCall (1995) showed that the first theory could be possible by finding a somewhat shifted metallicity-luminosity relationship for dSph while having a similar gradient with dIrr. Their result is presented in Figure 1.16. However, the same study shows from the [O/Fe] ratio that these two classes of dwarf galaxies have different SF histories, and an evolutionary connection is unlikely. They suggested that the only difference between these two types of galaxies is that dSph for some reason consumes their gas faster than dIrr and thus appears to be gas-poor.

Using the discussion so far as a background, this work addresses SF properties of interacting and dwarf irregular galaxies from different perspectives. In Chapter 2, using different surveys to quantify the environments of galaxies, we will study the relationship between SF and the environment of local luminous infrared galaxies. In the Chapter 3, we will address the same problem addressed in Chapter 2 but from a more theoretical perspective. We use the size of the dark matter haloes that luminous infrared galaxies live in to characterise their local environment and see if their SF is indeed consistent with their local environment. In Chapter 3, we study the metallicity and the metallicity-luminosity relationship as well as metallicity gradient of a small sample of dwarf irregular galaxies. Finally in Chapter 4, we conclude the entire work by summarising the main results and discussing future prospects.

2

The relationship between star formation rate and environment of local LIRGs

2.1 Brief background and objective

While it is clear that the immediate environment is a major driving force behind the SF properties of LIRGs, it is not clear how significant a role the larger scale environment (such as the 1-2 Mpc scale environment) beyond their immediate neighbours plays in their SF characteristics (e.g. Sanders & Mirabel 1996). Normally, the environment on a scale of 1Mpc plays a crucial role in shaping the SF properties of the general galaxy population (Lemson & Kauffmann 1999, Blanton et al. 2006). Even if it is clear that the larger scale environment of galaxies has a connection with their SF properties, often this connection is a complex matter to fully understand and draw any trend because of other influences that coexist with it. Stellar mass is one such important issue that can significantly influence any SF-environment relation.

The effect of stellar mass can be expressed in terms of the so called "Mass down sizing" effect. Mass down sizing is an important factor in establishing the relationship between stellar masses and SFR of galaxies. In the local Universe, it is observed that galaxies having higher rates of specific star formation rate tend to be smaller in their stellar mass than galaxies with lower SFRs. In fact, there are some findings indicating that such mass down sizing effects are already in place even at $z \sim 1$ and above (see section 1.6.2 in Chapter 1). LIRGs, being among the most star forming galaxies in the local Universe, are normally expected to be less massive. However, this is yet to be proven.

This chapter addresses the influence of environment and stellar mass on SF of local IR galaxies. It specifically addresses:

1. The influence of the larger scale, the 2Mpc scale, environment on the SF properties of LIRGs and non-LIRG IR galaxies with special emphasis given to how much and in what fashion the SF of LIRGs is influenced by the effect of the large scale environment.
2. Whether an environmental divide exists between LIRGs and non-LIRG IR galaxies and if so, how does the environment correlate with SF in both cases.
3. The possible stellar mass influence on the SF property of these galaxies.
4. The possible similarities between the environment-SFR trend found for LIRGs with the same trend for other type of local galaxies (SDSS) and high redshift galaxies.

The overall structure of the chapter is as follows. It starts with presenting the different data used. In the next Section a detailed explanation of the quantification of the environment and how SFR and stellar mass are derived. Following that, the results found will be discussed and finally, a thorough discussion of the results found is presented. The chapter is concluded with a summary that highlights the most important results. Throughout this work, we have used $\Omega_m = 0.3$, $\Omega_\Lambda = 0.7$ and $H = 100h^{-1}$.

2.2 Data

The data used in this work are presented in two groups. The first one is the sample around which we studied the local environment. We refer to this group as the *target galaxy sample*. The second group is the galaxies used to quantify the local environment and this group is referred as the *density field sample*.

2.2.1 Target galaxy samples

The target galaxy samples are taken from a combination of two IRAS redshift surveys: Point Source Catalogue redshift survey (PSCz) (Saunders et al. 2000) and The Imperial IRAS-Faint Source Catalogue redshift sample (IIFSCz) (Wang & Rowan-Robinson 2009).

The Point Source Catalogue Redshift (PSCz) Sample

The Point Source Catalogue redshift survey (PSCz) contains 18351 IRAS selected galaxies and covers nearly 85% of the sky. Most of the data for PSCz are taken from the IRAS catalogue but also supplemented from different sources including NASA/IPAC Extragalactic Database (NED)[1]. It goes as deep as 0.4 in redshift space. Generally the catalogue is complete and

[1] http://nedwww.ipac.caltech.edu

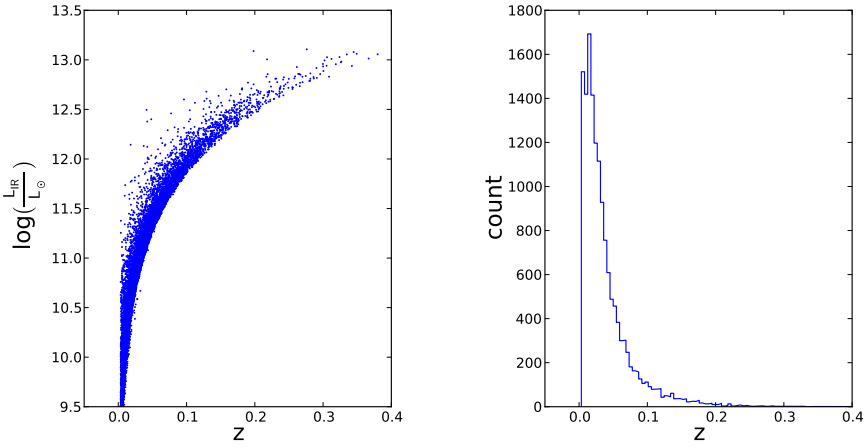

Figure 2.1: *Left panel*: L_{IR} versus redshift. *Right panel*: the redshift distribution of PSCz galaxies.

uniform within a few percent at high galactic latitude and 10% at low latitude. The redshift distribution and L_{IR} distribution of the original PSCz sample is shown in Figure 2.1.

The catalogue is cross-matched with 2MASS Extended Source Catalogue (Jarrett et al. 2000) at a search radius of $60''$ in order to obtain the absolute K-magnitude, M_K, to derive stellar masses for its galaxies. The choice of the search radius was made based on a test we did for different searching angles ranging from $5''$ to $100''$ for randomly selected 5000 PSCz galaxies. The number of galaxies for which we got at least one match at different searching radius starting from $5''$ increased at a constant rate till it reached about $60''$ and we thus took $60''$ to be a reasonable searching radius that can give us genuine matches with a minimal inclusion of false matches. Note that it is estimated based on the surface density of 2MASS galaxies, that there is only $\sim 1\%$ chance to have a random 2MASS match within this area. At $60''$, only less than 5% of the PSCz galaxies have two matches and less than 1% have more than two matches; considering the low fraction of multiples, we merely selected the closest one. In addition we did not attempt de-blending or re-distributing the IRAS detection and flux into 2MASS counterparts. After matching the entire PSCz to the 2MASS at this radius and excluding the galactic plane, $|b| \leq 10$, and sources with $V \leq 1000\text{kms}^{-1}$, we found 11727 PSCz galaxies having matches from 2MASS. These galaxies form part of the sample of IR-selected galaxies the environment of which this work studies and from now onward we refer to it as PSCz-I. Out of the total number of PSCz-I, 2956 galaxies have $L_{IR} \geq 10^{11}h^{-2}L_\odot$ while the remaining 8771 have $L_{IR} \leq 10^{11}h^{-2}L_\odot$.

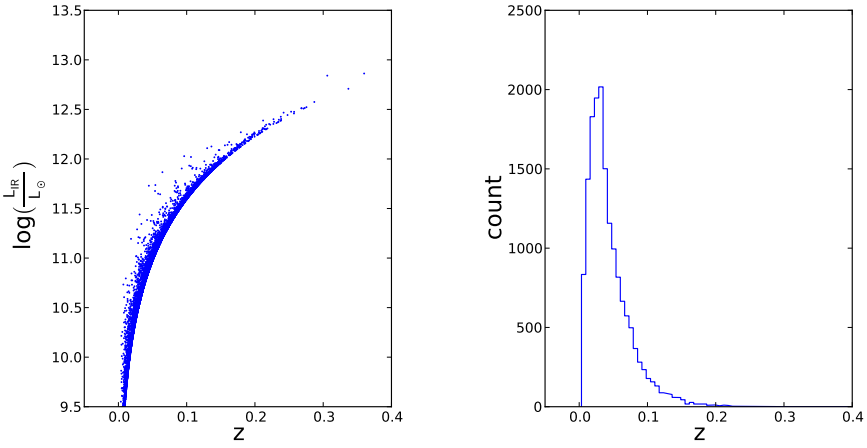

Figure 2.2: *Left panel*: L_{IR} versus redshift. *Right panel*: the redshift distribution of IIFSCz galaxies.

The Imperial IRAS-Faint Source Catalogue (FSC) redshift Sample (IIFSCz)

The IIFSCz catalogue is constructed based on the IRAS Faint Source Catalogue (FSC) (Moshir et al. 1992) and has 60,303 galaxies selected based on their $60\mu m$ IRAS flux and covers 61% of the entire sky. Almost 55% of theses galaxies have spectroscopic redshifts found by cross matching IRAS-FSC with various previous redshift surveys such as IRAS PSCz (Saunders et al. 2000), FSCz (Oliver et al. 1996) and 6dF (Jones et al. 2009). Approximately 20% have photometric redshifts estimated either by template-fitting or empirical training method. For $S(60) \geq 0.36Jy$, the catalogue is 90% complete in redshift. The redshift distribution and L_{IR} distribution of the original IIFSCz sample is shown in Figure 2.2. In this work, we considered only galaxies with spectroscopic redshift. Together with PSCz-I, this sample is used as an IR target galaxy sample around which the environment is studied.

Since PSCz-I (Section 2.2.1) and IIFSCz samples are both originally from IRAS, we think it is natural to merge and treat them together as a target galaxy sample. Before the two samples are merged, however, 5853 duplicates between PSCz-I and IIFSCz are identified and removed from IIFSCz by cross matching them at a search radius of $\leq 20''$ which is a reasonable radius based on IRAS positional uncertainties (Neugebauer et al. 1984). Again removing the galactic disc ($|b| \leq 10$), sources with $V \leq 1000\text{kms}^{-1}$and including only sources with K-band flux and spectroscopic redshifts, the IIFSCz sample is reduced to 16207 galaxies. From this subset, 5137 galaxies have $L_{IR} \geq 10^{11}h^{-2}L_\odot$ while the remaining 11069 have $L_{IR} \leq 10^{11}h^{-2}L_\odot$. We refer to this final IIFSCz catalogue as IIFSCz-I.

Finally PSCz-I and IIFSCz-I are merged. This merged catalogue has 27934 galaxies with redshift range $0.003 < z < 0.14$ and a mean redshift of 0.029. Hereafter, this merged catalogue

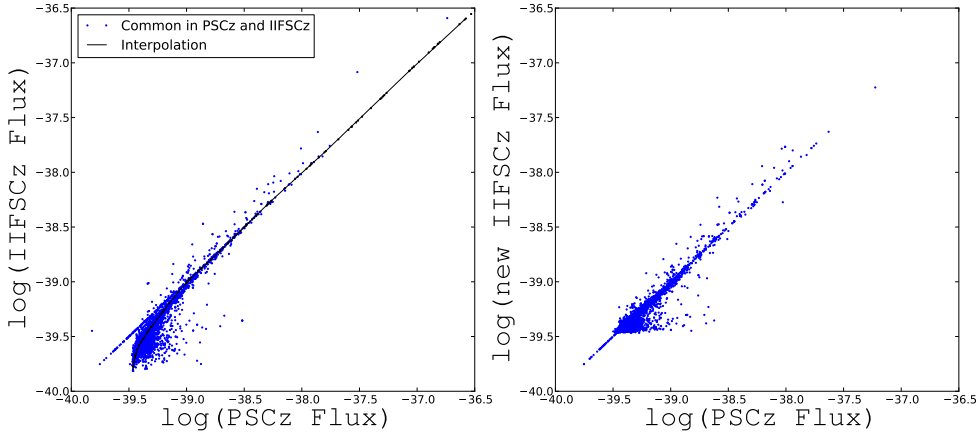

Figure 2.3: *Left panel*: IIFSCz fluxes are underestimated as much as 30% at the lower flux limit as compared to the flux of the same galaxies found in PSCz. *Right panel*: All the IIFSCz fluxes are corrected to PSCz flux using interpolation based on the fluxes of galaxies found in both catalogues. Note that only randomly selected 40% of the data is presented.

is referred to as IRAS-I.

Correction of F_{IR} and calculating L_{IR}

The far-infrared fluxes $F_{IR} = F_{(8-1000\mu m)}$ of IRAS-I are estimated based on the 12 μm, 25 μm, 60 μm and 100 μm fluxes using Equation 2.1 below according to Sanders & Mirabel (1996).

$$F_{IR} = 1.8 \times 10^{-14}\{13.48 f_{12} + 5.16 f_{25} + 2.58 f_{60} + f_{100}\}[Wm^{-2}], \tag{2.1}$$

where f_{12}, f_{25}, f_{60} and f_{100} are the 12 μm, 25 μm, 60 μm and 100 μm fluxes respectively. We compared the fluxes of galaxies belonging to the original PSCz and IIFSCz (duplicates) and checked if the F_{IR} values are the same. We found that IIFSCz is underestimated by approximately 30% at the lower flux end ($F_{IR} = 10^{-39.5}$ to $10^{-39.8}[Wm^{-2}]$). By comparing the two fluxes we made corrections to the entire IIFSCz fluxes using interpolation. However, the correction above ($F_{IR} = 10^{-39.5}[Wm^{-2}]$) is negligible (see Fig. 2.3).

Finally the far infrared luminosity, L_{IR}, is worked out from $L_{IR} = 4\pi D_L^2 F_{IR}[L_\odot]$, where D_L is the luminosity distance and defined as

$$D_L = (1+z)\frac{c}{H_o}\int_0^z \frac{dz}{\sqrt{\Omega_m(1+z)^3 + \Omega_\Lambda}}, \tag{2.2}$$

where Ω_m, Ω_Λ, H_o, z and c are the matter density, energy density, Hubble constant, redshift and speed of light respectively (Hogg 1999).

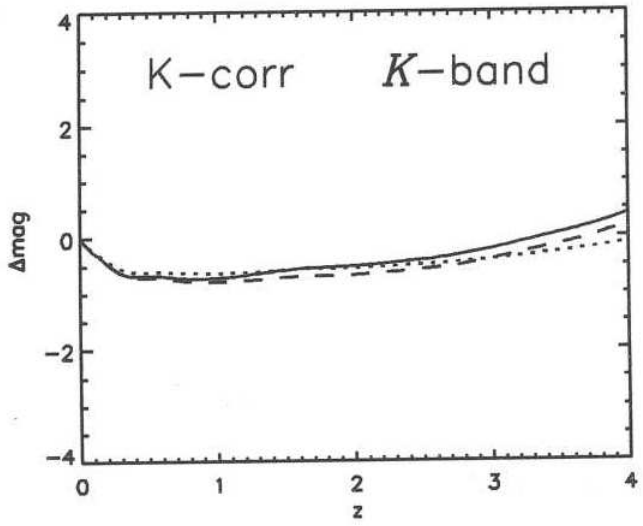

Figure 2.4: Δmag vs. redshift for three different types of SEDs.The solid line, the dashed line and the dots represent Sa, E0, Sc galaxies respectively. Note that in the local Universe ($z < 0.4$) the difference in Δ mag among the three SEDs is very negligible (adopted from Väisänen (2001)).

K-correction of PSCz and IIFSCz fluxes

Since the different magnitudes are not K-corrected, we K-corrected the K-band magnitudes of the IRAS-I. K-correction is dependent on the SED of the galaxy and specific filter used for the observation. However, in K-band at least up to z=0.2 the K-correction is almost independent of the galaxy type (independent of SED used) (Glazebrook et al. 1995) (see Fig 2.4). In addition, most of our galaxies are expected to be late type spirals anyway.

Based on the work by Väisänen (1996), a late type spiral SED model is used to come up with a relation between a multiplicative correction factor (K_c) and redshift. The relation is plotted in Figure 2.5. A straight line is fitted for the lower redshift end of Figure 2.5 and a numerical relationship of

$$K_c = 2.2\mathrm{z} + 1 \tag{2.3}$$

is found, where K_c and z are the multiplicative K-correction factor and redshift respectively.

The K-band magnitudes are then K-corrected using Equation 2.3 before they are used for estimation of other physical quantities. The K-corrected absolute K-band magnitude is given

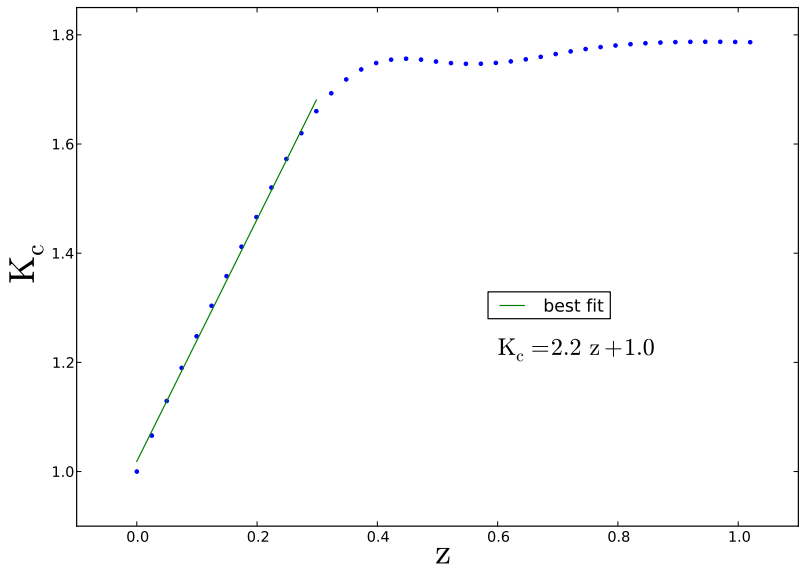

Figure 2.5: The K-correction adopted for the PSCz galaxies.

as:

$$M_K = -2.5\log(K_c\,(10^{-m_K/2.5})) - 5\log(D_L) + 5, \tag{2.4}$$

where M_K is the K-corrected K-band absolute magnitude and M_K is the uncorrected K-band apparent magnitude. The result is presented for PSC-I and IIFSCz-I separately in the left and right panels of Figure 2.6 respectively. It is noted that for the brightest galaxies, ΔM_K is as big as 0.4 for PSCz galaxies and as much as 0.23 for IIFSCz galaxies and in both cases the change is almost insignificant at the faint end of the galaxy distribution. This is the result of a selection effect both samples are subject to. At lower redshift, the data is dominated by low luminosity galaxies while at high redshift end only the brightest galaxies are detected and it is shown in Equation 2.3 above that the correction factor is proportional to redshift.

In both PSCz-I and IIFSCz-I cases the far-infrared flux is not K-corrected as the wavelength range it covers is so wide $(8 - 1000\mu m)$ that any K-correction effect is negligible.

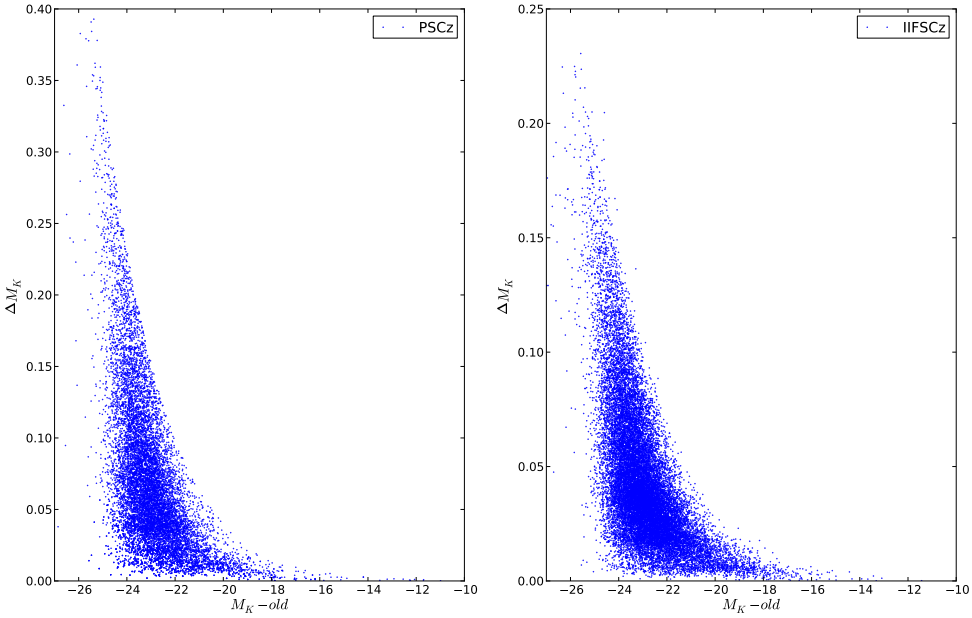

Figure 2.6: *Left panel*: The difference between the original and the K-corrected K-band magnitude vs. the original K-magnitude for PSCz-I sample. *Right panel*: The same relationship for IIFSCz-I. The correction is nearly zero at the low M_K end in both cases.

2.2.2 Density field samples

Several galaxy surveys have been conducted at optical (SDSS), far-infrared (IRAS) and in near-infrared (2MASS and 6dF) wavelength regime with main objective of reconstructing the galaxy density and velocity fields of the local Universe. All of them are subject to selection bias depending on the wavelength range they operate at. IRAS, being far-infrared sensitive, misses the early type galaxies while optical surveys tend to be affected by extinction especially at low galactic latitude. On the other hand near-infrared surveys are biased towards early-type galaxies and against the late-type ones. Understanding these biases, we used three catalogues (near and far-infrared selected) as a galaxy density field to make sure that our results are consistent.

PSCz

The entire PSCz catalogue without being matched with 2MASS is used as a density field to quantify the local environment around target galaxies and the final number of galaxies in this case is 14639. We call this sample the PSCz-II. The redshift distribution of this sample is shown in the right panel of Figure 2.1. Its level of completeness, uniformity and all sky coverage make

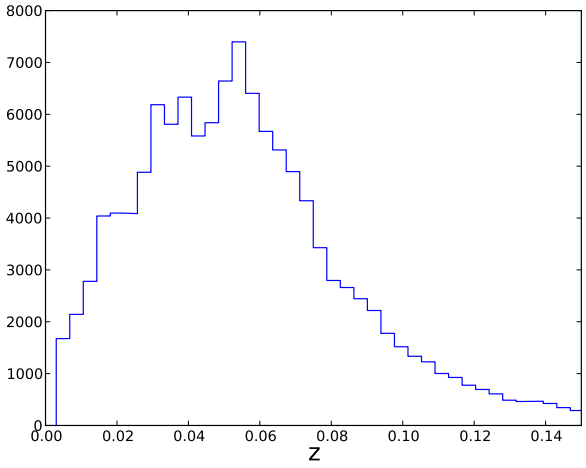

Figure 2.7: The redshift distribution of 6dF galaxies.

this sample suitable for density field measurements.

6dF Galaxy Survey

The 6dF Galaxy survey (Jones et al. 2009) is a southern hemisphere near-infrared-selected galaxy redshift survey of 150000 galaxies. Its initial target list came from many smaller surveys including 2MASS. For our purpose, it is used as a galaxy density field. This catalogue does not cover the full sky region of our target sample (IRAS-I), and in this respect it is not as good as our PSCz-II catalogue for estimating environments. However, it has the advantage that it is a much denser sample than PSCz-II and being K-selected, it may trace environment better than PSCz-II which is IR selected. It has a median redshift of 0.053 and goes as deep as $z \sim 0.14$ (see Fig. 2.7).

2MRS

The Two Micron All-Sky Redshift Survey (2MRS) is also used as a density field in this work. It is an all sky near-infrared redshift survey of 23000 galaxies with almost 99% completeness at a magnitude to $K = 11.25$ and $|b| \geq 5^{\circ}$ (Erdoğdu et al. 2006). It is not as deep as both PSCz and 6dF galaxies in its redshift coverage (see Fig. 2.8) but it has the advantage that it is much denser than PSCz below $z \sim 0.05$. Even if it does not add any additional advantage over the other two density field catalogues, it is used as consistency check.

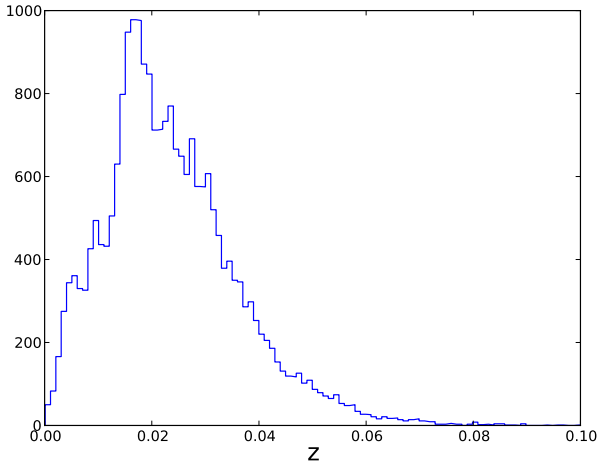

Figure 2.8: The redshift distribution of 2MRS galaxies.

2.2.3 The Sloan Digital Sky Survey (SDSS) data release 4 (DR4)

This work also made use of SDSS DR4. This sample is used both as a density field and as a target galaxy sample. The SFR for the sample was calculated from extinction corrected H_α emission line by Brinchmann et al. (2004). The spectroscopic and photometric data of DR4 were matched using galaxy ID in order to identify galaxies with redshift. In order to avoid any possible aperture effects at relatively small redshifts, galaxies below $z = 0.04$ are removed (Kewley et al. 2005) and the final redshift range used is $0.05 \leq z \leq 0.1$.

To summarise, our IR target galaxy sample is a merged sample of the PSCz-I and the fainter IIFSCz-I catalogues and we refer it as IRAS-I. To compute environments, we use the PSCz (PSCz-II), 6dF and 2MRS samples. In the case of the SDSS sample, we have used the same SDSS sample as a density field around SDSS galaxies. All samples are restricted to regions with $|b| > 10^\circ$ and $V > 1000$ km s^{-1} and cover similar redshift ranges.

2.3 Local density measurement

2.3.1 Why flux-limited?

In this work four flux-limited redshift surveys namely SDSS, 6dF, PSCz and 2MRS (see Section 2.2 for a detailed description of these samples) are used to quantify the local density around target galaxies which are IRAS-I (=PSCz+IIFSCz) and SDSS galaxies. The choice between using flux or volume-limited samples is determined by two factors:

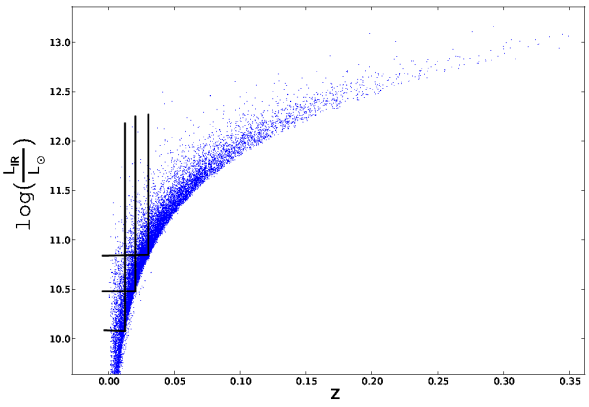

Figure 2.9: Attempts made to extract a volume-limited sample. It is very difficult to get a volume-limited sample which would both give a wide range of luminosity and a large number of galaxies. Any attempt to get a wider range of luminosity reduces the number of galaxies and vice versa.

1. Since this work primarily seeks to make a comparative study of the environments of LIRGs and non-LIRG IR ($L_{IR} \leq 10^{11} L_{\odot}$) galaxies, ideally it should cover a luminosity range as wide as possible both below and above $L_{IR} = 10^{11} h^{-2} L_{\odot}$ in the target sample (IRAS-I).

2. The spatial distribution of the density field samples must overlap with the target galaxy sample.

One possible way of doing this is to select a volume-limited sample in a wide luminosity range that includes $L_{IR} = 10^{11} h^{-2} L_{\odot}$ in a certain volume limit for the target samples. This means the resulting sample includes only galaxies above a certain luminosity limit and below a certain redshift. Once the redshift limit of the sample is known, the density field sample is defined by this redshift. However, given the nature (luminosity and redshift distribution) of the galaxy sample used as a target sample (IRAS-I), using a volume-limited sample is proved to be inefficient. It was found impossible to include at least 50% of the galaxies above $L_{IR} = 10^{11} h^{-2} L_{\odot}$ while still having a statistically large number of galaxies below $L_{IR} = 10^{11} h^{-2} L_{\odot}$. Figure 2.9 demonstrates attempts made to extract volume-limited samples from the PSCz-II sample. One can easily understand that any possible volume-limited sample from PSCz-II results in the inclusion of only a very small fraction of the total sample in the desired luminosity range and leaves out a considerably large proportion of otherwise usable galaxies sample.

In cases where the use of volume-limited sample is impossible, the other option is to use flux-limited samples. This allows the use of almost the entire available sample without any considerable reduction of the number of galaxies. However, there are issues one needs to be

aware of when using flux-limited samples. In using a flux-limited sample as a density field, one should be careful of a density bias both at high and low redshift ends of the sample. At higher redshift, low flux galaxies, galaxies whose flux is below the limiting flux of a survey, are missing and hence the density estimation is biased to high luminosity objects. At low redshift, on the other hand, high luminosity objects are missing too. First of all there are few high luminosity objects as compared to low luminosity objects at any redshift[2] and at the same time at low redshift the volume probed is small, and hence the representation of high luminosity objects, which are scarce already gets proportionally lower. As a result the density estimation at low redshift is biased towards low luminosity objects. For density estimation based on number count, this luminosity or size dependent bias is not as much as it would have been if density estimates were somehow weighted by mass or luminosity.

Because of the reasons discussed, this work makes use of flux-limited samples as a galaxy sample around which density field galaxies are counted. All the density field galaxy samples (PSCz-II, 6dF and 2MRS) are also flux-limited so that the target galaxy sample and the density field samples overlap spatially.

2.3.2 The cylindrical aperture for density measurement

Our choice of local density estimation method is motivated based on two main factors. Firstly, the method must have clearly defined geometry with fixed volume to ensure a consistent and uniform density measurement throughout the galaxy density field used. Secondly, the method must stand robust against redshift space distortion effects which are by far the most important factor affecting the density estimate.

Based on the above criterion, the aperture method with cylindrical geometry oriented in the line-of-sight direction is found to be the most reasonable and suitable option for our work.

Length of the cylinder

We have used a line-of-sight length of 1000 kms^{-1} in velocity space in order to reduce redshift space distortion effects in a wide variety of environments ranging from fields to clusters. In a cluster environment, where maximum redshift distortion effect is felt, a velocity dispersion is typically up to 1000 kms^{-1}.

Radius of the cylinder

Properties of galaxies such as SF, luminosity and colour are related to the galaxies' host virialized dark matter halo mass contained within a radius about 1 Mpc (Lemson & Kauffmann 1999, Blanton et al. 2006). Therefore, ideally a 1 Mpc radius sphere should give a good estimate of

[2]The luminosity function of galaxies shows a higher abundance of low luminosity systems than high luminosity systems

the local density. However, in our particular case, the space density of galaxies in the galaxy fields, especially in PSCz sample, gets substantially lower at higher redshift. Using a 1 Mpc radius at the higher redshift end, therefore, would not give a statistically large enough number of galaxies. Consequently, we chose to use 2 Mpc radius throughout.

2.3.3 Density measurements

For each of the IRAS-I galaxies, the number of PSCz-II, 6dF and 2MRS galaxies are counted in a cylinder with a radius of $2h^{-1}$Mpc and $10h^{-1}$Mpc. However, since these measurements are subject to redshift dependent incompleteness, correction is made for each of the individual counts. We refer to the number count of the density field galaxies as $X_z(z)$.

Correcting for redshift dependent selection effects and edge effects

As it is mentioned above, this work made use of flux-limited samples which go as deep as 0.15 (6dF and PSCz-II) and 0.1 (2MRS) in redshift as a density field. Due to this wide redshift range, there is indeed a redshift dependent incompleteness even above the luminosity limit at each redshift. The redshift distribution of all the three samples used as a density field is indicated in the top panel of Figure 2.10 and one can see that at higher redshift, the number of galaxies declines and this results in underestimation of the density measurement at higher redshift. We refer to this bias as redshift dependent incompleteness. It is worth mentioning that the redshift dependent incompleteness we mean here does not refer to missing galaxies because they are below the limiting luminosity of a survey. Following the discussion in Chapter 1 Section 1.3.5, we account for the redshift dependent incompleteness based on the actual observed distribution of galaxies in the surveys themselves.

A scaling factor, $s(z)$ (see Chapter 1 Section 1.3.5 for its definition), estimation is done by creating points in space that have random right ascension (RA) and declination (Dec) but similar redshift distribution and geometry with the real density field galaxies (PSCz-II, 6dF and 2MRS). The number of random points at each redshift is proportional to the number of density field galaxies at that particular redshift. The difference between the real density field and the random points is that the former has a clustering nature while the latter does not have any clustering because of the randomness in RA and Dec. Otherwise, both samples are subject to the same redshift dependent incompleteness and edge effects which are the most important feature of the random points in order to make the desired correction to the density field samples. Figure 2.10 shows the similarity of the redshift distribution of the random points in space and the real density field galaxies samples.

The number of random points in space produced for each of the three density field samples is 70 million. It is obvious that any increase in the random number can only make the estimation of $s(z)$, and consequently the scaling (correcting) for the incompleteness, even better. However,

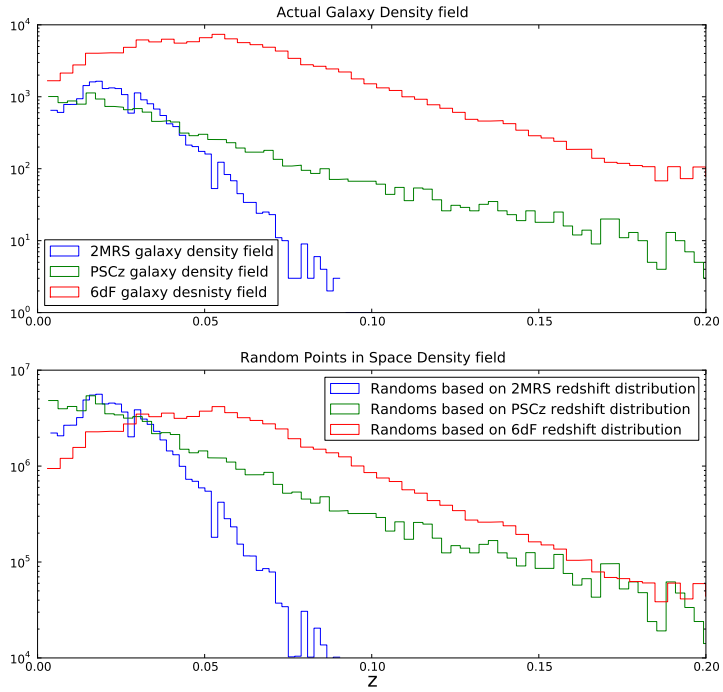

Figure 2.10: *Top panel*: The redshift distribution of the three galaxy density field samples. *Bottom panel*: The redshift distribution of the random points in space. The redshift distribution of the random points is similar to their respective real galaxy distribution so that the random points in space reflect the same redshift dependent incompleteness with real galaxy distribution.

we were limited by computational power which does not allow us to push the number any higher than 70 million.

Finally, the scaling factor is determined by making number counts of the random points around each target galaxy for each sample with the same geometry and size aperture. Since the points are distributed in random RA and Dec at each redshift, the determination of $s(z)$ at each redshift is done for each galaxy at each redshift instead of getting one value for all galaxies. However, this does not mean that the $s(z)$ values at different random points within each redshift are completely different. Though there are variations because of the random nature of the random points, in average $s(z)$ at each redshift reflects the correction that needs to be made at that particular redshift. In Figure 2.11, the variation of the mean $1/\bar{s}(z)$ across all RA and Dec combinations for each redshift, for all the three samples used as density field, is presented. Generally the plot shows that $1/\bar{s}(z)$ increases with redshift implying that there is a bigger correction at high redshift, where the real galaxy distribution is highly affected by

selection effects, than there is at low redshift ($z \rightarrow 0$), where the incompleteness effect is not that severe.

We used the same number of random points (70 million) to make redshift dependent incompleteness in all the three samples. However, this does not mean that the same scaling factor scales the three samples equally. This is because the three samples differ from each other in their flux depth (flux cut off at a certain redshift), redshift coverage and, above all, their incompleteness limit. In other words, the effect of the scaling in one sample cannot be compared to another. However, the important thing to note from the curves in Figure 2.11 is that the scaling at higher redshift is higher than the case at low redshift. The scaling curves in the figure reflect the general trend of the correction that needs to be done for the respective density field. In reality, however, there is a slight random variation in the correction from galaxy to galaxy at the same redshift because the random points at the same redshift have random RA and Dec - some points have slightly more random points than others around them. This situation could have been improved if the number of random points were sufficiently more than 70 millions.

Finally, again recalling the discussion in Chapter 1 Section 1.3.5, the scaled (the redshift dependent incompleteness corrected) density measurement is given as:

$$X_o(z) = \frac{X_z(z)}{s(z)}, \tag{2.5}$$

where $X_o(z)$ is the scaled density measurement.

Normalising the scaled densities

The density after the correction ($X_o(z)$) is a dimensionless quantity and it cannot tell us anything about the actual value of density except the trend. Moreover, the level of the corrected density depends on the size of the random number used in the process and it does not represent any absolute level. The higher the random number, the lower the density and vice versa.

In order to get a better sense of the level of the density estimation, the corrected dimensionless quantity is normalised by the mean density of galaxies of the density field galaxies. The entire process of determining this mean density is exactly the same as in the procedure described above, except that in this case the count is made around randomly chosen points in space. Firstly, the number density of the density field galaxies are made with the same size and geometry aperture (cylinder) around 10000 randomly selected points in space (random in RA, Dec and z). To correct for selection effects, around the same 10000 random points in space , random points from the 70 million random points are counted. The mean of the corrected density of the 10000 random points, defined as ($X_1(z)$), is given as:

$$X_1(z) = \ < \frac{X_r(z)}{s(z)} >, \tag{2.6}$$

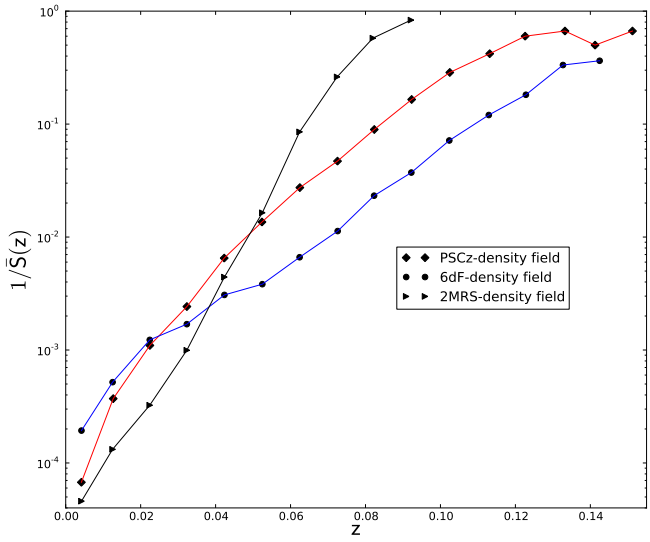

Figure 2.11: The distribution of the average value of $1/\bar{s}(z)$ with redshift for PSCz-II, 6dF and 2MRs galaxies. The distribution shows that the correction is higher at high redshift than at low redshift as the incompleteness is higher at higher redshift than it is at lower redshift.

where $X_r(z)$ is the corrected dimensionless density. The selection function, $s(z)$, used here is the same as the one used for the density estimation around the real galaxies. This is because in both cases, the real galaxy density field is the same. Finally, the average of all the corrected density values are taken to be the number that can normalise the $X_0(z)$ values for each of the target galaxies. The ultimate normalised and corrected density is given as:

$$X(z) = \frac{X_0(z)}{X_1}. \tag{2.7}$$

This means that the units of the density measurements are the mean density of the respective density field galaxies.

The distribution of the real density field galaxies and the corresponding random points have the same geometry and the same redshift range. As a result, whatever edge effects the real density field has, the random points have. This means that the selection function makes correction for edge effects too while correcting for the redshift dependent incompleteness.

The same procedure is followed in correcting the SDSS data. The only difference is that the SDSS sample has holes with complicated geometry in its spatial distribution and hence the random points have the same holes as the real galaxy sample.

2.4 SFR and stellar mass estimation

It is common for far-infrared emission to be used as a tracer for obscured SF (Kennicutt 1998a, Chary & Elbaz 2001). Being dominated by circumnuclear dust enshrouded SF, the SF of LIRGs and ULIRGs could be estimated using their far-infrared light. In Chapter 1 Section 1.5.3, we give a detailed description of the entire method that uses far-infrared emission in estimating the SFR of LIRGs.

The expression used for estimating SFR using L_{IR} from Kennicutt (1998a) is given as

$$\frac{SFR}{1\,M_{\odot}\,yr^{-1}} = \frac{L_{IR}}{2.2\times10^{43}\,erg\,s^{-1}} = \frac{L_{IR}}{5.8\times10^{9}\,L_{\odot}}. \tag{2.8}$$

We note that the above relationship assumes a continuous and constant SFR for a time scale of 10^8 yr and above, but some unknown fraction of our galaxy sample consists of strong starbursts which are expected to form stars in a shorter time scale. In other words these galaxies do not form star at a constant rate for a long period. It is therefore very important to keep in mind that the relationship used could introduce an uncertainty in the derived SFR. On the other hand, the relation is widely used in the literature even for strongly star-forming galaxies in the absence of better calibrations.

The K-band light is believed to originate mainly from the old stellar populations of galaxies and hence it is a good tracer of the stellar mass of galaxies. In this work, the relationship between K-band absolute magnitude and K-band $M_{\star}/L$ ratio from Bell & de Jong (2001) is used to derive stellar mass. The relationship used is based on a range of spiral galaxy evolution models and the accuracy is of a factor of 2. We estimated the value of $M_{\star}/L$ based on the K-band absolute magnitude of each galaxy. The estimate was made based on an analytic relationship derived from Bell & de Jong (2001) and presented as:

$$\log(M/L) = -0.0222M_K - 0.77. \tag{2.9}$$

Then the derived mass to light ratio for each galaxy is converted into stellar mass using $M_{K,\odot} = 3.33$.

At the high K-band absolute magnitude end, the relationship gives $log(M_{\star}/L)$ value of about -0.2 but most of the galaxies in this regime are high star forming ones (see the correlation between M_K and L_{IR} in Figure 2.12) which can have gas fractions up to even 60%. According to Bell & de Jong (2001), a gas fraction of 60% corresponds to a lesser value of $M_{\star}/L$. Therefore, using $log(\frac{M_{\star}}{L}) = -0.2$ results in a possible overestimation of the mass for the high star forming galaxies.

In addition, extinction and contamination from emission lines (e.g., Pa_{α} and Br_{γ}) near the K-band could also bias the mass estimate. The typical extinction of the K-band in LIRGs is up to $A_K \sim 0.3$ (Väisänen et al. 2008) which means that there is a possibility of underestimating the stellar mass by a factor of about 30%. The effect of emission lines can be very strong especially

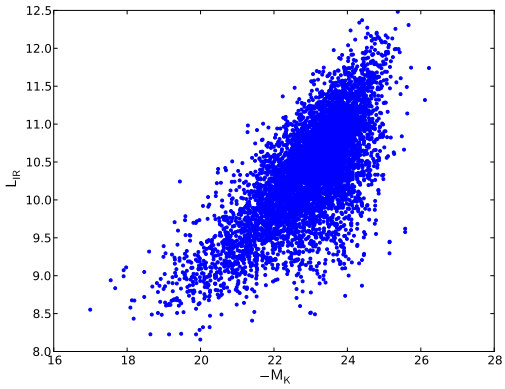

Figure 2.12: The relationship between L_{IR} and M_K for selected IR galaxies. Their M_K values are adopted from 2MASS.

with very young stellar populations (Zackrisson et al. 2008) and leads to overestimation, but it weakens for averaged stellar populations of various age (Rhoads 1998). The mass bias from the emission lines and extinction as a result is well within the overall uncertainty of the determination method in most cases and works in either direction.

Figure 2.12 clearly shows the existence of a correlation between M_K and L_{IR} though the scatter is high. The scatter is because the PSCz-I sample contains both blue (high star forming) and red (older stellar population) clouds of galaxies. Since the method employed to find the stellar mass is purely based on a spiral galaxy evolution model, it might not work for the red sequence galaxies as well as it works for the blue cloud galaxies.

2.5 Results

The mean local densities are estimated from three separate redshift surveys: 6dF and PSCz-II and 2MRS. The mean local density, and SFR and stellar mass estimate are made based on the technique described above in Sections 2.3 and 2.4 respectively. The relationships between these physical quantities with SF are explored with the main intention of understanding the connection between SFR and environments of local IR galaxies.

2.5.1 SFR or (L_{IR}) and density connection of LIRGs and non-LIRG IR galaxies

Here we explore how the density around local LIRGs and non-LIRG IR galaxies and their respective L_{IR} are compared. The densities are measured in $2h^{-1}$Mpc radius and $10h^{-1}$Mpc length following the discussion in Section 2.3. All of the panels in Figure 2.13 show the L_{IR}-

density relationship for IRAS-I galaxies using 6dF (panel a), PSCz-II (panel b) and 2MRS (panel c) galaxies as a density field. The L_{IR}-density data points are binned along L_{IR} in bins of 0.3. The error bars represent the standard deviation of the means which is given by $\sqrt{\frac{\sum(x_i-\bar{x})^2}{n(n-1)}}$. Sometimes the error bars are very small and difficult to see.

In all cases, we note that there is a clear difference in the environments of local LIRGs and non-LIRG IR galaxies. LIRGs live in an environment which is up to 100 times (panel a), 300 times (panel b) and about 10 times (panel c) as dense as the environments of non-LIRG IR galaxies while the non-LIRG IR galaxies live in an environment which is as dense as the respective density fields. It is important to remember the physical meaning of the densities. As it is mentioned in Section 2.3, density measurements are done in units of the mean density of the respective density field galaxies.

Moreover, above $L_{IR} \geq 10^{11} L_{\odot}$ in the case of panel a) (6dF density field) and slightly earlier in panel b) and c) (PSCz-II and 2MRS density fields respectively), the local density around LIRGs increases monotonically with L_{IR}. Analytical expressions for the relationship between L_{IR} and local density (ρ) around IRAS-I galaxies using 6dF, PSCz-II and 2MRS galaxies as a density field are respectively given as:

$$\log(\rho) = 1.5 \log(L_{IR}/h^{-2}L_{\odot}) - 16.4, \tag{2.10}$$

$$\log(\rho) = 1.5 \log(L_{IR}/h^{-2}L_{\odot}) - 17, \tag{2.11}$$

and

$$\log(\rho) = 1.47 \log(L_{IR}/h^{-2}L_{\odot}) - 15.2. \tag{2.12}$$

Figure 2.14 shows the SFR-density relationship for LIRGs and non-LIRG IR galaxies from IRAS-I sample using three separate density fields: 6dF (panel a), PSCz-II (panel b) and 2MRS (panel c). All plots are basically done by splitting the corresponding plots from Figure 2.13 into LIRGs and non-LIRGs IR galaxies and converting their L_{IR} into SFR and also binning in the other way as compared to Figure 2.13. The LIRGs, except in panel c, exhibit a SFR that increases with density which is the reverse of what is observed in the local Universe for normal galaxies (Kauffmann et al. 2004). The trend of the SF-density relationship measured for local LIRGs from 6dF and PSCz-II density fields is consistent with one another. On the other hand, though there is a clear correlation between the L_{IR} and local density of LIRGs when the 2MRS sample is used as the density field (see panel c) of Figure 2.13), the corresponding SFR-density relationship is not clear in panel c) Figure 2.14). However, it is important to note that there is a difference in the redshift depth across the three density samples. The 6dF and PSCz-II density field samples go as far as $L_{IR} \sim 10^{12} h^{-2} L_{\odot}$ in luminosity whereas the 2MRS sample goes only as far as $L_{IR} \sim 10^{11.5} h^{-2} L_{\odot}$).

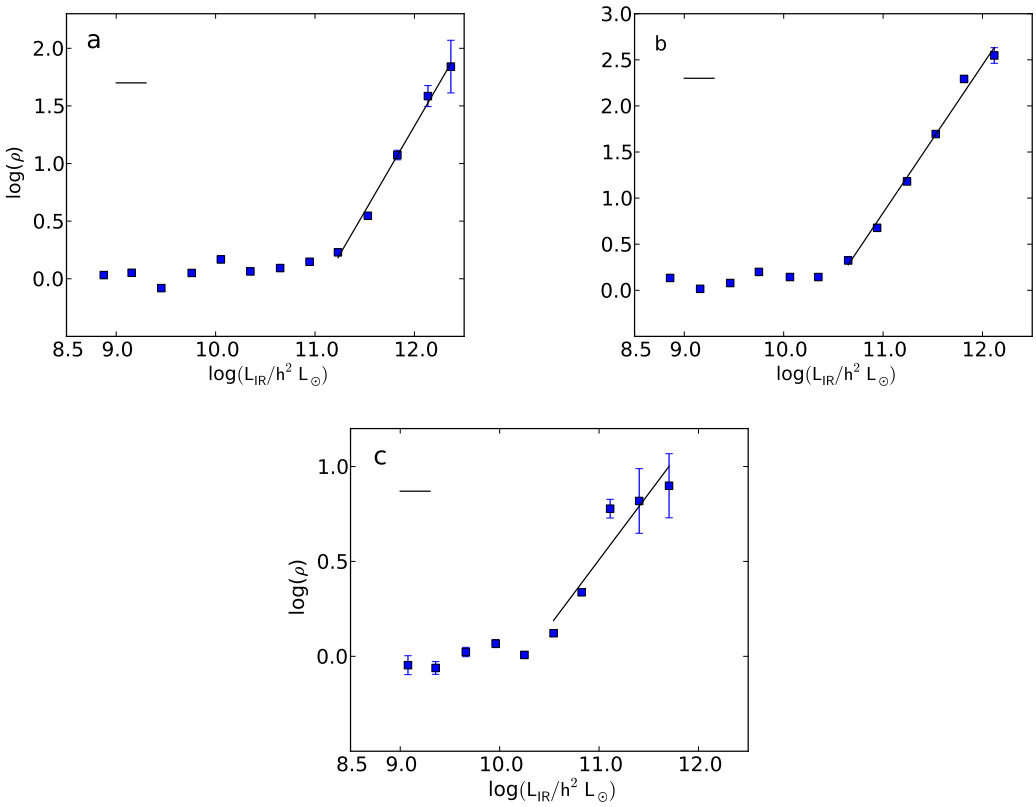

Figure 2.13: The relationship between L_{IR} and the mean local densities around IRAS-I galaxies. The mean local densities are estimated using three independent density fields: 6dF (panel a), PSCz-II (panel b) and 2MRS (panel c). The data points are binned along the density direction with a width of 0.3 (the black dash lines in the panel). In all the panels, the error bars represent the standard deviation of the mean in each bin. The three results show a similar trend that there is a dramatic difference in local density around LIRGs and non-LIRG IR galaxies.

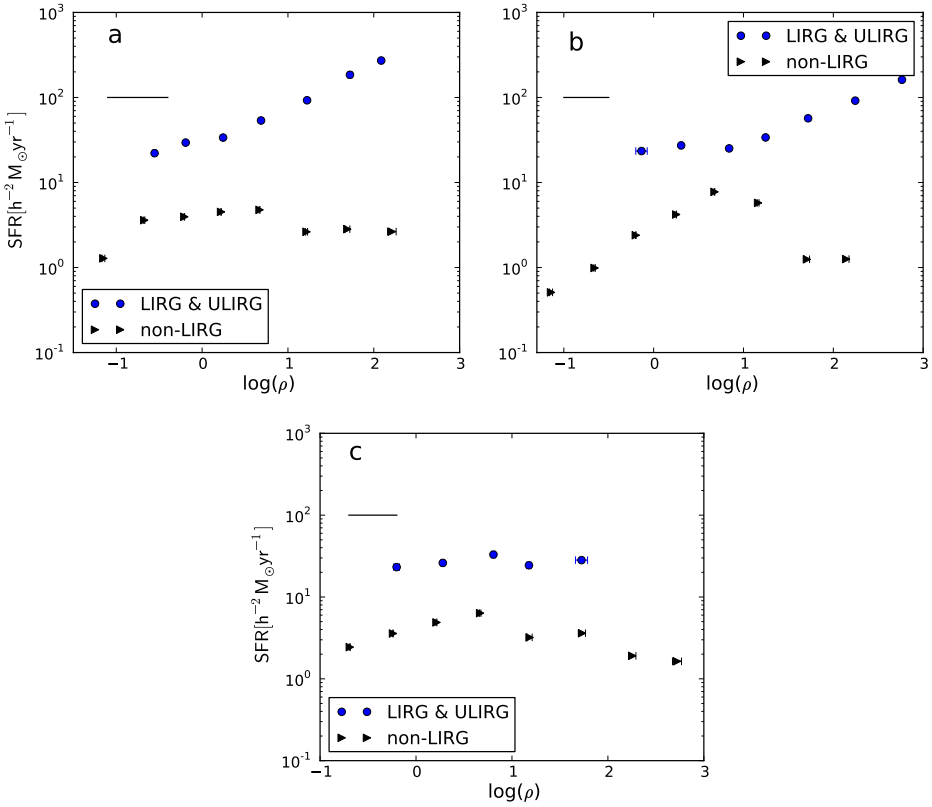

Figure 2.14: The relationship between SFR and the mean local densities around IRAS-I galaxies. All panels are similar to the panels a), b) and c) of Figure 2.13 except that here we split the entire IR galaxy sample into LIRGs and non-LIRGs and converted L_{IR} to SFR. The data points are binned along the density direction with a width of 0.5 (the black dash lines in the panel). In all the panels, the error bars represent the standard deviation from the mean for each bin.

2.5.2 Calibrating the density measurements into field/group/cluster

The density measurements are classified into the traditional environment classes: field, group and cluster based on galaxy systems[3] identified from a volume-limited sample which itself is extracted from our 6dF sample. The galaxy systems are identified using a friends-of-friends algorithm from Berlind et al. (2006) and their corresponding halo masses are estimated by matching their mass function with theoretical halo mass function (Quintero et al. 2005) (see Chapter 3 for a detailed description of the entire process of group identification and estimating halo masses for the identified groups). Densities around the centroid of each of the identified galaxy systems are measured using number counts of 6dF flux-limited density fields in exactly the same manner described above in Section 2.3 . Finally, a relationship between halo mass and density for the identified groups is established. The relations are presented in the left panel of Figure 2.15. A boundary between halo masses of field and group as well as between group and cluster is adopted from Kauffmann et al. (2004) and used to the measured densities using the established relationship between halo mass and densities to find the corresponding density boundaries. The adopted classification assumes that the field, groups and clusters have halo masses (M_{halo}) in the range: $M_{halo} \leq 10^{13} M_{\odot}$, $10^{13} M_{\odot} < M_{halo} \leq 10^{14} M_{\odot}$ and $M_{halo} > 10^{14} M_{\odot}$ respectively. In the right panel, we show the density boundaries derived from the halo mass and density relationships in the left panel. The density boundaries between field and group is found to be at $\log(\rho) = 0.2$ and between group and field it occurs at $\log(\rho) = 0.8$.

The results demonstrate that the IR galaxies with $L_{IR} \leq 10^{11} L_{\odot}$ in our sample dominate either field or near the boundary between field and group environments and LIRGs dominate group environments. One can also note that high L_{IR} LIRGs and low L_{IR} ULIRGs live in cluster environment.

2.5.3 SFR, specific star formation rate and stellar mass in IR galaxies

In the upper panel of Figure 2.16, we show the correlation between the stellar mass and SFR both for the LIRGs (blue points) and non-LIRG IR galaxies (black points). One can see that on average there is correlation between SFR and stellar mass except there is wide scatter especially at the high mass end, presumably contributed from two different populations of galaxies, i.e. one population has both high stellar mass and SFR while the other is with high mass but lower SFR. The solid line on the upper panel represents a maximum limit of SFR at a certain stellar mass. The same panel shows that though LIRGs are all massive galaxies, not all massive galaxies are LIRGs. Only massive galaxies with a high SFR are LIRGs.

In the lower panel, we presented the relationship between specific star formation rate (sSFR) (defined as $SFR/M_{\star}$) and stellar mass for both LIRGs and non-LIRG IR galaxies and it is clearly seen that the sSFR of both populations declines slowly with stellar mass. Moreover, at constant stellar mass, the LIRGs produce stars more efficiently than the other group.

[3]any galaxy system made of two or more galaxies bound together gravitationally

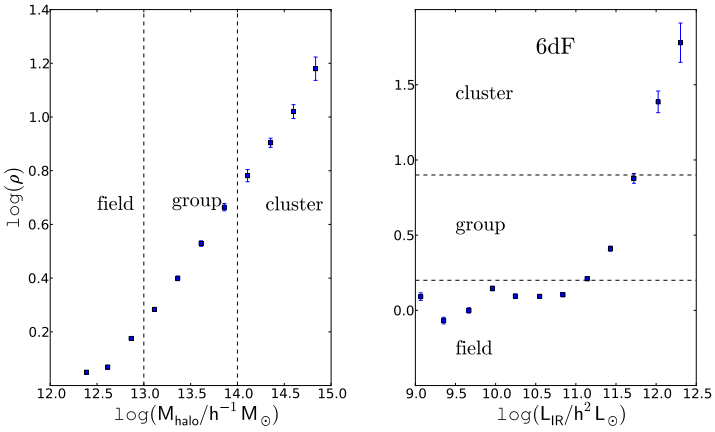

Figure 2.15: The density measurement around the IR galaxies including LIRGs is compared to the density measurement around the centroids of galaxy groups identified from 6dF galaxies in an attempt to calibrate the density measurements around the IR galaxies into field, group or cluster environments. The right panel represents the trend between the density measurements around the centroid of the galaxy groups and their corresponding halo mass whereas the plots on the right hand side represent the trend between the density around the IR galaxies and their L_{IR}.

2.5.4 Stellar mass (or M_K), star formation (or L_{IR}) and density

We reported that there is a connection between SFR or L_{IR} and local density around IRAS-I galaxies. Now we want to test if there is any connection between stellar mass (or M_K) and local density. If there is a relationship, we will investigate which one, i.e. L_{IR}-density at constant mass-density at constant value of L_{IR} is stronger. The three panels in Figure 2.17 are contour plots of M_K against L_{IR} for constant density.

Above $L_{IR} \sim 10^{11} h^{-2} L_{\odot}$, the density contours show a clear trend in all of the three panels. In panel b (6dF density field), we note that the contour lines take shape progressively as L_{IR} increases and gets completely vertical in the LIRG regime. On the other hand, in panel c (2MRS density field) the density contours take shape slightly earlier, at about $L_{IR} \sim 10^{11.5} h^{-2} L_{\odot}$. In the regime where the density contours are vertical, at a constant value of M_K, L_{IR} appears completely proportional to the mean density. There is no correlation between stellar mass (M_K) and mean density at a constant value of L_{IR}. Generally the correlation is weaker for the non-LIRG IR galaxies in both cases except the case in panel a.

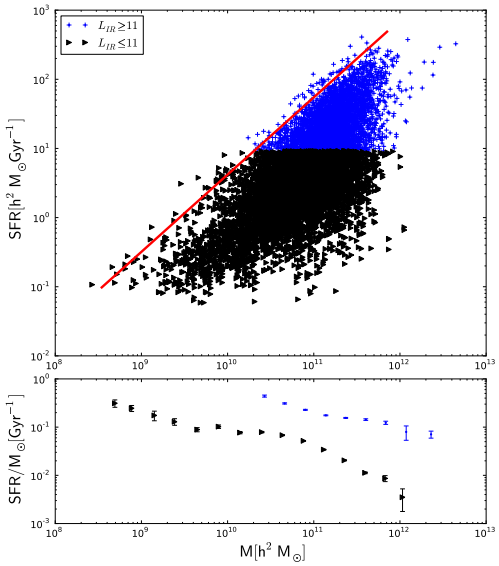

Figure 2.16: *Top panel*: SFR vs. stellar mass for both LIRGs (blue points) and non-LIRG IR galaxies (black points). SFR correlates with stellar mass; however, it shows wide scatter especially at the higher stellar mass end. The scatter seems to be the result of mixing of two different populations of galaxies (possibly red sequence and blue cloud) having two different relations between SFR and stellar mass. The red diagonal line demonstrates the existence of a physical limit in SFR at a given stellar mass. *Bottom panel*: The sSFR (specific SFR) of both LIRGs (blue points) and non-LIRG IR (black points) galaxies declines slowly with stellar mass. Moreover, at fixed stellar mass, LIRGs have a higher sSFR than non-LIRG IR galaxies.

2.5.5 Specific star formation rate, stellar mass and environment connection for local LIRGs

The SFR-density connection of local IR galaxies was explored in Section 2.5.1. In order to explore the origin of the relationship, we plot in Figure 2.18 and 2.19 how sSFR and $M_\star$ are related to their local environment both for LIRGs and non-LIRG IR galaxies. The density is estimated using 6dF in Figure 2.18 and using PSCz-II in Figure 2.18 as density field galaxies. The sSFR is calculated by taking the ratio of SFR and $M_\star$. Both the sSFR and $M_\star$ of non-LIRG IR galaxies show almost no dependence on environment (panels c and d in both figures). While the sSFR of LIRGs show a similar trend with the non-LIRG IR galaxies; the stellar mass of LIRGs is strongly proportional with their environment. This suggests that the origin of the SFR-density relationship of LIRG arises more from the stellar mass-density relationship they exhibit and the sSFR-density trend has less effect. The independence of SF and density in non

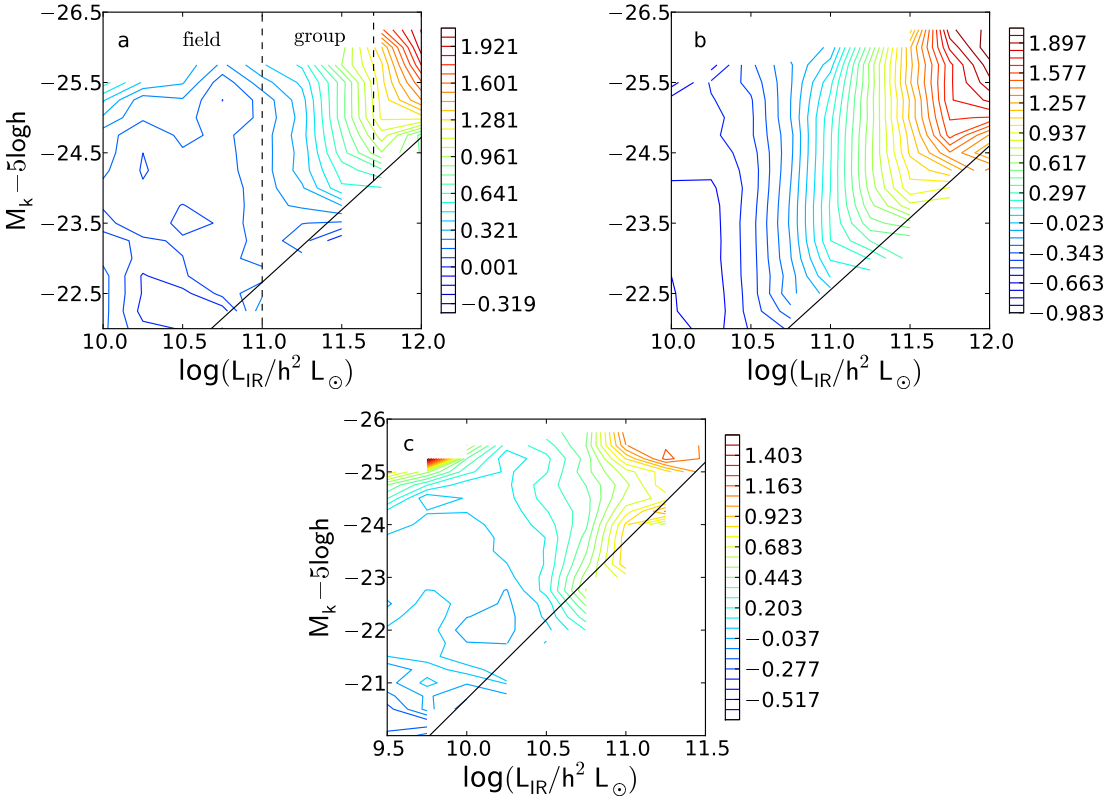

Figure 2.17: Local density as a function of both stellar mass (M_K) and SFR (or L_{IR}). Local density is measured using 6dF galaxies (panel a), PSCz-II (panel b) and 2MRS (panel c). All the three panels show contours of constant density, with the values of $\log(\rho)$ colour-coded to the right of each panel. The vertical dashed lines in panel a) denote the approximate transition between field, group, and cluster environments. In all the panels, density contours reflect the mean density in square bins of width 0.25 in both MK and log(LIR). At constant stellar mass, the SFR of local LIRGs is correlated with their local density. On the other hand, at constant SFR their stellar mass does not show any correlation with local environment. The solid diagonal lines in all the panels highlight that there is a maximum SFR that grows with stellar mass.

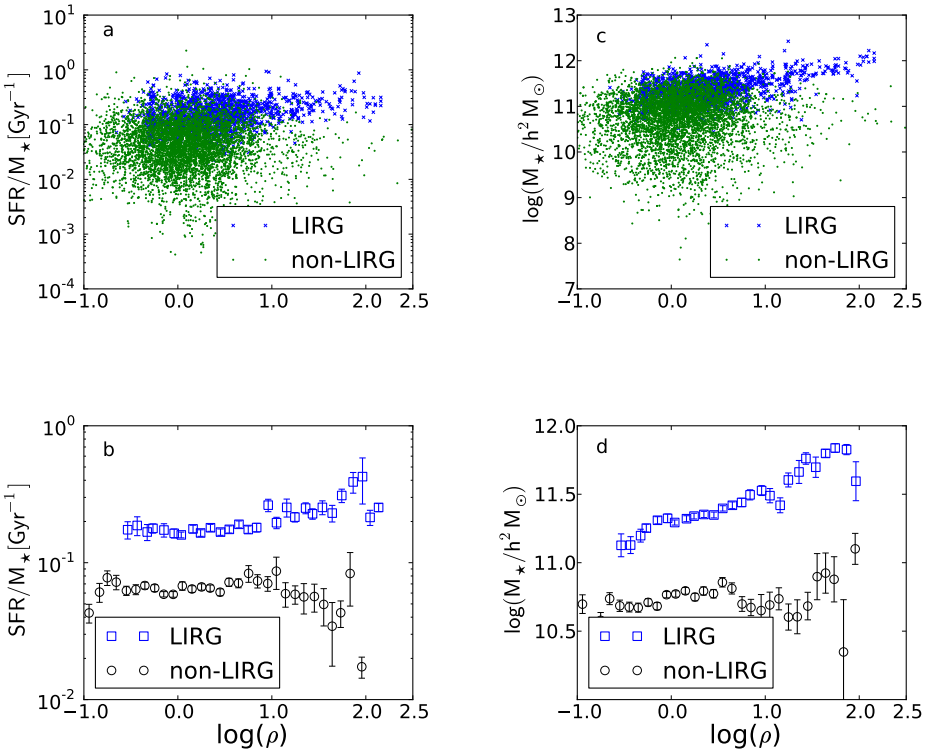

Figure 2.18: The SFR-density trend seen in LIRGs seems to be driven by the stellar mass-density relationship, and not by the sSFR-density relationship. Panels a) and b): $SFR/M_\star$ vs. local density. Panels c) and d): stellar mass vs. local density. The density in all the panels is estimated from 6dF density field. In all the panels blue points are LIRGs while black points are non-LIRGs. The top panels show all the galaxies as scatter-plots, whereas the bottom panels show average values of SFR/$M_\star$ and $M_\star$ in bins of local density. The binning both in panels b) and d) are done along the density axis with bin size of 0.1 and all the error bars represent the standard deviation from the means.

LIRG-IR galaxies, on the other hand, is because neither M$_\star$ nor sSFR exhibit a trend that shows a relationship with the environment.

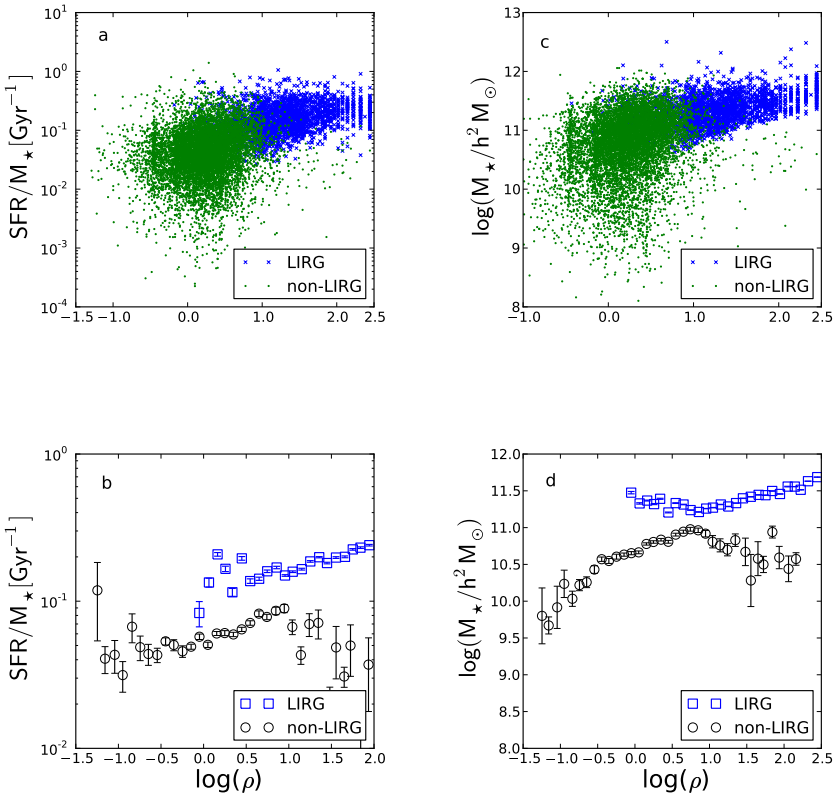

Figure 2.19: The SFR-density trend seen in LIRGs seems to be driven both by sSFR-density and stellar mass-density relationship. Panels a) and b): $SFR/M_\star$ vs. local density. Panels c) and d): stellar mass vs. local density. The density in all the panels is estimated from PSCz-II density field. In all the panels blue points are LIRGs while black points are non-LIRGs. The top panels show all the galaxies as scatter-plots, whereas the bottom panels show average values of SFR/$M_\star$ and $M_\star$ in bins of local density. The binning both in panels b) and d) are done along the density axis with bin size of 0.1 and all the error bars represent the standard deviation from the means.

2.6 Discussion

2.6.1 Validity of the result

PSCz-II, 6dF and 2MRS as density fields

Since different galaxy types cluster differently, they do not trace the underlying mass distribution of the Universe in the same way (see Section 1.4.1 in Chapter 1) (Lahav & Suto 2004). We have used PSCz-II and 6dF and 2MRS galaxies to quantify the local density local LIRG and non-LIRG IR galaxies. It is known that PSCz-II (IRAS selected) galaxies and mass are not well correlated (Taylor et al. 2001). On the other hand, 6dF and 2MRS being near-infrared selected, their mass is lower than than the PSCz-II's bias.

While we do not see a fundamental discrepancy in the results found using all the three samples as an overdensity tracer in this work, we have seen some minor issues. The upturn point in the L_{IR}-density relationship occurs approximately at $10^{11}L_{\odot}$ when 6dF galaxies are used as an overdensity tracer but when PSCz-II and 2MRS galaxies are used as an overdensity tracer, it occurred slightly before $10^{11}L_{\odot}$. In the contour plots, when PSCz-II is used as an overdensity tracer, we see a strong well defined vertical pattern but 6dF produces a slightly weaker pattern. Though it is difficult to make a proper comparison on the 2MRS sample contour plot as the sample does not go as deep as the other two samples in redshift, it is possible to see weak vertical contour lines roughly above $10^{11.5}L_{\odot}$. Overall, given the main intention of this work which is trying to find any possible trends using the three samples as a density tracer, we believe all produced consistent results.

Testing our density estimation method

We have tested our density estimation method using a flux-limited SDSS sample (Section 2.2.3), if indeed the method we employed reproduces the locally expected (declining SFR-density) trend. Based on the explanation in Section 2.3 ,the density around SDSS galaxies are estimated in $2h^{-1}$Mpc radius and $10h^{-1}$Mpc length cylinder using SDSS galaxies themselves as a density field. The estimated density versus SFR relationship is shown in Figure 2.20 and it indeed reflects what is normally expected in the local Universe. The SFR decreases monotonically by five orders of magnitude for a density increase of nearly one order of magnitude. The general trend found is in agreement with other results done on SDSS galaxies and it is in agreement with what is normally expected in the local Universe (Gómez et al. 2003, Kauffmann et al. 2004). The same result will be used in Section 2.6.6 as a comparison for the SFR-density trend for local LIRGs with other local galaxies since the methods used to estimate density are consistent with each other.

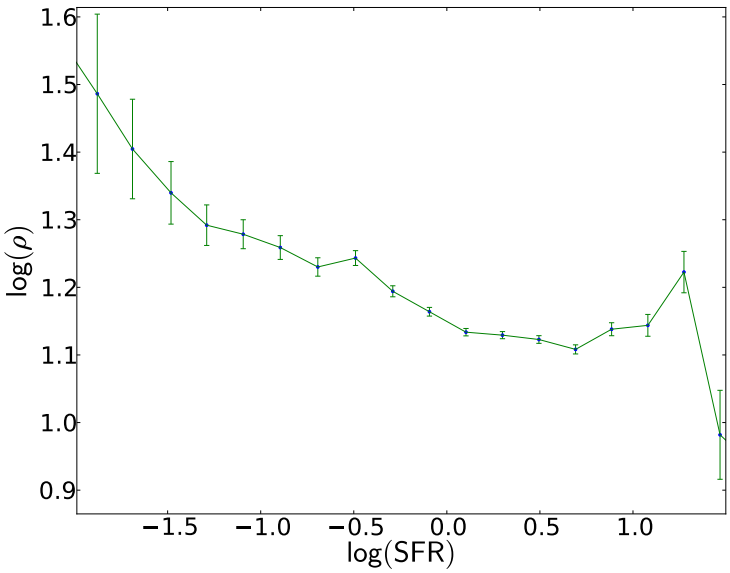

Figure 2.20: The density measurements are made by counting the SDSS galaxies themselves around SDSS galaxies. The bin size is 0.2 and the binning is in SFR axis. The relationship reflects the normal SFR-environment relationship expected in the local Universe.

2.6.2 The relevance of $L_{IR} = 10^{11} L_{\odot}$

We have shown that local LIRGs live in an environment denser than non-LIRG IR galaxies. According to the upper two panels of Figure 2.13, the far-IR luminosity, $L_{IR} = 10^{11} h^{-2} L_{\odot}$, is not only a matter of numerical convenience to distinguish between the two populations of IR galaxies. This luminosity point also marks a clear boundary (difference) in the environments of IR selected galaxies. This possibly means that LIRGs are a different galaxy population than other IR galaxies with $L_{IR} \leq 10^{11} h^{-2} L_{\odot}$ and the difference is at least partly environmentally triggered.

Several studies demonstrated that there is a symmetry difference in the physical shape between moderate and high IR-emitting galaxies, although they do not pinpoint exactly where the boundary is. Almost all Es and S0s exhibit an insignificant amount of IR activity with $L_{IR} \leq 10^{9} L_{\odot}$ (Young et al. 1984) whereas Sa to Sc type spirals produce $L_{IR} \geq 10^{8} L_{\odot}$ (Rieke & Lebofsky 1986). Neugebauer et al. (1984) found that up to 25% of LIRGs are peculiar or interacting while IRAS galaxies with $L_{IR} > 3 \times 10^{12} L_{\odot}$ are entirely classified as interacting or merging (Sanders & Mirabel 1996). Similarly, Melnick & Mirabel (1990) showed that the fraction of interacting systems increases from nearly 10% to 100% for L_{IR} value increase from $10^{10.5} - 10^{11}$ to 10^{12} and above. Putting together sequentially the L_{IR} values of these galaxies

with their corresponding morphology and taking into account the fact that morphology somehow reflects the level of interaction of galaxies, there is indeed an indication for a correlation between their IR activity and degree of interaction.

If the level of morphological asymmetry/interaction of galaxies reflects the environment they live in (see e.g. Ellison et al. 2010), then the morphological transition at luminosity $L_{IR} = 10^{11} L_{\odot}$ should also mark a transition in the environments of IR-selected galaxies. The result of this work confirms that there is indeed dramatic density difference above and below $L_{IR} = 10^{11} L_{\odot}$ and in other words, the asymmetry difference in the physical appearance witnessed around this luminosity point may be a direct reflection of this dramatic environmental difference.

From this result, it is clear that there is a certain environmental threshold above which galaxies are expected to experience the extreme SFR seen in LIRGs. However,this may depend on other physical characteristics as well, for example gas fraction. Why exactly $L_{IR} = 10^{11} L_{\odot}$? This question is beyond the scope of this work and it needs detailed studies of the physical characteristics of IR populations of galaxies above and below the $L_{IR} = 10^{11} L_{\odot}$ luminosity limit and the local mass distribution around them.

2.6.3 Correlation between SFR and environments of local LIRGs

Photometric studies made on the morphology of local LIRGs agree that these galaxies have a highly disturbed morphology which is a signature of interactions they have undergone (Sanders & Mirabel 1996). However, it is not clear in what fashion the environmental influence (interaction) and their IR activity are related. We understand that their environment is not only denser than that of non-LIRG IR galaxies, but we also found that L_{IR} (or SFR) of LIRGs is monotonically proportional to the richness of their local environment (see Fig. 2.14 and Fig. 2.17).

An independent work by Melnick & Mirabel (1990) found that the morphology (interaction) of (U)LIRG systems is systematically proportional to their L_{IR} output. Since merger (interaction) probability is a function of environmental richness, the morphology-IR activity witnessed in (U)LIRGs is the direct reflection of the IR-environment correlation shown in this work. Therefore, the IR activity of LIRGs is at least partly interaction driven and also their L_{IR} (SFR) can be considered as a tracer of the their interaction. The same trend has been witnessed among $z \sim 1$-LIRG groups (Elbaz et al. 2007). Elbaz et al. (2007) found in GOODS field that the intrinsic luminosity of LIRGs increases with the local galaxy density around them, with the most luminous ones living in the centre of a cluster.

Looking at (U)LIRGs as a product of two gas-rich isolated interacting systems without the effect of the bigger scale environment, Sanders & Ishida (2004) found that the mean distance between interacting companions amongst (U)LIRGs declines with L_{IR} (see Fig. 2.21). The mean distance decreases from 30 kpc at $log(L_{IR}/h^2 L_{\odot}) = 11.3$ to almost about zero at $log(L_{IR}/h^2 L_{\odot}) = 12.5$. The most obvious conclusion one can draw from their work is that any interaction between two gas-rich galaxies would experience different value of L_{IR} at different

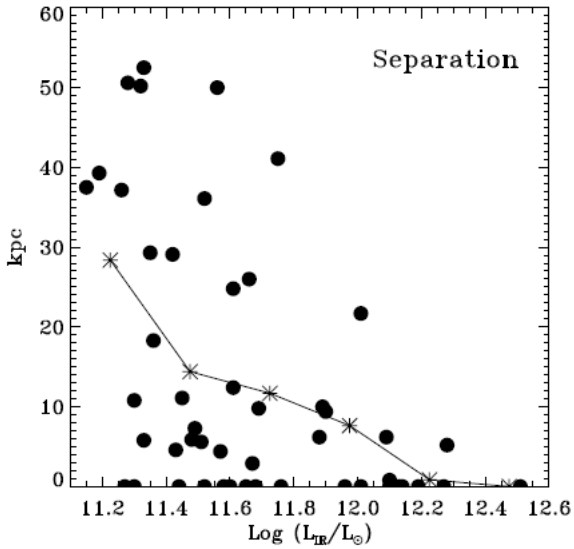

Figure 2.21: The mean distance between the nuclei of interacting pairs declines with L_{IR} (adopted from Sanders & Ishida 2004).

stages of the interaction. This leads to a scenario where (U)LIRGs of different L_{IR} values are basically similar types of gas-rich galaxies seen at their different stage of interaction (possible evolutionary scenario).

We, on the other hand, have shown that the large scale environment of (U)LIRGs is correlated with their L_{IR} at least to $log(L_{IR}/h^2 L_{\odot}) = 12.5$. According to our result, every increase of L_{IR} is associated with an increase in the surrounding density. This scenario seems to contradict with the above mentioned possible evolutionary sequence among (U)LIRGs. Because, if one expects an evolutionary connection amongst (U)LIRGs, then the correlation between their bigger scale environment (2 Mpc scale) and L_{IR} should not be necessary. This disagreement between the two scenarios leads to a question about the connection between the density of large scale environment (2 Mpc) and the one-to-one interactions of galaxies.

What is the maximum density environment that LIRGs are expected to reside in? Does the trend between SFR (or L_{IR}) seen in Figure 2.14 and Figure 2.17 continue in the same manner even past the LIRG regime and extend to the ULIRG regime? Do we see them in clusters? If so, where in clusters, outskirts or cores of clusters? There are indications at high redshift Universe that higher L_{IR} LIRGs are found in cluster cores (Elbaz et al. 2007). On the other hand, locally the highest density environments observationally confirmed to host LIRGs are the outskirts of clusters (Laag 2006, Duc et al. 2004, Lemonon et al. 1998, Kleinmann et al. 1988). Based on the well established knowledge of SFR-density relationship at the local Universe, we argue that

the relationship between SFR (or L_{IR}) and local density around ULIRGs would not be similar with the relationship for LIRGs. This is because if the environment is very dense, then galaxies move very quickly and will not have enough time to interact and form stars to the level seen in ULIRGs.

2.6.4 Does the 2 Mpc scale environment have an effect?

As it is discussed in 2.3.2, normally it is the $1h^{-1}$ Mpc scale environment of galaxies that correlates strongly with the spectroscopic properties of galaxies such as colour and luminosity. A comparison of the relationship of different scale environments and SF properties of galaxies revealed that the environment at more than 1 Mpc scale does not have an important implication on the SF property of galaxies (Lemson & Kauffmann 1999, Blanton et al. 2006).

The environment in this work is quantified at $2h^{-1}$ Mpc scale and the result shows that the environment at this scale is correlated with L_{IR}. However, this does not necessarily mean that it is the $2h^{-1}$ Mpc scale that influences the SF of the IR-galaxies. It could be that the result is a mere consequence of one of the following:

- the inclusion of the $1h^{-1}$ Mpc scale environment within the $2h^{-1}$ Mpc scale environment
- the density in the 1 Mpc scale is correlated with the density outside of the 1 Mpc radius
- the 2 Mpc scale environment has indeed an influence by itself but not as a result of the above two factors
- a combination of the above two

Though it is not very easy to resolve the issue, we have tried to remove the inclusion of the 1 Mpc scale density from the 2 Mpc scale and checked if the effect still exists. We have estimated the environment within an *annulus* of $(1-2)h^{-1}$ Mpc. If the environment beyond the $1h^{-1}$ Mpc has no effect, one should not see any correlation between L_{IR} and density measured in this plot. However, Figure 2.22 shows that the same trend seen with $2h^{-1}$ Mpc is observed in $(1-2)h^{-1}$ Mpc scale also. This result implies that in fact the effect observed at 2 Mpc scale is not because of the inclusion of the inclusion of the 1 Mpc scale environment. It is rather either because of the correlation of the environment above the 1 Mpc scale environment to the 1 Mpc environment or it could also be because the density at 2 Mpc environment indeed matters.

2.6.5 The stellar mass, SFR, sSFR and environment of LIRGs and non-LIRG IR-galaxies

The stellar mass, SFR and environment

Normally, the SF of a galaxy is dictated by three very important factors: the gas content, its stellar mass, and by the environment in which it lives (Kauffmann et al. 2004). Depending

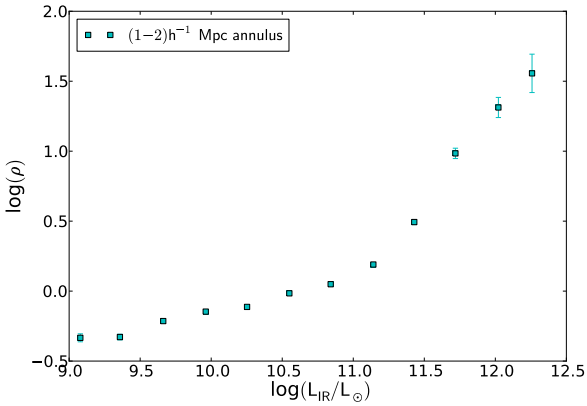

Figure 2.22: The relationship between L_{IR} and environment in annulus of $(1-2)h^{-1}$ Mpc scale. The relation shows that the L_{IR} activity of LIRGs is correlated not only with the small scale environment but also with the large scale environment.

on these two factors, a range of SFR is expected. According to Figure 2.17, local IR galaxies including LIRGs exhibit a correlation between their L_{IR} (measure of SFR) and environment at constant M_K (or stellar mass) but they do not show any clear correlation between stellar mass and density at constant SFR. No matter what the stellar mass variation is, IR galaxies in similar density environments tend to have the same SFR. The implication is that the SF property of local IR galaxies is controlled by their environment regardless of their stellar mass. It seems that there is a minimum stellar mass threshold which galaxies have to have in order to be IR galaxies at a certain environment and above that stellar mass threshold; the stellar mass increase does not have any impact on their IR activity. Once galaxies become IR galaxies and acquire a certain SFR, regardless of their mass they need to be transferred to another density environment in order to change their SFR. This basically tells us that at constant stellar mass, galaxies might have different SFR based on their environment.

The minimum stellar mass galaxies have in order to be IR galaxies, or in this case specifically LIRGs, correlates with both L_{IR} and the local environment around them. We have derived an analytical expression between the minimum M_K and the corresponding L_{IR} in all the three density fields in producing the three panels in Figure 2.17. The best fit represented by the black line in panel a) and b) is represented by Equation 2.13 and in c) it is represented by Equation 2.14 below.

$$M_K = -2.05 \log(L_{IR}). \tag{2.13}$$

$$M_K = -2.99 \log(L_{IR}) + 9.2. \tag{2.14}$$

These diagonal lines in all the panels indicate a physical limit to stellar mass that can support the existence of IR galaxies at a given L_{IR}. In the cases of panels a and b where 6dF and PSCz-II density fields are used as a background density, the slopes of the lines are the same whereas in the case of panel c) the slope is quite different. According to the results, the minimum stellar mass grows linearly with L_{IR}. This limit in the stellar mass is of the same origin to the physical limit in M_K indicated by the diagonal line in the upper panel of Figure 2.16.

This limit traces its origin to the famous Kennicutt-Schmidt law that relates the mass in stars formed per unit area per unit time (similar quantity with SFR) ($\dot{\Sigma}_\star = \dot{M}_\star/area$) to the gas surface density (Σ_{gas}) (Schmidt 1959, Kennicutt 1998b). The rule in terms of the two quantities is given as:

$$\dot{\Sigma}_\star \propto \Sigma_{gas}^N, \tag{2.15}$$

with the power N ranging between 1 and 2. One can see that the SFR (as it is represented by the right side of Equation 2.15) is a power-law correlation with the surface density of the gas. Given the logarithmic nature of the Equations 2.13 and 2.14 we derived for the physical limit of SFR for a given stellar mass (see also the limit in Fig. 2.16), we note that they are very similar to the Kennicutt-Schmidt power-law relationship. It might be possible to derive physical SF constraints for IR galaxies using the envelopes of the distributions both in Figure 2.16 and 2.17. However, in this work we did not pursue this further.

The stellar mass difference between LIRGs and non-LIRG IR-galaxies

From the upper panel of Figure 2.16, we note that on average local LIRGs have a higher stellar mass than the non-LIRG IR galaxies and in addition, their stellar mass is correlated with their SFR though it is not clear how exactly the stellar mass influence is manifested in their SF activity. One possibility is that LIRGs at the high stellar mass end are at their latter stage of interaction (possibly completely merged with a stellar mass of at least two progenitor spiral galaxies) in which their IR-activity has reached its peak.

However it is not clear if stellar mass is the only factor differentiating between the SF activity of LIRGs and non-LIRGs. In order to investigate this, we study the specific SFR (sSFR) of LIRGs and non-LIRG IR galaxies. In the lower panel of the same Figure 2.16, we learn that local LIRGs have higher sSFR than the non-LIRG IR galaxies. For the same stellar mass, local LIRGs then produce stars more efficiently than the non-LIRG IR galaxies. This confirms that the very reason why local LIRGs are LIRGs is not only because they are higher stellar mass systems on average than non-LIRG IR galaxies, but that it is also because they produce stars at a higher efficiency than non-LIRG IR galaxies.

Though local LIRGs have higher sSFR than non-LIRG IR galaxies for a given stellar mass, their sSFR slowly declines with stellar mass (lower panel of Fig. 2.16). This may mean that another factor is suppressing SF activity in LIRGs as their stellar mass increases. Despite the

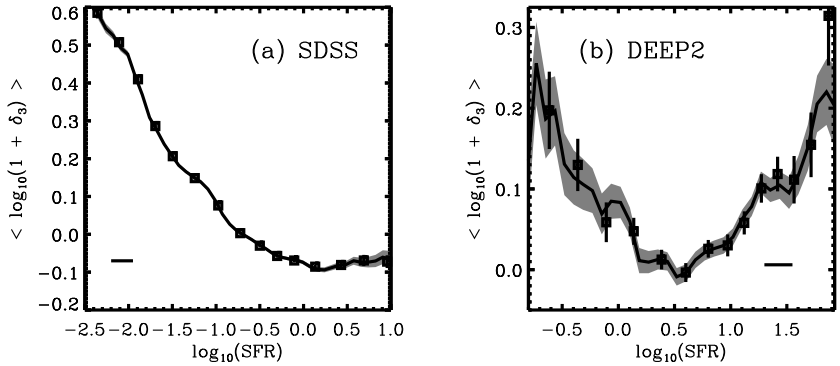

Figure 2.23: *Left panel*: The density-SFR for $z \sim 0$ galaxies. *Right panel*: The density-SFR for $z \sim 1$ galaxies. The local Universe is dominated with a population of galaxies whose SF anti-correlates with environment while the high redshift Universe has two types of population with different SF-density relationship (adopted from Cooper et al, 2008)

effect of this unknown SF suppressing factor, the total SFR grows proportionally with stellar mass, implying that the effect of stellar mass is much stronger than any effect that suppresses SF in LIRGs. It is known that the strength of AGN feedback activities correlates with stellar mass of host galaxy; the stronger AGN feedback, the stronger the suppression of SF. It could then be possible that what is suppressing the SF activity is the influence of AGN feedback in the central regions.

2.6.6 The reversal of SF-density trend in the local Universe and the possible origin of local LIRGs

The SF-density relationship found for SDSS galaxies ($z \sim 0$ galaxies) in Figure 2.20 is consistent with other results for SDSS galaxies (Gómez et al. 2003, Kauffmann et al. 2004) and it is also the reverse of what is observed for blue cloud galaxies at $z \sim 1$ (Cooper et al. 2008, Elbaz et al. 2007). A comparison made by Cooper et al. (2008) between low (SDSS) and high (DEEP2) redshift galaxies using projected surface density based on the 5^{th} neighbour galaxy, show clear evolution of SFR-density relationship with redshift. At $z \sim 1$, SFR decreases for red sequence galaxies and then increases for blue sequence galaxies with environment (V-shaped trend see panel b of Fig. 2.23).

The highest (bright massive blue galaxies) and lowest SF (massive red sequence galaxies) are both found in denser environments than the intermediate ones. On the other hand this relationship is reversed in the local Universe. Locally, SFR declines with density regardless of their type (see panel a of Fig. 2.23).

While the existence of a galaxy population whose SF anti-correlates with density is normal

at both redshifts, at $z \sim 1$ there is another population whose SF correlates with its local density (blue cloud galaxies). This population does not have any counterpart in the local Universe according to the common understanding of SF-environment. It is believed that most of the blue cloud galaxy population at high redshift has possibly evolved into the red-sequence galaxies at $z \sim 0$ and resulted in the lack of a galaxy populations whose SF correlates with environment at the local Universe. This is exactly what we see in the SF-density relationship of SDSS galaxies in Figure 2.20. The result reflects the absence of a population of galaxies whose SFR correlates with density and it is this difference between the trends at $z \sim 0$ and $z \sim 1$ that we mean by the "reversal of SF-relationships".

The SF-density trend observed for local LIRGs in this work is similar to the relationship observed for $z \sim 1$ blue galaxies: SFR increases with local density (see Fig. 2.14). Combining the SF-density relationship found for SDSS galaxies (see Fig. 2.20) and the result for local LIRGs (see Fig. 2.14), we tried to construct a complete picture of SF-density relationship in the local Universe. This trend is a identical to what is observed at $z \sim 1$ (V-shaped trend): the SFR first decreases and then increases with local density. We argue that the difference between the SF-density trend found by Cooper et al. (2008) and our result arises because the SDSS data in Cooper et al. (2008) does not probe the highest SF galaxies such as LIRGs and non-LIRGs. Even if they are optically detected to be part of SDSS, their effect is weakened by the general galaxy populations. Otherwise, apart from the difference in the number density of extreme star forming galaxies such as LIRGs and ULIRGs, the entire SFR-density relationship is similar with the relationship at $z \sim 1$.

The similarity in the SF-density relationships between local LIRGs and $z \sim 1$ blue cloud galaxies gives clues as to their possible formation mechanism and the origin of local LIRGs. The fact that local LIRGs exhibit the same SFR-density trend with $z \sim 1$ blue cloud galaxies together with their sharp drop in number density since $z \sim 1$ to $z \sim 0$, could mean that they might be population of galaxies that survived whatever process that has been transforming the blue population of galaxies between $z \sim 1$ and the present.

Contrary to our finding, Hwang et al. (2010) using IR galaxies with $L_{IR} \geq 10^{10} L_{\odot}$ found that SFR is not correlated with environment and concluded that the SFR-density relationship of these galaxies is similar to local galaxies. We believe that the presence of galaxies with $L_{IR} \leq 10^{11} L_{\odot}$ in their sample weakens the relationship we have observed in Figure 2.13. Also the density measurement they have used is quite different to the one we have used.

Cooper et al. (2008) showed that the observed difference in the SFR-density relationship between SDSS and DEEP2 galaxies is the reflection of the difference in stellar mass-density relationship between them. Taking B-band absolute magnitude (M_B) as a proxy for stellar mass, they showed that M_B is proportional to density for DEEP2 blue galaxies but not for SDSS galaxies (see Fig 4.9). They further argued that the difference between $z \sim 0$ and $z \sim 1$ SFR-density trend has nothing to do with sSFR-density relationship.

sSFR declines with environment both for SDSS and DEEP2 galaxies (DEEP2 blue cloud

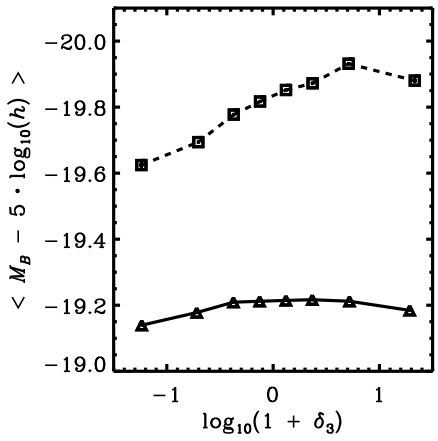

Figure 2.24: The mean absolute B-band magnitude, MB for blue galaxies in the SDSS (solid line and triangles) and DEEP2-A (dashed line and squares) samples, in bins of local galaxy overdensity, $1 + \delta_3$. While the mean MB shows little dependence on environment for nearby blue galaxies, there is a much stronger dependence (adopted from Cooper et al, 2008)

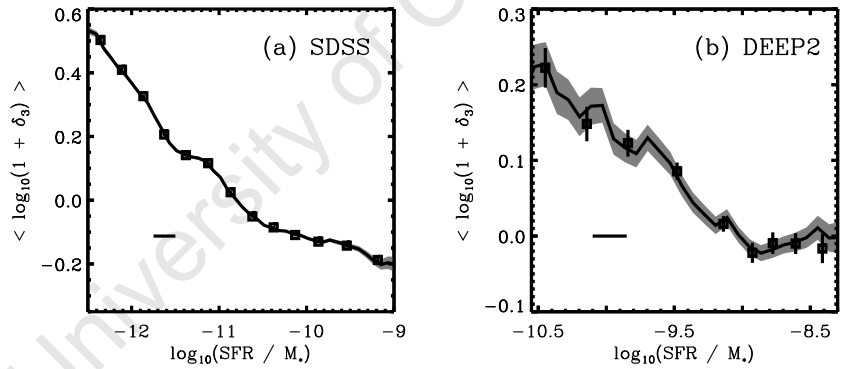

Figure 2.25: *Left*: The mean dependence of environment on sSFR and 1σ uncertainty in the mean (gray region) for SDSS galaxies. *Right*:The mean dependence of environment on sSFR and 1σ uncertainty in the mean (gray region) for DEEP2 galaxies. The sSFR in both low and high redshifts declines with environment(adopted from Cooper et al, 2008)

galaxies) (see Fig. 2.25) implying that a sSFR-density relationship is not responsible for the origin of a SFR-density relationship at higher redshift Universe. It is the stellar mass-density relationship that drives the observed trend.

In search of further similarity between local LIRGs and $z \sim 1$ blue galaxies, we traced the origins of the SFR-density trend of local LIRGs by disentangling their total SFR into sSFR and

stellar mass components. According to Figure 2.20, LIRGs' sSFR has weak or no correlation with local density (panel b) while their stellar mass correlates more strongly with their local density (panel d). This means the observed trend between total SFR and density is contributed by the mass-density relationship while sSSF has less effect. Note that this result seems in apparent contradiction with the result from Figure 2.17 in which stellar mass has no environmental dependence at a *fixed SFR*. However, these two results represent two different scenarios: the first one is a relationship between stellar mass and environment at constant SFR while the other one is a relationship between stellar mass and environment in general without being restricted to a certain value of SFR. The minimum stellar mass IR-galaxies have, as indicated by the black diagonal lines in both panels of Figure 2.17, is not only SFR dependent but also density dependent. At higher density environments, the minimum mass gets higher and the environment is dominated by higher stellar mass objects than the case at low density environment in which a wider range of stellar mass objects exist. Therefore if one averages the stellar mass at different density bins, a correlation between stellar mass and density is not a surprise. For $z \sim 1$ blue galaxies, the SFR-density trend also reflects their stellar mass-density relationship, where stellar mass increases with density (Cooper et al. 2008). Both in local LIRGs and $z \sim 1$ blue galaxies, the mass-density relationship appears to drive the observed total SFR-density relationship. This similarity gives us additional evidence that there is indeed some kind of similarity between these two populations of galaxies.

The positive correlation of SFR and environmental density of LIRGs raises a question regarding the mechanism of intense bursts of SF in the local Universe. Normally, as density increases, the possibility of finding processes such as ram-pressure stripping, galaxy harassment and galaxy strangulations that suppress SF activities is high. Despite this fact, we observe enhanced SF as density increases in local LIRGs. In addition to that, there is observational evidence that shows LIRGs living in environments such as outskirts of clusters that are not normal for the magnitude of SFR they exhibit (Laag 2006, Duc et al. 2004, Lemonon et al. 1998, Kleinmann et al. 1988).

Simulations suggests that major mergers or interactions happening near the tidal fields of cosmological structures such as groups and clusters are more efficient in producing the highest level of star-bursts than major mergers or interactions happening in the absence of any tidal effects from groups or clusters (Martig & Bournaud 2008). For example, two M33- like galaxies interacting in the tidal field of Local group-like or Virgo-like clusters could have their star-bursts raised by a factor of two or more. Given the environment where LIRGs, and especially ULIRGs, are found in our study, SF triggering mechanisms such as tidal field from massive cosmological structures could be considered to explain their SF mechanism. Such mechanism of SF must have been very much efficient in the high redshift Universe when clusters were still in the process of forming and galaxies at the centre of the forming clusters had not yet exhausted their gas. Consequently, at $z \sim 1$ SFR is correlated with environment unlike the case at $z \sim 0$. In the local Universe, SF activity has been quenched especially in cluster cores and this resulted in less SFR at the highest density regions, though the strength of the tidal field of the groups and cluster is

unchanging. However, in the outskirts of clusters and very rich group-like structures, there are still gas-rich interacting galaxies whose SF mechanism has not started in the past for various reasons. Such galaxies may have just fallen down to the group or cluster potential well recently affected by the action of the group or cluster tidal field.

2.6.7 The halo model and star formation of LIRGs

So far, this work studied the environment of IR galaxies at $2h^{-1}$Mpc. This scale is comparable with most host virialized dark matter halo sizes. The most important result of this work, which is the correlation of environment and SFR in LIRGs, implies that the L_{IR} activity (or SFR) of LIRGs is closely related with their large scale mass concentration. Since the scale of the environment probed is comparable with the size of virialized dark matter haloes, it would be natural to extend the relation found between L_{IR} and environment to L_{IR} and halo mass.

Thus, in order to get a complete understanding of the properties of LIRGs and their SF properties, it is crucial to understand their host dark matter haloes. The next Chapter investigates the dark matter halo size of LIRGs to further understand their SF properties in the context of halo model of galaxy formation and evolution (Kauffmann et al. 1993, Berlind & Weinberg 2002).

2.7 Conclusions and summary

In this chapter, we have studied the connection between SF and environment in local LIRGs and non-LIRG IR galaxies in comparison to other types of galaxies (SDSS) locally. The results are compared to other similar works done for high redshift galaxies in order to understand the nature, possible origin and evolution of local LIRGs. Both the LIRG and non-LIRG IR galaxies are drawn from IRAS catalogues. Densities are estimated in a cylinder of $2h^{-1}$Mpc radius and $10h^{-1}$Mpc length scale using various redshift surveys that are K-band (6dF and 2MRS) and infrared (PSCz-II) selected samples in order to ensure that the result is not biased by the nature of the density field. We have arrived at the following conclusions:

1. The IR luminosity value $L_{IR} \sim 10^{11}h^{-2}L_{\odot}$ is a special luminosity point among IR selected galaxies. It stands out as a demarcation point to mark a dramatic environmental difference. We show that there is a drastic density rise above $L_{IR} = 10^{11}h^{-2}L_{\odot}$ (LIRGs) while the IR galaxies below this luminosity point have a local density equal to the mean galaxy density of the density field galaxies. The local environments of both classes of galaxies are consistent both with their morphology and SF properties, since the non-LIRGs are typically expected to be fairly normal quiescent, even isolated, spirals, whereas LIRGs are known to often be involved in interactions, i.e. to be found in somewhat denser environment.

2. It is found that the L_{IR} values of local LIRGs are correlated with their density. This could be because galaxies at higher density environments experience a higher probability of interaction and mergers than those at relatively lower environment and hence have high rates of SFR (or L_{IR}).

3. Even if we could not cover the entire ULIRG luminosity range because of lack of data, we noticed that the L_{IR}-density trend found for LIRGs extends to the ULIRG regime up to $10^{12.5}h^{-2}L_{\odot}$ in the same manner. However, it is not possible to confirm if the trend would carry on across the ULIRG regime on account of lack of data.

4. We find that at constant stellar mass (derived from M_K), SFR (derived from L_{IR}) is correlated with background density for IR galaxies (most importantly for LIRGs). At constant L_{IR} value, no trend is observed between M_K and density. Density defines the SFR at all masses.

5. Galaxies also seem to require a certain minimum stellar mass in order to be LIRGs. Once the minimum stellar mass limit is met and they become LIRGs, any additional mass they have does not have an effect on their SFR. If they want to form stars at a higher level, their environment must be elevated. The minimum stellar mass limit is correlated with the L_{IR} values of the galaxies. This limit is found to be similar with the Kennicut-Schmidt law.

6. The overall local mass overdensity at a scale of $2h^{-1}$Mpc plays a crucial role in the SFR of local LIRGs but not only because it includes the 1 Mpc environment which is known to correlate strongly with SF properties of galaxies. However, it is not clear if the density field in the (1-2) Mpc scale has indeed a genuine effect or it is because this density is correlated with the 1 Mpc that we see the effect at the 2 Mpc scale.

7. The larger scale environment of LIRGs is correlated with their SF. It is not only the immediate surroundings (one-to-one interaction and mergers) of LIRGs, that makes them LIRGs. This explains why interacting LIRGs are not common in poor groups or fields even if two gas-rich galaxies happen to merge in such environments. In other words, the interaction should happen in the potential well of a bigger mass concentration than the potential of the two interacting galaxies. This result supports the halo model of galaxy formation (see next chapter).

   Despite being a far-infrared selected sample, PSCz galaxies as a density field produced similar results to both 6dF and 2MRS samples which are K-selected. Once the bigger scale overdensity is optimal enough to form one LIRG, then it is also optimal to convert another gas-rich galaxy into an IR galaxy. As a result, PSCz galaxies can be considered as tracers of the local mass concentrations better than their morphology or luminosity class

would lead to assume. This could possibly be part of the reason why PSCz-II sample as a density field produced similar result to the other samples (6dF and 2MRS).

8. The SFR of LIRGs is proportional to their environment. This relationship between SF and environment of LIRGs is similar to what is witnessed in blue cloud galaxies at $z \sim 1$. In both LIRGs and $z \sim 1$ blue cloud galaxies, the origin of the SFR-density relationship appears to come from the relationship stellar mass has with density. These similarities give some clue that the formation mechanism of local LIRGs and $z \sim 1$ blue galaxies might be similar. These two populations were formed of similar processes but at different times. Alternatively, local LIRGs might be survivors of whatever process transformed blue cloud galaxies of the past into the present red sequence galaxies.

9. Below $L_{IR} \leq 10^{11} h^{-2} L_{\odot}$, non-LIRG IR galaxies do not only live in less dense environment than LIRGs but they experience a flat L_{IR}-density trend in $2h^{-1}$Mpc scale. Once the LIRG luminosity limit is passed in the lower direction, the $2h^{-1}$Mpc scale potential well has no effect in the SFR of IR galaxies in that regime.

3

Dark matter haloes and LIRGs

3.1 Background and objective

In the context of the hierarchical model of structure formation, ΛCDM theory, dark matter haloes are hierarchically and gradually merging in time to form more complex systems like groups, clusters and walls. Galaxies, according to this theory, are formed from baryonic matter inside these dark matter haloes and interact with their environment (environment in this context is represented both by baryonic and non-baryonic matter) (White & Rees 1978). This interaction with their environment is believed to play a crucial role in shaping their evolution.

More massive haloes host a larger number of galaxies than smaller haloes. This means the mass of dark matter halo is correlated to the number of galaxies (the environment inside the halo) it contains. As a result, a galaxy living in a high mass halo is living in a denser environment than a galaxy living in a smaller size halo. This in turn means that measuring a galaxy density around galaxies is the same as measuring the underlying dark matter halo mass distribution (Berlind et al. 2005).

Through the dependence of SFR of galaxies with environment, one can then say that halo mass is the primary halo property correlated with the SFR of galaxies. For example, SF activity is more efficient in group size haloes than in cluster size haloes. Therefore, understanding the dark matter halo mass of galaxies gives insight into understanding their SF processes.

In Chapter 2, it is shown that local LIRGs live in an overdense environment and also that their SFR is correlated with their environment on a 2 Mpc rscale. The fact that their environment within a 2 Mpc radius has an effect on their SFR is already an indication that their SF is not

only a matter of a one-to-one interaction but that it is also a matter of the larger scale mass distribution that can possibly be characterised by the size of the dark matter halo they live in.

This chapter, motivated by the above mentioned two reasons, addresses the same problem that is addressed in the previous Chapter 2, which is the relationship of SFR and environment of LIRGs, from a more theoretical perspective. We will explain whether the strong SF exhibited by LIRGs is consistent with the environment defined by the size of dark matter halo of galaxy groups according to ΛCDM theory. We also make comparisons with other results we found in Chapter 2. Hereafter, the terms "galaxy group" and "galaxy systems" are used interchangeably to refer to a collection of galaxies with two or more members living in the same dark matter halo bound by mutual gravitational attraction.

3.2 Data

This work made use of six volume-limited samples extracted from two redshift surveys: the Point Source Catalogue Redshift survey (PSCz) and the 2MASS redshift survey (2MRS). Since the main objective of the work is understanding the environments of IR galaxies (especially LIRGs) in terms of the size of the dark matter halo of the galaxy group they are associated with, the first sample (PSCz), being IR selected, is used as a target sample (we refer to this same as a target sample).

K-selected galaxies cluster more than optically selected galaxies (Ma et al. 2009). Knowing that the clustering nature of galaxies is associated with the mass concentration in their surrounding environment, K-selected galaxies are always preferred to optical or any other wavelength selected samples as a mass tracer of the local environment of galaxies. As a result, the second sample (2MRS), being K-selected, was used to identify groups based on the mass of their dark matter halo (we refer to this sample as a group sample). For a detailed description of the samples used in this Chapter and the corresponding references, please see Chapter 2.

3.2.1 Volume-limited samples

Why volume-limited samples?

As it is explained above, the main purpose of the work in this chapter is to determine the likelihood of finding LIRGs in different density environments. Given this objective, three important issues are considered when defining our samples.

1. Different environments (field, group, and cluster) are defined based on their halo mass size. Their halo mass is determined using the cumulative luminosity of member galaxies in identified groups (see Section 3.3.5 for a detailed explanation of how halo masses are determined). Therefore, unlike the work in Chapter 2, flux bias in the samples from which groups are identified is an important concern as it can easily lead to incorrect mass

determination. Even if we are covering a small redshift range (the maximum being z=0.05), groups identified at higher redshift tend to miss galaxies below the minimum flux limit at a certain redshift and that makes groups appear lighter in their halo mass than they are in reality in comparison to groups identified at lower redshift.

2. Since we want to study the likelihood of finding galaxies in a certain environment, the target galaxy samples should also be complete. Otherwise, it is impossible to do any probabilistic analysis of the sample.

3. Finally, it is known that the target galaxies and the group samples should have the same spatial distribution or should be in the same volume to make a cross match between them.

In order to accommodate the above three requirements, we used volume-limited samples. However, this does not necessarily mean that there is no redshift dependent flux bias even above the minimum flux limit in volume-limited samples. Since we are covering a small range of redshift in all the volume-limited samples, we are assuming that this bias can simply be ignored.

Further details on how we defined the individual volume-limited samples are discussed below.

2MRS volume-limited samples

As a first attempt to construct a volume-limited sample out of the 2MRS survey, a rough estimate of redshift cut for the samples was done based on two requirements. Firstly, the volume enclosed by the redshift limit of the volume-limited sample must have maximum number of 2MRS galaxies and secondly, when the same redshift limit is applied to the target sample, PSCz, the resulting volume-limited PSCz sample has a statistically good number of LIRGs.

Once we got a rough idea of the redshift limit that satisfies the above requirements, this limit was further fine-tuned to find the sweet spot that could result in the maximum number of galaxies in both samples. Finally, we came up with three 2MRS volume-limited samples with $z \leq 0.02$ and $M_K \leq -23.4$, $z \leq 0.024$ and $M_K \leq -23.8$ and finally $z \leq 0.03$ and $M_K \leq -24.3$. Hereafter, we refer to these samples as V2M1, V2M2 and V2M3 respectively. These samples have 5044, 5457 and 4954 galaxies respectively.

PSCz volume-limited samples

For each of the three 2MRS volume-limited samples, we constructed a target galaxy volume-limited sample from the PSCz. The choice of the maximum redshift for each of these volume-limited samples was made based on the maximum redshift of each of the corresponding 2MRS volume limited samples. The choice of the minimum L_{IR} limit for the PSCz volume-limited sample was made in such a way that the PSCz magnitude and the 2MRS magnitude limits are the same or at least close to each other. In order to do this, a rough conversion of $M_K = -23.4$ into L_{IR} was made based on the relationship of M_K and L_{IR} drawn from PSCz galaxies with

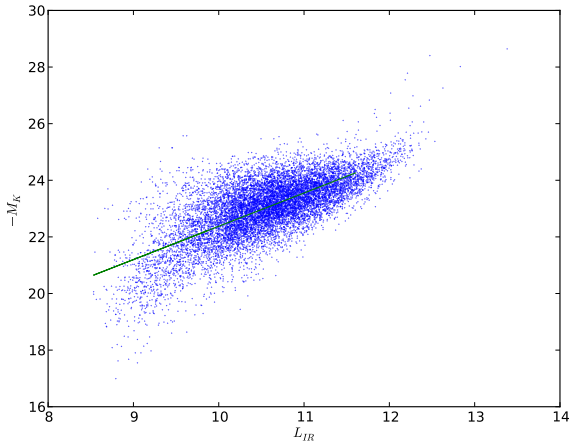

Figure 3.1: The relation between M_K and L_{IR} values of PSCz galaxies. The line represents the best fit. The M_K values are taken from the 2MASS.

M_K determined by matching PSCz with 2MASS (see Fig. 3.1). The equation of the best fit to the data is $L_{IR} = 1.176M_K + 10.6$. Based on this equation, the L_{IR} value corresponding to $M_K = -23.4$ was found to be 10.8 and this was then taken as a luminosity limit for all the three PSCz volume-limited samples. Here it is important to note that the scatter in the relationship between L_{IR} and M_K is not negligible and obviously resulted from the presence of different populations of galaxies. Thus, the conversion may have significant uncertainty especially on an individual galaxy basis.

The three volume-limited samples are characterised by the following redshift and L_{IR} limits: $z \leq 0.02$ and $L_{IR} \geq 10.8$, $z \leq 0.024$ and $L_{IR} \geq 10.8$ and finally $z \leq 0.03$ and $L_{IR} \geq 10.8$. Hereafter, we refer to them as VP1, VP2 and VP3 respectively. We took the advantage of the fact that the L_{IR} luminosity limit is below $10^{11}L_{\odot}$ so that we can do the same analysis for galaxies below $10^{11}L_{\odot}$ (Non-LIRG IR-galaxies) and compare the result with the LIRGs.

Name	Magnitude limit	z_{max}	No. of galaxies	volume $[Mpc^3]$
V2M1	$M_K \leq -23.4$	0.02	5044	7.377×10^5
V2M2	$M_K \leq -23.8$	0.024	5457	1.272×10^6
V2M3	$M_K \leq -24.3$	0.03	4954	2.475×10^6

Table 3.1: 2MRS volume-limited samples.

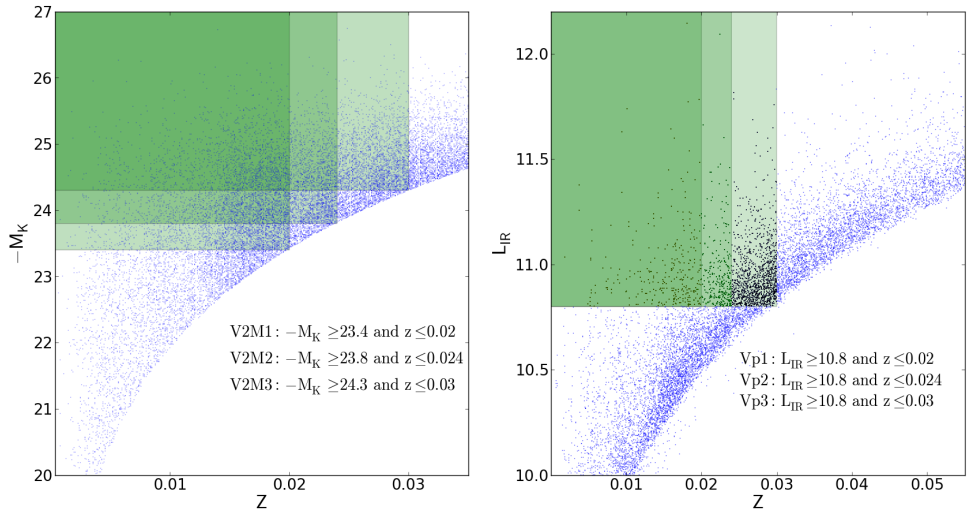

Figure 3.2: *Left*: A volume-limited samples extracted from 2MRS. *Right*: The volume-limited samples extracted from PSCz.

Name	Magnitude limit	z_{max}	No. of galaxies
Vp1	$L_{IR} \geq 10.8$	0.02	290
Vp2	$L_{IR} \geq 10.8$	0.024	565
Vp3	$L_{IR} \geq 10.8$	0.03	1616

Table 3.2: PSCz volume-limited samples.

3.3 Group finding

The task of defining galaxy groups is very subjective and often misleading. A system assumed to be a group in the nearby Universe might be identified as a field (isolated) galaxy in the distance Universe because of the dimming of the flux of individual galaxy members. Some define galaxy groups in terms of the number of members while others define them based on dynamical mass of the system. Here in this work we define galaxy groups as collections of galaxies dynamically (gravitationally) bound to each other (Geller & Huchra 1983) and occupying the same dark matter halo (Berlind et al. 2006). We aim to identify galaxy groups based on this context.

3.3.1 Friends-of-friends (FoF) group finding algorithm

The friends-of-friends (FoF) group finding algorithm originally used by Huchra & Geller (1982) and Geller & Huchra (1983) to identify galaxy groups is employed in this work. The basic

principle of this algorithm has been used in identifying dark matter haloes in simulations (Jenkins et al. 2001) as well as identifying galaxy groups in redshift surveys (Huchra & Geller 1982, Eke et al. 2004, Berlind et al. 2006) and it is proved robust.

The algorithm basically finds all "friends" of a galaxy linked to it by a certain linking length and again finds friends of each of the already identified friends in the first attempt. This goes on recursively until it finds no more friends. If there is no friend for a galaxy at the first iteration, then the galaxy is assumed to be isolated. Figure 4.3 is a flow chart describing the way how the algorithm works.

This algorithm has important properties that make it preferable to other ways of identifying groups. These include:

1. Apart from the spatial coordinates on the sky and the redshift information; it uses no other properties of galaxies to identify groups. This is a very interesting feature of the algorithm which makes it stand strong against any bias caused by different properties of galaxies. For example, there is no bias by magnitude, colour or size of galaxies as long as they are detectable. While this helps in the study of the spatial distribution of galaxies regardless of their specific type, the method is not flexible in accommodating requirements to study a specific class of galaxies such as only star forming galaxies unless they are preselected already.

2. The method identifies groups regardless of their geometry. This specific property makes the algorithm flexible enough to accommodate any dynamical interactions that could disrupt the otherwise spherical symmetry of virialized galaxy systems.

3. For a given catalogue and linking length, the algorithm produces a unique group catalogue. There is no possibility that a galaxy belongs to more than one identified group.

This work follows the approach and the notations used in Berlind et al. (2006) to discuss how the method is applied in our specific case. Two galaxies i and j are friends if both the line-of-sight $D_{\parallel,ij}$, and transverse $D_{\perp,ij}$ distances between these two galaxies are less than a certain line-of-sight and the projected linking lengths respectively. Throughout the entire calculations, non-relativistic luminosity distances are used because the redshift range we work in ($z \leq 0.06$) is small.

If two galaxies, i and j, are separated by an angle θ_{ij} and have redshifts z_i and z_j; $D_{\perp,ij}$ and $D_{\parallel,ij}$, both in units of (h^{-1} Mpc), are given by

$$D_{\perp,ij} = (c/H_o)(z_i + z_j)sin(\theta_{ij}/2), \tag{3.1}$$

$$D_{\parallel,ij} = (c/H_o)|z_i - z_j|, \tag{3.2}$$

then the two galaxies are friends if

$$D_{\perp,ij} \leq b_\perp \bar{n}_g^{-1/3}, \tag{3.3}$$

and

$$D_{\parallel,ij} \leq b_{\parallel} \bar{n}_g^{-1/3}, \tag{3.4}$$

where $b_{\parallel}$ and $b_{\perp}$ are the line-of-sight and transverse linking lengths respectively (see Section 3.3.2) in units of the mean intergalaxy length and $\bar{n}_g$ is the mean density of galaxies in the sample measured in units of Mpc^{-3}. Even if the algorithm does not prefer any geometry, because of the peculiar motion of galaxies along the line-of-sight direction, it appears that cylindrical geometry with length equal to twice the line-of-sight linking length and radius equal to the projected linking length is a preferred geometry for the algorithm.

3.3.2 The choices of linking lengths

Both the line-of-sight ($b_{\parallel}$) and the projected ($b_{\perp}$) linking lengths used in this work were directly adopted from Berlind et al. (2006). In order to optimise the choice of $b_{\parallel}$ and $b_{\perp}$ for any kind of redshift survey, Berlind et al. (2006) used a mock galaxy catalogue for which they know exactly which mock galaxies live in the same dark matter halo. Using FoF algorithm on the mock catalogue, they recovered galaxy groups for different values of linking lengths (both $b_{\parallel}$ and $b_{\perp}$) and compared how well each linking length recovered the original true mock galaxy groups. The comparison made between the true mock galaxy groups (associated halo) and the recovered ones were based on how well the following four important features of the recovered group were met:

1. The group multiplicity function (the abundance of groups as a function of the number of galaxies they enclose) compared to the "true" halo multiplicity function,

2. The number of galaxies in a halo (N_{true}) and the number of galaxies in the group found in the halo by FoF ($N_{observed}$),

3. The distribution of the projected group sizes as a function of group richness compared to the "true" distribution of projected halo sizes as a function of halo multiplicity,

4. The distribution of group velocity dispersions as a function of group richness compared to the "true" distribution of halo velocity dispersions as a function of halo multiplicity.

However, Berlind et al. (2006) had difficulty to find a linking length (both $b_{\parallel}$ and $b_{\perp}$) that satisfied all the four requirements at the same time and hence they sacrificed the fourth requirement as it affected the linking length least. The optimised linking length found is:

$$b_{\parallel} = 0.75, \tag{3.5}$$

and

$$b_{\perp} = 0.14. \tag{3.6}$$

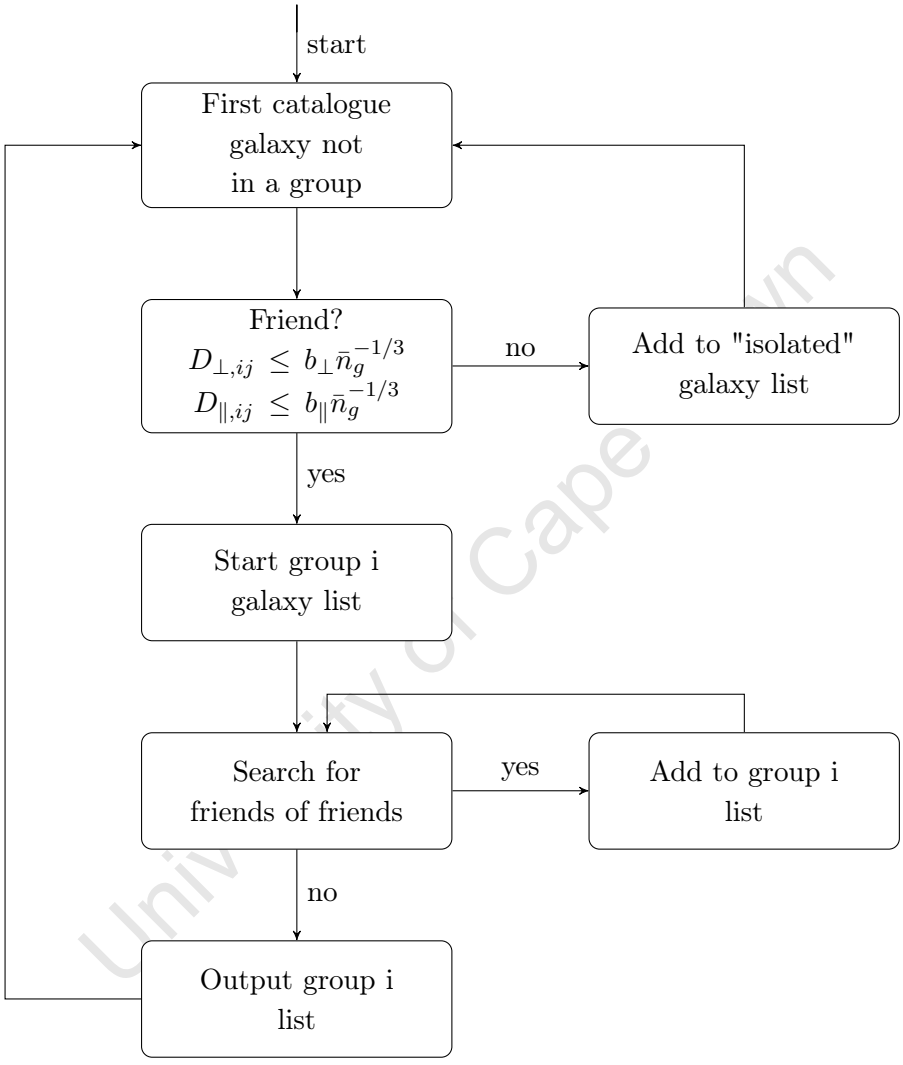

Figure 3.3: Flow chart for the way Friends-of-Friends (FoF) algorithm works to find groups.

3.3.3 Identified groups from 2MRS volume-limited samples

The FoF group finding algorithm described above was run on all the three 2MRS volume-limited samples (V2M1, V2M2 and V2M3) to identify groups, clusters and fields (isolated) galaxies. In V2M1, out of 3087 systems identified, the number of isolated galaxies, groups with 2 members and groups with more than 2 members are 2291, 441 and 355 respectively. These numbers for V2M2 out of 3459 identified systems are 2592, 491 and 376. Finally V2M3 out of 3395 systems has 2639 isolated, 453 groups with 2 members and 303 groups with more than 2 members. Figure 3.4 shows the overall distribution of the number of galaxies in the identified groups.

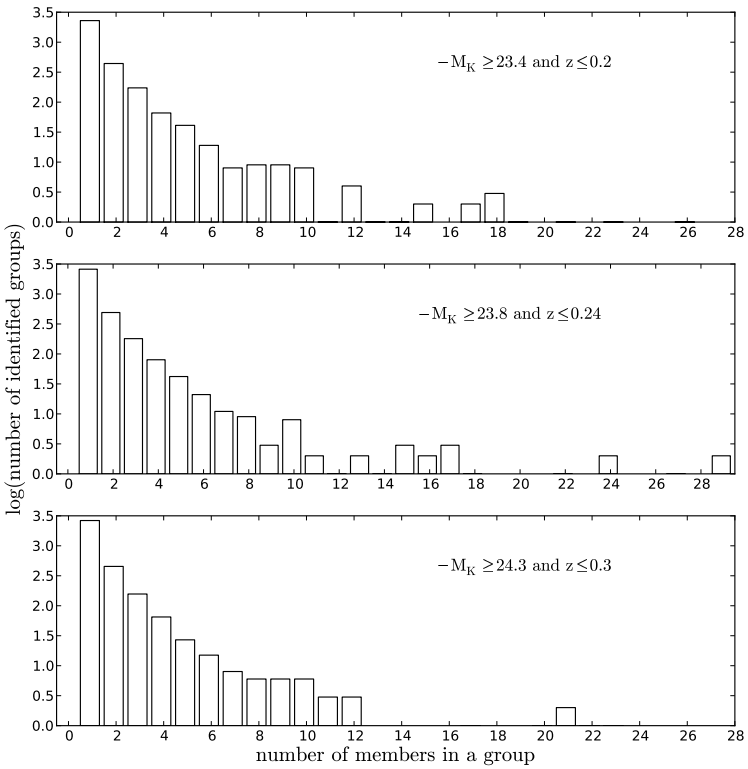

Figure 3.4: The distribution of the number of galaxies per identified groups. The number of rich groups (clusters) is much smaller than fields and groups.

3.3.4 Estimation of group K-band magnitude

K-band magnitude for each of the identified galaxy groups in each of the three 2MRS volume-limited samples is computed by summing up the individual K-band absolute magnitude of members as

$$M_{K_{total}} = -2.5log(\sum_{i} 10^{-0.4M_{Ki}}). \tag{3.7}$$

However, this does not mean that the estimated magnitude is the total magnitude of the groups because the volume-limited samples are complete only to a certain M_K magnitude limit (2MV1: -23.4, 2MV2: -23.8 and 2MV3: -24.3). The total magnitude of the individual systems, therefore, only tells us where each particular group sits if all the systems within each volume-limited sample are listed in absolute magnitude order.

3.3.5 Estimation of halo mass

It is possible to estimate the halo mass (dynamical mass) for galaxy systems using various methods that rely on the observables of galaxy systems. Most of the methods are, however, only effective when they are applied to high mass galaxy systems such as clusters (Voit 2005). The methods include the mass-X-ray luminosity relationship (Reiprich & Böhringer 2002), mass-weak lensing relationship (Metzler et al. 1999), and mass-velocity dispersion relationship based on the virial theorem (Evrard 2004). The X-ray luminosity relationship has a scatter as high as 50% and the weak lensing method is usually affected by lensing coming from mass outside the virial radius. The mass-velocity dispersion method gives good and reliable results as long as the galaxy systems have a sufficient number of members to allow a reliable measurement for their velocity dispersion. This method of mass estimation is more reliable in clusters because of the high number of member galaxies. Evrard (2004) derived a relation between the virial mass enclosed by a radius at which density is 200 times the mean density and the velocity dispersion (σ_v) as:

$$M_{200} \simeq \frac{10^{15}h^{-1}M_{\odot}}{H/H_o}(\frac{\sigma_v}{1080kms^{-1}})^3, \tag{3.8}$$

where M_{200} is the mass included inside the radius at which the density is 200 times the mean density of the Universe. As one can easily notice from the relationship above, this method is dependent on the accurate determination of the velocity dispersion. Normally, estimating the dynamical masses of our identified galaxy systems using this method would have given us a reliable result. However, since the fraction of systems with a pair of galaxies are greater than the fraction of systems with more than two galaxies, the mass estimate is highly subject to statistical risk. As a result we are forced to estimate the masses using another technique.

We made a rough estimate of the halo mass by matching the number density of groups from their cumulative luminosity function to the number density of the theoretical halo mass function. Here the underlying assumption is that since groups of galaxies live in haloes and the halo mass is proportional to the luminosity of groups, there is a one-to-one correlation between the number density of groups of a certain luminosity and the number density of haloes of a certain mass.

There are two possible sources of uncertainty that we expect in the mass estimate: scatter from the halo mass function determination itself and scatter from the matching of the group luminosity function and the halo mass function. In the latter case, it is known that the one-to-one correlation between the halo number density and the group number density is not entirely true. In reality, it is true that different luminosity groups might occupy the same size dark matter halo and result in scatter at a given halo mass. However, our assumption is not that bad for the nature of work we are using the estimated halo mass. This method is in fact tested and has produced good results (Berlind 2006, Quintero et al. 2005).

A luminosity function is computed for each of the volume-limited 2MRS samples by counting groups below a certain M_K value and dividing this count by the corresponding volume (see Table 3.1) of each of the samples. Figure 3.5 shows the luminosity functions of each of the samples. The differences in the luminosity functions arise from the fact that each of the different volume-limited samples have a different magnitude limit. The magnitude limit puts a constraint on the calculation of the total M_K magnitude of groups though it does not change the order of their magnitude. For example, when the magnitude limit goes deeper in the volume-limited sample, the luminosity function is systematically pushed to the right in Figure 3.5 while preserving the luminosity order and the abundance.

A theoretical halo mass function computed based on a simulation work by Warren et al. (2006) is adopted to find the theoretical number density of halo masses. While calculating their halo mass function, the authors used concordance ΛCDM cosmology with $(\Omega_M; \Omega_b; n; h; \sigma_8) = (0.3; 0.04; 1; 0.7; 0.9)$. Based on their mass function, we have come up with a cumulative mass function by summing up contributions above a certain mass limit. Figure 3.6 shows the theoretical cumulative mass function of haloes.

After finding the cumulative halo mass function and group luminosity functions, we matched their number count and got the following results. In terms of halo mass, the fraction of groups with $M_{halo} < 10^{12.5} M_\odot$, $10^{12.5} M_\odot \leq M_{halo} < 10^{14} M_\odot$ and $M_{halo} \geq 10^{14} M_\odot$ for V2M1, V2M1 and V2M3 respectively are 71.5%, 28.1% and 0.5%; 56.1%, 43.1% and 0.7%; and 12.9%, 85.6% and 1.6% (see table 3.3). Figure 3.7 shows the distribution of the halo mass in each of the three samples. Because of the difference in magnitude limit, it is seen that the minimum halo mass is different for the three samples. In the case of V2M1, it is possible to go past $log(M/M_\odot) = 12$ limit whereas the other samples have a higher limit because of their higher magnitude limit.

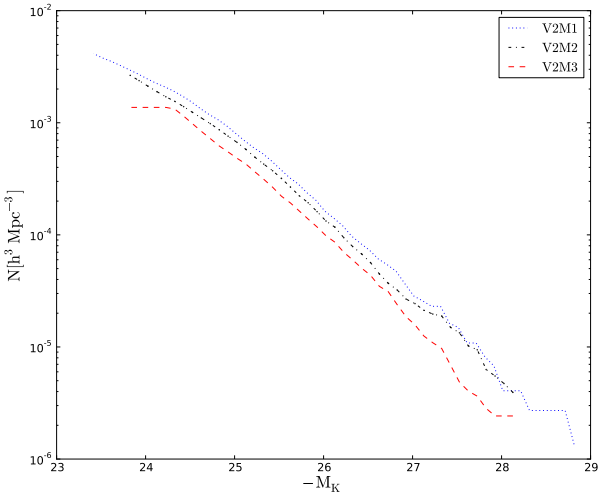

Figure 3.5: Group luminosity function for the three volume-limited samples.

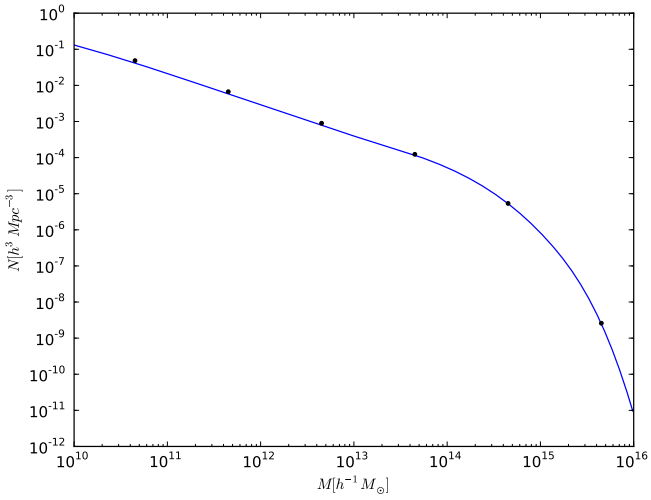

Figure 3.6: A cumulative halo mass function (adopted from Warren et al. (2006)).

3.3.6 Coordinates and redshift

The right ascension and declination of the centroid of the group is taken as a right ascension and declination of the group. The mean $\langle cz \rangle_g$ value for the group is calculated from the individual members as:

Sample	$< 10^{12.5} M_{\odot}$	$10^{12.5} M_{\odot} \leq M_{halo} < 10^{14} M_{\odot}$	$\geq 10^{14} M_{\odot}$
V2M1	2206 (71.5%)	865 (28.1%)	16 (0.5%)
V2M2	1940 (56.1%)	1492 (43.1%)	24 (0.7%)
V2M3	437 (12.9%)	2905 (85.6%)	48 (1.6%)

Table 3.3: The distribution of 2MRS galaxies into different size halo groups.

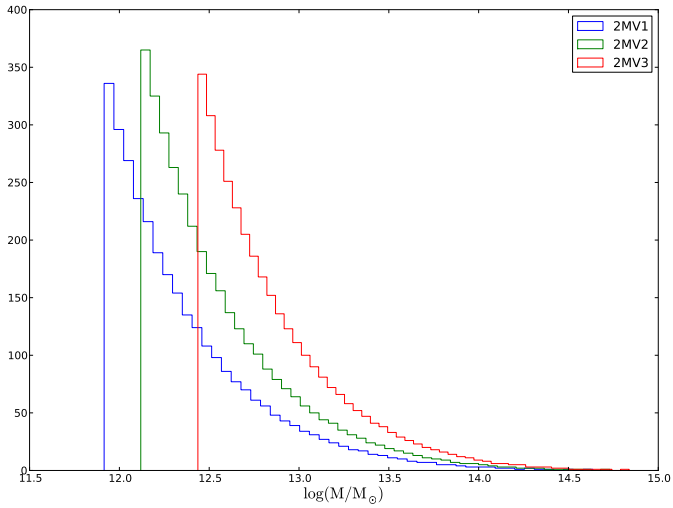

Figure 3.7: The halo mass distribution of the three 2MRS volume-limited samples.

$$\langle cz \rangle_g = \frac{1}{N} \sum_i cz_i, \tag{3.9}$$

where N is the total number of galaxies in the group and cz_i is the cz value for the i^{th} galaxy. When a galaxy is isolated, its own right ascension, declination and redshifts are preserved.

3.3.7 Virial radius

The physical extent of haloes is defined as the physical size in which the matter inside it is gravitationally bound and stable in a well-defined orbit (see Section 1.4 in Chapter 1). This represents what is called a virialized dark matter system and the physical size of such virialized systems is referred to as the virial radius. We have used Equation 1.4 from Chapter 1 given below again to calculate the virial radius:

$$R_{vir} = (\frac{3}{4\pi}\frac{M_{vir}}{200\bar{\rho}})^{1/3}, \tag{3.10}$$

where R_{vir} is the virial radius and M_{vir} is the group mass.

3.3.8 Velocity dispersion

Characteristic velocity dispersion for each group is also derived. This velocity dispersion is calculated to be the maximum rotational velocity of the dark matter halo with density profile which represented by Navarro-Frenk-White profile (NFW) (Navarro et al. 1997). This density profile is given as

$$\rho(r) = \frac{\rho_0}{\frac{r}{R_s}\left(1 + \frac{r}{R_s}\right)^2}, \tag{3.11}$$

where R_s represents the radius, ρ_o is the mean density of the Universe and r is the radius. The velocity dispersion is calculated by combining Equation 3.19 with

$$M(r) = \int_0^r 4\pi\rho(r), \tag{3.12}$$

and combining this with Newton's law which is given as

$$V^2 = \frac{Gm(r)}{r}, \tag{3.13}$$

where V is rotational velocity, G gravitational constant and m is mass inside the radius r.

One can come up with a velocity profile as a function of r by solving Equation 3.13. The velocity profile depends on r and has a maximum value at a certain characteristic radius. Solving numerically, we took the maximum velocity (V_{max}) as the velocity dispersion of the groups. This maximum velocity is assumed to be the maximum velocity galaxies can have inside their respective haloes.

In summary, all the identified groups have now right ascension, declination, velocity (or redshift), M_K, halo mass, R_{vir} and velocity dispersion. Based on R_{vir} and V_{max}, we formulated the physical dimensions of identified groups. Since groups of galaxies appear stretched in the line-of-sight direction because of the line-of-sight motion (peculiar velocity) of member galaxies, we assumed the groups to have cylindrical geometry with radius equal to the virial radius, R_{vir} and length twice the maximum rotational velocity of the halo, $2V_{max}$.

3.3.9 Cross-correlating galaxies with the cluster and group catalogue

Once groups are identified and the different physical parameters are derived for them, the next step involves trying to correlate the target galaxies (PSCz) to the identified groups. A line-of-sight and transverse distance between a galaxy and each of the groups is calculated. Finally, it is assumed that a galaxy belongs to a group if both the line-of-sight and transverse direction separation are less than a certain characteristic length.

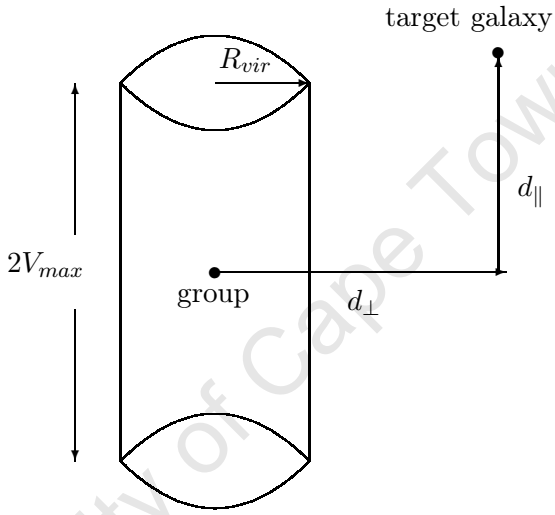

Illustration: The physical dimensions of groups is represented by their virial radius, R_{vir} and the maximum rotational velocity of galaxies $2V_{max}$. A galaxy belongs to a group if it lies in the boundary defined by R_{vir} and $2V_{max}$.

Suppose the galaxy in question have $d_{\parallel}$ and $d_{\perp}$ as the line-of-sight and perpendicular distances from the geometric centre of a particular galaxy system (could be isolated, group or cluster), then $d_{\parallel}$ is given by

$$d_{\parallel} = |(1/H_o)(cz_i - \langle cv \rangle_g)|. \tag{3.14}$$

For a small angle θ between the line of sight of the system and a galaxy in question, $d_{\perp}$, can be approximated to a good accuracy as

$$d_{\perp} \approx (1/H_o)\langle cv \rangle_g \theta. \tag{3.15}$$

Both distances are given in units of h^{-1} Mpc. A galaxy is considered to be part of, or gravitationally bound to, a certain group if it lies inside the cylinder defined by R_{vir} and $2V_{max}$, i.e. if

$$d_{\parallel} \leq V_{max}/H_o. \tag{3.16}$$

$$d_{\perp} \leq R_{vir}. \tag{3.17}$$

In cases where a galaxy might lie in a cylinder of more than one group, then the line-of-sight and projected distances from each group to the galaxy are weighted by R_{vir} and $(1/H_o)V_{max}$ respectively. This is shown as

$$d = \sqrt{(d_{\parallel}/(1/H_o)V_{max})^2 + (d_{\perp}/R_{vir})^2}\,, \tag{3.18}$$

and the galaxy finally belongs to the group with the least value of d.

3.4 Results

Following the method described above in Section 3.3.9, we correlate galaxies both from 2MRS and PSCz volume-limited samples with groups identified from 2MRS in their corresponding volume coverage (see Section 3.3.3). Below we present the results for both 2MRS and PSCz samples.

3.4.1 Correlating individual 2MRS galaxies with identified 2MRS groups

Individual 2MRS galaxies from all the three volume-limited samples were cross correlated to the groups identified in the respective volume-limited samples following the discussion in Section 3.3.9. We presented in Table 3.4 the number and percentage of galaxies associated with a group with three or more members, with two members and with zero members (isolated).

The number of isolated galaxies in all the three 2MRS volume limited samples in Table 3.4 are higher than the number of isolated galaxies ($< 10^{12.5} M_{\odot}$) in Table 3.3. This difference arises because the cylindrical volume used here in this section is larger than the effective volume chosen by FoF algorithm.

The reason why we are using the cylindrical volume to assign 2MRS galaxies to groups when FoF already gave us a set of assignments is because we need to use the cylinder to match PSCz galaxies to groups and then we need to use the same method with 2MRS in order to correctly compare the two.

3.4.2 Correlating individual PSCz galaxies with identified 2MRS groups

PSCz galaxies from each of the volume-limited samples are also correlated with groups identified from the respective 2MRS volume-limited sample in the same manner explained in Section 3.3.9 and the result is presented in Table 3.5. In addition, we have also presented the result found only

Sample	≥ 3	2	isolated
V2M1	1871 (37.1%)	882 (17.4%)	2291 (45.4%)
V2M2	1883 (34.5%)	982 (17.9%)	2592 (47.49%)
V2M3	1409 (28.0%)	906 (18.8%)	2639 (53.2%)

Table 3.4: The distribution of 2MRS galaxies into different number size groups.

for LIRGs and non-LIRG galaxies in each sample. One general trend noticed is that as we go deeper into the maximum redshift of each of the volume-limited samples (from 0.02 (V2M1) to 0.024 (V2M1) and then to 0.03 (V2M1)), we note that the fraction of isolated galaxies (galaxies in field) increases from about 10% (minimum) to about 60% (maximum).

Sample	magnitude limit	no companion	at least one companion
V2M1	LIRGs	11 (11.2%)	87 (88.8%)
	non-LIRG	29 (15.1%)	163 (85%)
V2M2	LIRGs	22 (13.8%)	137 (86.2%)
	non-LIRG	121 (29.8%)	285 (70.2%)
V2M3	LIRGs	190 (44.7%)	235 (55.2%)
	non-LIRG	717 (60%)	474 (39.7%)

Table 3.5: The breakdown of the size of groups for LIRGs and non-LIRG IR galaxies.

In Figure 3.8, the distribution of the groups to which both the LIRG and the non-LIRG IR galaxies belong to is presented in a histogram form. The different histograms represent the different volume-limited samples and they do not include isolated PSCz galaxies. The result shows that most PSCz galaxies prefer to live in groups with fewer members than groups with more members. However, it is not yet clear whether this is indeed a true reflection or selection effect.

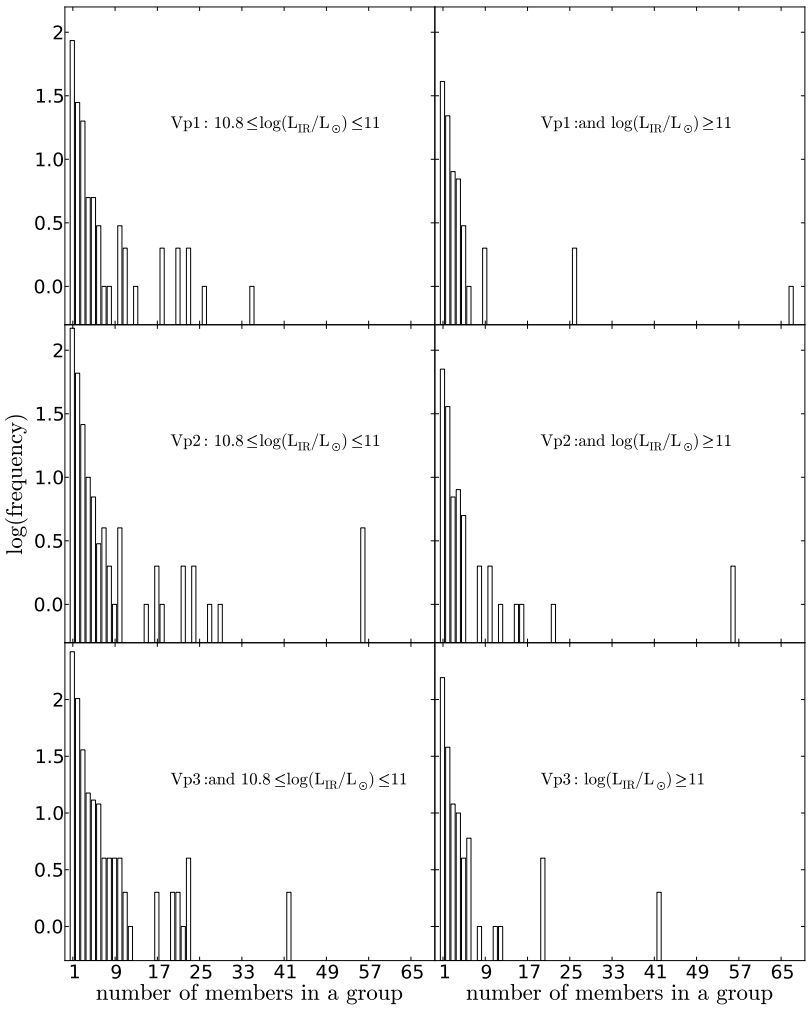

Figure 3.8: The distribution of the groups PSCz galaxies belong to. The left panels are for non-LIRGs and the right ones for LIRGs. The horizontal axis represents the number of members in each group.

3.4.3 The halo size distribution of the total IR samples

Once cross matching was done to both the 2MRS and PSCz samples with the groups identified, a probability distribution of the different mass haloes the PSCz and 2MRS galaxies live in is

determined. The probability distribution is made only for galaxies with at least one companion. This is done in order to show the halo mass distribution of PSCz galaxies with respect to 2MRS galaxies.

In each of the PSCz volume-limited samples, all of the galaxies that are not in a field are binned in a halo mass range of 0.4 dex and the number in each bin is divided by the total number of galaxies from their respective volume-limited sample. This is done to determine the probability of finding PSCz galaxies in a certain halo mass range. In the same way, in each of the 2MRS volume-limited samples, 2MRS galaxies are binned in the same size halo mass bin and each bin is divided by the total number of 2MRS galaxies in their respective volume-limited sample to get the probability of finding 2MRS galaxies in a certain mass range. The result is presented in Figure 3.9. The different panels represent the results for the different volume-limited samples. The squares represent 2MRS galaxies whereas the triangles represent the PSCz and all the error bars are calculated from Poisson statistics. The errors both for 2MRS and PSCz galaxies are sometimes too small to be seen.

The halo mass probability distribution both for the PSCz and 2MRS galaxies in all the three volume-limited samples shows that the probability of finding these galaxies declines with halo mass (see the square and the triangle points). However, this does not necessarily reflect the type of environment that these galaxies prefer to live in. It is, for example, known that 2MASS galaxies, a mixture of all sorts of galaxies, are not expected to have a certain preferred environment. The result, nevertheless, demonstrates that there is a higher probability of finding 2MASS galaxies in low density environments (poor groups and fields) than rich clusters and groups.

What the result reflects is the overall deficiency of high mass system in the Universe. The mass function of haloes shows that (Warren et al. 2006) low mass systems are more numerous than high mass systems in the Universe. According to Figure 3.6, the number density of haloes at a certain mass range declines with their mass and the declining rate is even higher once $M_{halo} = 10^{14} M_{\odot}$ is exceeded. Based on this fact, it is not surprising to see a declining probability distribution for LIRGs and 2MRS galaxies found in Figure 3.9.

In order to recover the true trend by avoiding the mass function bias, the ratio of the probability distribution of PSCz and 2MRS galaxies in the same mass bin is taken. The circles in the Figure 3.9 represent the relative probability of finding PSCz galaxies in a certain mass range with respect to 2MRS galaxies. The results in all the three panels show that the relative probability of finding PSCz galaxies in cluster environment is low but in field environment is almost as equal as the case for 2MRS galaxies. On the other hand, their relative probability distributions peaks in the halo mass range of $10^{12.5} L_{\odot} - 10^{13.5} L_{\odot}$, which is a group size halo regime. The probability of finding them in haloes of mass $\sim 10^{12.5} L_{\odot}$ is almost 1.3 times higher than finding 2MRS galaxies at the same halo size.

As it is mentioned earlier in this section, all the probability distributions of the PSCz galaxies

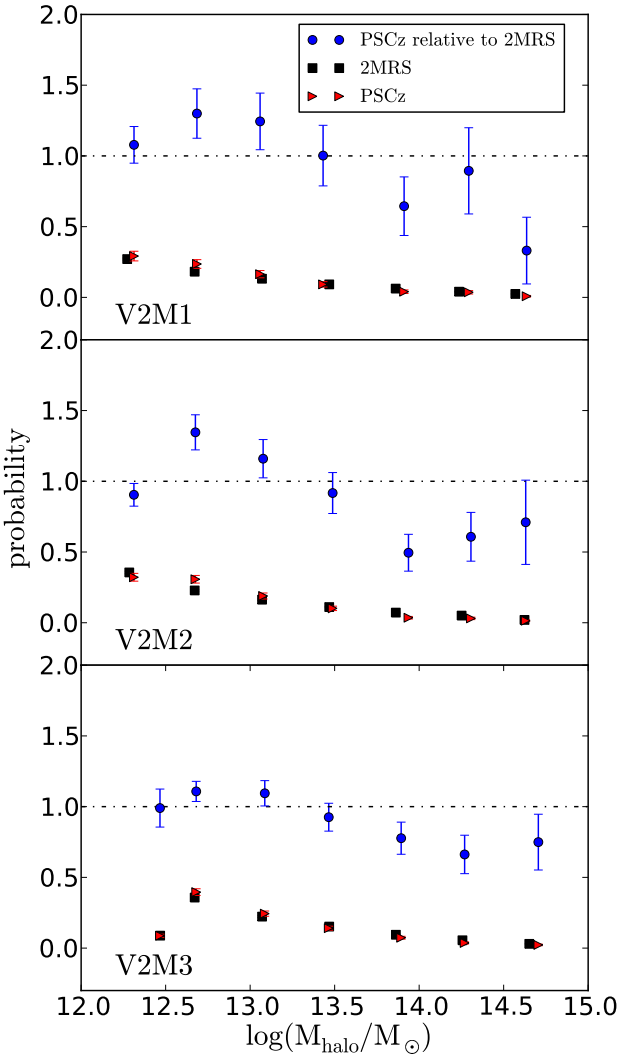

Figure 3.9: The probability of finding PSCz and 2MASS galaxies in a certain dark matter halo mass range. The red points represent the relative probability for finding PSCz galaxies, the black 2MASS, and the blue LIRGs relative to 2MASS galaxies.

are done only for galaxies that have at least one companion. In order to make the result complete, it would also be important to include the probability of the galaxies without companions. However, we do not have any halo mass estimates for those galaxies that do not belong to any groups and this basically results in difficulty representing them in the plots above. Alternatively, assuming that all of these isolated galaxies have a halo mass less than the minimum halo mass

in each volume-limited sample, we have learned that the combined relative probability of finding them in a halo mass less than the minimum halo mass is always smaller than the relative probability of finding PSCz galaxies in the smallest mass halo represented in the plots. The combined relative probability of the isolated galaxies for V2M1, V2M2 and V2M3 are 0.3, 0.53 and 0.1 respectively. When these combined probabilities spread out to different halo masses, the effect is even smaller. In all the three cases, these probabilities indicate that the relative probability trend goes even smaller than the minimum value seen in each cases. Therefore, it is safe to conclude that the relative probability of finding PSCz galaxies in isolation is very minimal and exclusion of the isolated galaxies does not change the result at all.

3.4.4 The halo size distribution of LIRGs and non-LIRGs

Having seen the probability distribution for the entire L_{IR} range in each of the samples, we now try to deal with LIRGs and non-LIRG IR galaxies separately. We followed a similar procedure to the case in Section 3.4.3 above for the total sample above to come up with a relative probability distribution for them.

We separated PSCz galaxies from each of the three volume-limited samples based on their L_{IR} values into sets with $L_{IR} > 10^{11} L_{\odot}$ and $10.8 \leq L_{IR} \leq 10^{11} L_{\odot}$ to look for any difference between LIRGs and non-LIRG IR galaxies. We do not, however, expect to see much difference as the L_{IR} values for the latter set are very near to the transition from non-LIRG IR galaxies to LIRGs.

We bin both LIRGs and non-LIRGs in a halo mass size of 0.4 dex and divide each bin by the total number of galaxies in the sample to come up with a probability distribution. The distributions in each of the three volume-limited samples are shown in the different panels of Figure 3.10 for LIRGs and Figure 3.11 for the non-LIRG IR galaxies. In each of the panels, the probability distribution of 2MRS galaxies is exactly the same as with all the other cases. We used the 2MRS density distribution both to remove the mass function effect and finally to find the relative probability of finding the given IR sample galaxies at a given mass halo.

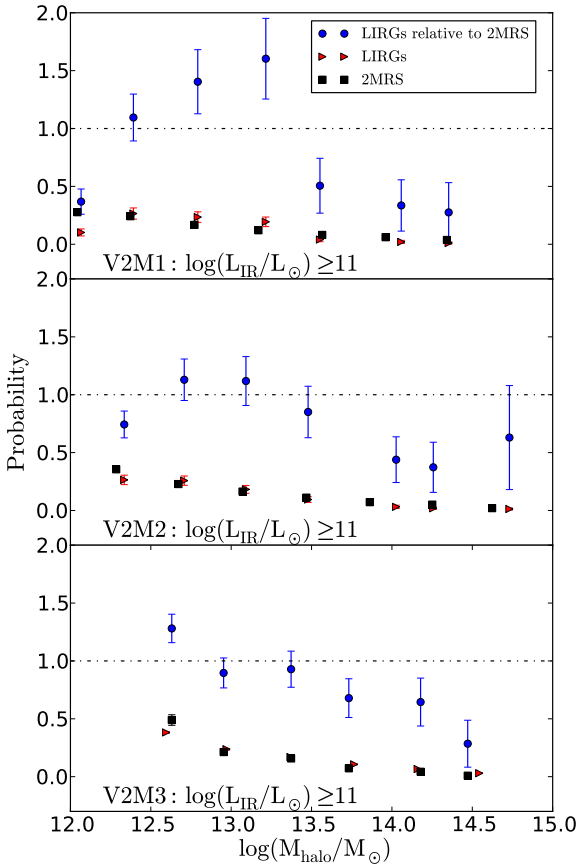

Figure 3.10: The probability of finding LIRGs and 2MASS galaxies in a certain range dark matter halo mass. The red points represent the probability for LIRGs, the black for 2MASS and the blue represent the relative probability of LIRGs in relative to 2MASS galaxies.

For the same reason discussed above, the probability distributions in all the panels in Figure 3.10 and 3.11 do not include isolated LIRGs and non-LIRG IR galaxies. The contribution from the isolated galaxies in the LIRG sample for V2M1, V2M2 and V2M3 are 0.24, 0.47 and 0.87 respectively. In the non-LIRG IR samples, these figures for V2M1, V2M2 and V2M3 are 0.025, 0.1 and 0.3 respectively. When these numbers spread out to different halo masses, the effect gets even smaller.

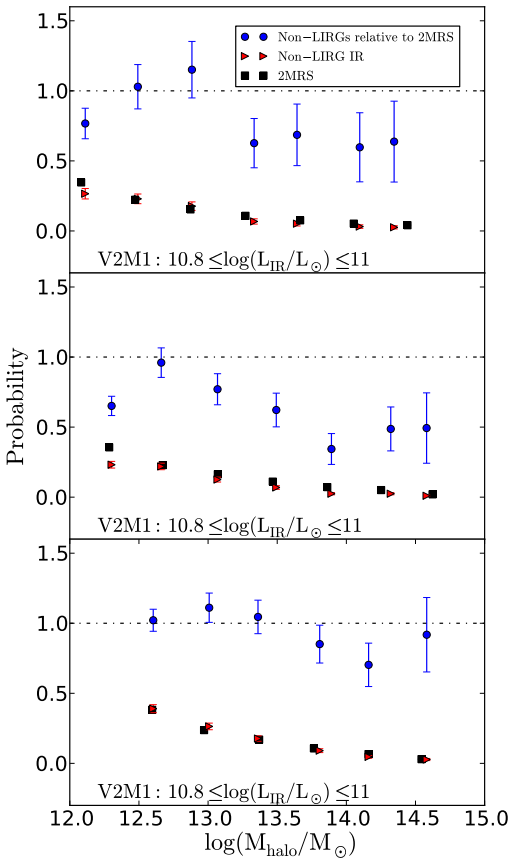

Figure 3.11: The probability of finding non-LIRGs and 2MASS galaxies in a certain range dark matter halo mass. The triangles represent the probability for non-LIRGs, the squares for 2MASS and the circles for relative probability of non-LIRG infrared galaxies in relative to 2MASS galaxies.

The result for the LIRGs (see Fig. 3.10) seems to indicate that the relative probability of finding LIRGs in cluster environment and field environment is very minimal. Their distribution peaks in the halo mass range of $10^{12.5}L_{\odot} - 10^{13.5}L_{\odot}$, which is a group size halo (Kauffmann et al. 2004). The probability of finding LIRGs in haloes of mass $\sim 10^{13}L_{\odot}$ in V2M1 is higher than finding 2MRS galaxies at the same halo size. On the other hand, the distribution for LIRGs at halo of mass $\sim 10^{13}L_{\odot}$ in V2M2 sample and at a halo mass $\sim 10^{13.5}L_{\odot}$ in V2M3 is at least as much as distribution of 2MRS galaxies in this halo mass regime. The results show interesting trend but they are not highly significant given their error bars.

The first two panels of Figure 3.11 reveal that the relative probability of finding non-LIRG

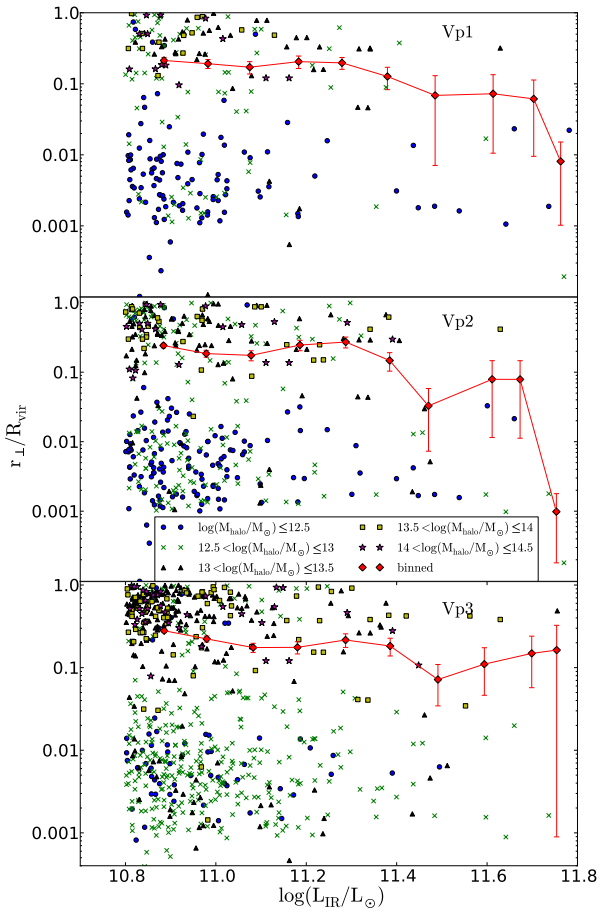

Figure 3.12: The distribution of the projected distances of LIRGs from the galaxy system centre in units of the virialized radius versus their L_{IR}. The red lines represent the binned values in the L_{IR} and the different markers different sizes of halo mass.

IR galaxies in a group environment is higher than finding them in cluster and field environments. However, the result is not as strong as the case for LIRGs. In fact, the last panel in the same figure illustrates that the relative probability of finding them in any environment is almost the same. Given their high SFR and disturbed morphology, the result in the last panel seems to contradict their SF mechanism.

3.4.5 Distance from the centre of galaxy groups

In the previous section, the kind of environment that the LIRGs in our sample prefer to live in, is revealed. Here in this section we want to investigate the influence that physical location inside the group or cluster might have on the SF property of LIRGs. This is done by exploring how close the LIRGs in our sample live to the centre of the group or cluster they are associated with.

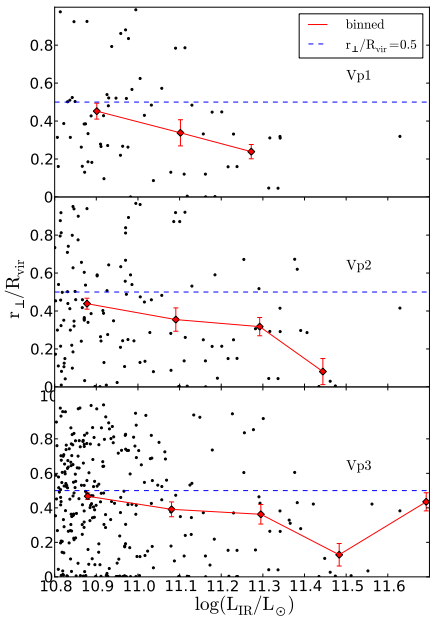

Figure 3.13: The distribution of the projected distances of non-field LIRGs from the galaxy system centre in units of the virialized radius versus their L_{IR}. The red lines represent the binned values in L_{IR}.

It is known which PSCz galaxies (or LIRGs) from all the three volume-limited sample are associated with galaxy groups. In the same section, projected distances ($r_{\perp}$) from the centre of their respective galaxy group are already calculated for each of the galaxies. These projected distances are normalised by the virial radius (R_{vir}) of the groups that the galaxies belong to. Figure 3.13 shows the distribution of the normalised distance (in a logarithmic scale) versus L_{IR} values of the individual galaxies. The different colours show the different halo mass range of the groups of the galaxies. The distribution is binned along the L_{IR} axis in a bin size of 0.2 dex and the red diamonds represent those points.

The figure reveals that the galaxies belonging to higher mass haloes tend to live further out from the centre than the galaxies that belong to small mass haloes, on average. The galaxies with small halo mass (most of which are in fields) live almost at the centre of their parent haloes. This is not surprising, because most of the field galaxies (isolated cases) in our sample are by themselves anyway. According to the trend from the binned points (the red diamonds), it is apparent that the galaxies in our sample prefer to live within $0.5R_{vir}$ radius around the group centre. Moreover, the projected distance declines at a slow rate with L_{IR}.

There is a danger that this result could be biased by the presence of field galaxies. Therefore, the field galaxies are removed from the sample and the distribution is re-plotted in Figure 3.13. The plot shows that the trend still declines with L_{IR}.

3.5 Discussion

LIRGs are often involved with major mergers. In order to fully explain their SF activity in the context of ΛCDM, it is therefore crucial to understand major merger and the associated physical processes driving mergers such as environmental factors in the context of ΛCDM theory. According to this theory, galaxy mergers, especially in group or cluster environments, take place during the merging of sub-haloes (haloes of individual or satellite galaxies) within their parent halo. The merging processes among sub-haloes and among galaxies are therefore two inseparable phenomena. Whatever process is happening to sub-haloes, affects the galaxies inside. Thus, it is also crucial to understand the merging process between sub-haloes in order to better understand the merging process of galaxies inside them.

Analytical studies show that the rate of major sub-halo mergers[1] decline with internal velocity of host halo and increases with sub-halo mass (Mamon 2000; 1992). This major merger rate (R_{mm}) in terms of these two parameters can analytically be expressed as:

$$R_{mm} \propto n_s G^2 m_s^2 / V_h^3, \tag{3.19}$$

where m_s is the sub-halo mass, V_h is the internal velocity in the host halo and n_s is the number density of potential major merger partners.

The internal velocity of haloes is a strong function of the host halo mass. The higher the host halo mass, the higher the internal velocity and vice versa. Therefore, the relationship between major merger rate of sub-haloes can be restated as: major merger rate of sub-haloes declines with host halo mass and increases with sub-halo mass. The former rate determines the environment while the latter rate determines the different aspects of the merging galaxies including their gas content and motion. According to this argument, for a given sub-halo mass, the rate of major merger is higher in groups than in clusters. In other words, it is more likely that one finds merger induced star forming galaxies in groups rather than in clusters.

[1]Major merger is a merger between two equal mass systems.

3.5.1 What halo size do LIRGs live in?

Considering LIRGs as a product of a major merger of two sub-haloes each with gas-rich galaxies in it, the result found in this work (their existence in a group environment) is consistent both with the level of their SFR and the SF mechanism which involves interaction and major merger.

For the specific purpose needed in this Chapter, the local environment of a galaxy is defined in terms of the size of the virialized halo (referred to as host halo) containing the surrounding galaxies that are bound by their mutual gravitational attraction. Based on the mass of the host dark matter halo, the environment can be roughly classified into the traditional and general environmental classes: field, group and cluster categories. A dark matter halo with $M_{halo} \leq 10^{13} M_{\odot}$ is classified as field; $10^{13} M_{\odot} \leq M_{halo} \leq 10^{14} M_{\odot}$ is classified as group and $M_{halo} \geq 10^{14} M_{\odot}$ is classified as cluster (Kauffmann et al. 2004).

By adopting the classification above, we understand that the probability of finding LIRGs in a small group (transition between field and group environment) is the same as or slightly higher (1.3 times in some cases) than the probability of finding 2MRS galaxies in the same halo size. Finding LIRGs in field and cluster environments, on the other hand, is very small as compared to finding 2MRS galaxies in the similar environments.

The probability of finding LIRGs and 2MRS galaxies in group-like environment is not very much different. Both of these galaxies live in a similar density environment. When one compares these two types of galaxies, their difference is not mainly from the difference in their environment. The difference should possibly be in their gas contents.

The L_{IR} range of the LIRGs which are found in association with galaxy systems in all the three volume-limited samples is between $10^{10.8} L_{\odot}$ and $10^{11.6} L_{\odot}$ with a considerably reduced fraction of galaxies at the higher L_{IR} end in the range. As a result, it is not possible to extend the result for the entire spectrum of LIRGs. However, in Chapter 2 it is found that the L_{IR} values of LIRGs is correlated with local density even up to higher L_{IR} values (see Fig. 2.13 in Chapter 2). According to that result, the higher L_{IR} value LIRGs are essentially in an intermediate environment between group and cluster and the ULIRGs in the sample are already in cluster environment. Based on this result, we predict that if the relative probabilities were determined in different L_{IR} bins and the result would cover the entire LIRG and ULIRG regime, the halo mass at which the relative probability peaks up would progressively increase with L_{IR}. An attempt made to split the result at least into two bins with $L_{IR} \leq 10^{11} L_{\odot}$ and $L_{IR} \geq 10^{11} L_{\odot}$ to see if there is any trend in the halo mass with L_{IR} did not show clear differences (see Figs. 3.9 and 3.10). This is perhaps because there is not much difference between galaxies so close to the $L_{IR} = 10^{11} L_{\odot}$ limit from both sides.

3.5.2 What is the star formation mechanism?

As it is shown in Chapter 2 and predicted above, inside the ULIRG regime the environment is already that of a cluster. This suggests that either another mechanism of SF is already in action

for ULIRGs ((Martig & Bournaud 2008); See Section 2.6.6 for detail explanation) or that even if ULIRGs are associated with clusters, they are actually situated in the peripheral regions of clusters where the velocity dispersion is close to that in group environment. According to the second scenario, ULIRGs could then be associated with groups that are still in the process of falling into clusters. This agrees with analytical results for the relationship between the merger rate and clusto-centric radius (distance from the centre of a cluster). Merger rate increases with clusto-centric radius within cluster environments (Mamon 1992). The natural extension of this is, if one could probe the entire ULIRG regime, it would not be surprising if the L_{IR} value of ULIRGs is not correlated with local density above a certain luminosity limit. As one approaches the centre of a cluster, the environment gets too crowded to have an interaction that could potentially result in L_{IR} values seen in ULIRGs. Or the other alternative is that while the centre of a cluster would be favourable for interaction triggered SF, but in clusters that are found in the local Universe SF has already been quenched at their centre for various reasons such as gas exhaustion. Since our sample does not cover the entire LIRG and ULIRG regime, it is not, unfortunately, possible to test the above idea with our data.

3.5.3 Where exactly in groups or clusters do LIRGs live?

With the limited sample (low L_{IR} LIRGs) we have, in Figure 3.13, it is shown that on average, all the LIRGs that are not in field environment from all the three volume-limited samples, prefer to reside within $0.5R_{vir}$ radius around the centre of their host halo (see the curves in red). Moreover, L_{IR} increases as galaxies get closer to the centre. Studies on the interactions of LIRGs and ULIRGs indicated that a separation less than or equal to $0.5R_{vir}$ between the two cold gas-rich components of LIRGs and ULIRGs are efficient in resulting in hydrodynamical interaction that funnels cold gas to the central region of the interacting systems (Hwang et al. 2010). Taking this separation distance into account, the fact that the LIRGs in our sample on average live within the same size radius from the centre hints that there is a possibility that interactions that give rise to LIRGs are interaction between a gas-rich satellite galaxy and another central galaxy sitting at the very centre of the host halo. However, often, galaxies at the centre of groups or clusters are early type hot gas dominated (Feldmann et al. 2010, Zabludoff & Mulchaey 1998) and hence interaction with the central galaxy does not seem to work in producing a SF level seen in LIRGs. The other alternative is that LIRGs might be of course residing within $0.5R_{vir}$ radius but their interacting pair is outside of this radius.

When the host halo grows in mass (and by implication in physical size), LIRGs tend to move out from the centre of their host halo. According to the different colour markers in Figure 3.12, we can see that on average the location of low luminosity LIRGs with respect to the centre of their host halo correlates with the mass of their halo. For example, one can note from the same figure that LIRGs in cluster environment ($M_{halo} \geq 10^{14} M_{\odot}$) are relatively farther out from their host centre than the LIRGs which are in group environment ($10^{13} M_{\odot} \leq M_{halo} \leq 10^{14} M_{\odot}$). This

in other words means that as the mass and size of the dark matter halo LIRGs are associated with increases, they tend to live further out from the centre, they are further out in clusters than in groups. This is in agreement with the possibility of SF quenching at the very centre of clusters or some other unfavourable environmental factor that would not allow SF to happen (e.g. high velocity fly-by interaction). No matter what the reason is, this result is observationally supported.

The fact that the binned results in all the three panels both in Figure 3.12 and Figure 3.13 indicate LIRGs live within $0.5R_{vir}$ radius, is not a surprising result. This is because LIRGs have a high probability of living in groups or rich fields, not in clusters, and the velocity dispersion of galaxies at the very centre of groups or rich fields is not as high as the case in clusters.

3.6 Conclusions and summary

This Chapter investigated the relation between environment and SF of local LIRGs by characterising their local environment not with galaxy counts, but with the size of their dark matter haloes. Three volume-limited LIRG samples were drawn from the PSCz sample and the environment around the LIRGs was characterised based on the 2MRS volume-limited samples. Halo masses and other physical parameters such as dispersion velocities and K-band magnitudes were determined for the galaxy systems the LIRGs in our sample live in.

A comparison between the likelihood of finding LIRGs and 2MASS galaxies in a certain halo mass (environment) bin was made. It was found that the relative probability of finding LIRGs appears to be very low both at the high mass range (cluster) and in the low mass (field) environments. The highest relative probability was found to be at a halo mass near the transition between field and group. Given the L_{IR} distribution of our sample (mostly low-L_{IR} LIRGs) and the correlation found between the environments of LIRGs and their corresponding L_{IR} values in Chapter 2, the result seems consistent both with their level of SF and their already known effective SF mechanism.

It was found that LIRGs, on average, live within $0.5R_{vir}$ radius of the centre of the galaxy system they were associated with. In addition, on average, their clusto-centric distance and their L_{IR} were anti-correlated. The ones very close to the centre form stars at a higher rate. This result seems to agree with the general process of SF within group size environment. Processes such as interaction and mergers are more effective close to the centre of group size environments than at the outskirts.

The clusto-centric distance of the LIRGs is found to be a function of the halo mass of the galaxy system they belong to. As the halo mass increases, LIRGs tend to move further out from the centre. This is true especially in the transition from group size to cluster size halo. This is also in agreement with the fact that the high SFRs exhibited by LIRGs are not expected inside cluster cores because velocities are very high so that tidal stripping should be more effective than merging. However, in the outskirts of clusters, the existence of LIRGs can be explained

by the combination of interaction (because at the outskirts of clusters velocity dispersions are lower than in the cores) and the tidal force of their cluster. Even if they are not ULIRGs, LIRGs that are associated with cluster size haloes tend to reside more in outskirts than near the core of their haloes.

The L_{IR} range of the LIRGs which are found in association with galaxy systems in all the three volume-limited samples is between $10^{10.8}L_{\odot}$ and $10^{11.6}L_{\odot}$ with a considerably reduced fraction of galaxies at the higher L_{IR} end in the range. As a result, it is not possible to extend the result for the entire spectrum of LIRGs. However, in Chapter 2 it is found that the L_{IR} values of LIRGs is correlated with local density even up to higher L_{IR} values (see Fig. 2.13 in Chapter 2). According to that result, the higher L_{IR} value LIRGs are essentially in an intermediate environment between group and cluster and the ULIRGs in the sample are already in cluster environment. Based on the result from Chapter 2, we predict that if the relative probability of finding LIRGs in a certain halo mass were determined in different L_{IR} bins and the result would cover the entire LIRG and ULIRG regime, the halo mass at which the relative probability peaks up would progressively increase with L_{IR} for PSCz-volume limited sample.

4

The Chemical Abundance of Dwarf Irregular galaxies

4.1 Introduction

Dwarf irregular galaxies are among the most unevolved galaxy systems in the Universe (Kunth & Östlin 2000). They have a very large ratio of total hydrogen to total mass (Fisher & Tully 1975) implying that they have not used up all their gas. In addition, when compared to spirals, for example, they seem to be less efficient in heavy element production. This means that, despite their abundant gas content, they have not converted much of their gas into stars yet. Knowing that star formation is the means of heavy element production in galaxies, their inefficiency in producing heavy elements could indicate that their star formation mechanism might not be as efficient as in other types of galaxies such as galaxies whose star formation is triggered by environmental factors.

Just like other non-dusty star forming galaxies, dIrrs host massive HII regions and hence the study of these HII regions within them provides an important insight into their chemical evolution and their star formation history. Powered by the process of star formation, the HII regions in dIrrs just like HII regions in other types of galaxies are dominated mainly by forbidden emission lines like [OII]λ3727 3729, [OIII]λ4959,5007, [NII]λ6548,6583 and recombination lines of hydrogen Hα, Hβ, Hγ.

The strength of the emission lines in HII regions is controlled by different factors that include the energy distribution of the ionizing photons, the spatial configuration of the ionized gas and its local properties, essentially its density and metal content. The metal content in HII regions defines the appearance of the emission line spectra. The spectra of HII regions therefore contain

important qualitative and quantitative descriptions of the different physical properties of the HII galaxies. These include: the star formation history, the chemical enrichment of the interstellar medium, gas cooling and metal abundance that help understand the chemical evolution of the galaxies better.

In this work, the oxygen, nitrogen and neon ionic and elemental abundances, electron temperatures as well as information about the dust content of three isolated Southern dIrr galaxies are determined for the first time from the spectra found from their HII regions. It is checked whether the galaxies fit to the already established metallicity-luminosity relationship and a possibility of metallicity gradient is also investigated in one of the three galaxies. These quantities will help understand the chemical evolution of these galaxies with future addition of other information. This small sample project is considered as a pilot project to test the performance of the spectrograph in the newly built the Southern African Large Telescope (SALT) [1] for various future chemical evolution studies on star forming galaxies such as LIRGs and ULIRGs in addition to dIrr galaxies. The chapter is organised in such a way that we first give a brief description of the sample and following that, the observation and data analysis. After that we discuss the results and finally we conclude and present a summary.

4.2 Objective

This chapter has two main objectives. They are:

1. Testing the feasibility of a future project which is based on long-slit observation using the Robert Stobie Spectrograph (RSS) on Southern African Large Telescope (SALT) to understand the spectroscopic properties of dIrr galaxies and interacting star forming galaxies.

2. Determining the elemental and ionic abundances of O, N and Ne as well as the electron temperature of the ionized plasma and information about the extinction effects in three dIrr galaxies.

4.3 Sample

Given the main objective of this work, three HII galaxies (namely: ESO 149-G003, ESO 272-G025 and ESO 074-G015) from a Local Volume Hα survey of eleven isolated Southern galaxies by Kaisin et al. (2007) are identified. The survey presents the total Hα flux, the star formation rate and the gas depletion time of the galaxies. All the three HII regions in the galaxies are all part of the intergalactic HII regions discovered in the NOAO Survey for Ionization in Neutral Gas Galaxies (SINGG) (Ryan-Weber et al. 2004). All the three galaxies lie within 7 Mpc radius

[1] www.salt.ac.za

of the Southern Local Volume. Figure 4.1 shows the Hα as well as R-band images of all the three galaxies taken from Kaisin et al. (2007).

ESO 149-G003 is a dIrr galaxy. It has an oval central region and extended disk-like low surface brightness envelope. It has one clear HII region associated with it (Kaisin et al. 2007, Ryan-Weber et al. 2004) (see Table 4.1 for further details). ESO 272-G025 is a dIrr galaxy surrounded by an extended diffuse halo. Its HII region is located right at the heart of it (see Table 4.2 for further details) (Kaisin et al. 2007).

ESO 074-G015/IC 5052 is an isolated edge-on galaxy (Kaisin et al. 2007). It has many compact HII regions spread out throughout the optically visible part of it (see Table 4.3 for further details). In some works, however, it is reported that it has two prominent HII regions. In Table 4.3, we presented the two prominent HII regions individually.

ESO 149-G003	
RA(J2000)	23:52:02.8
Dec(J2000)	-52:34:39
Distance (Galactocentric)	6.95 ± 0.49 Mpc
Heliocentric velocity (Km s^{-1})	576
Type	Sm
M_B	-14.1
Hα Lum (erg s^{-1})	3.5×10^{36}
log(SFR)	-2.19 $M_\odot/yr$

Table 4.1: Physical characteristics of ESO149-G003 taken from Kaisin et al. (2007), Ryan-Weber et al. (2004).

ESO 272-G025	
RA(J2000)	14:43:25.5
Dec(J2000)	-44:42:19
Distance (Galactocentric)	6.81±0.5 Mpc
Heliocentric velocity (Km s^{-1})	(624±10)
Type	Sc-irr
M_B	-14.8
Hα Lum (erg s^{-1})	
log(SFR)	-2.15 $M_\odot/yr$

Table 4.2: Physical characteristics of ESO 272-G025 taken from Kaisin et al. (2007), Ryan-Weber et al. (2004).

ESO 074-G015/ IC 5052	
RA(J2000)	20:52:59
Dec(J2000)	-69:12:27
Distance (Galactocentric)	6.03 Mpc
Heliocentric velocity (Km s^{-1})	584±3
Type	Sd
M_B	-17.5
The first HII region (ESO 074-G015)	
Hα Lum (erg s^{-1})	1.3×10^{36}
The second HII region (IC 5052)	
Hα Lum (erg s^{-1})	1.7×10^{36}
log(SFR)	-1.05 $M_\odot/yr$

Table 4.3: Physical characteristics of ESO 074-G015/ IC 5052 taken from Kaisin et al. (2007), Ryan-Weber et al. (2004).

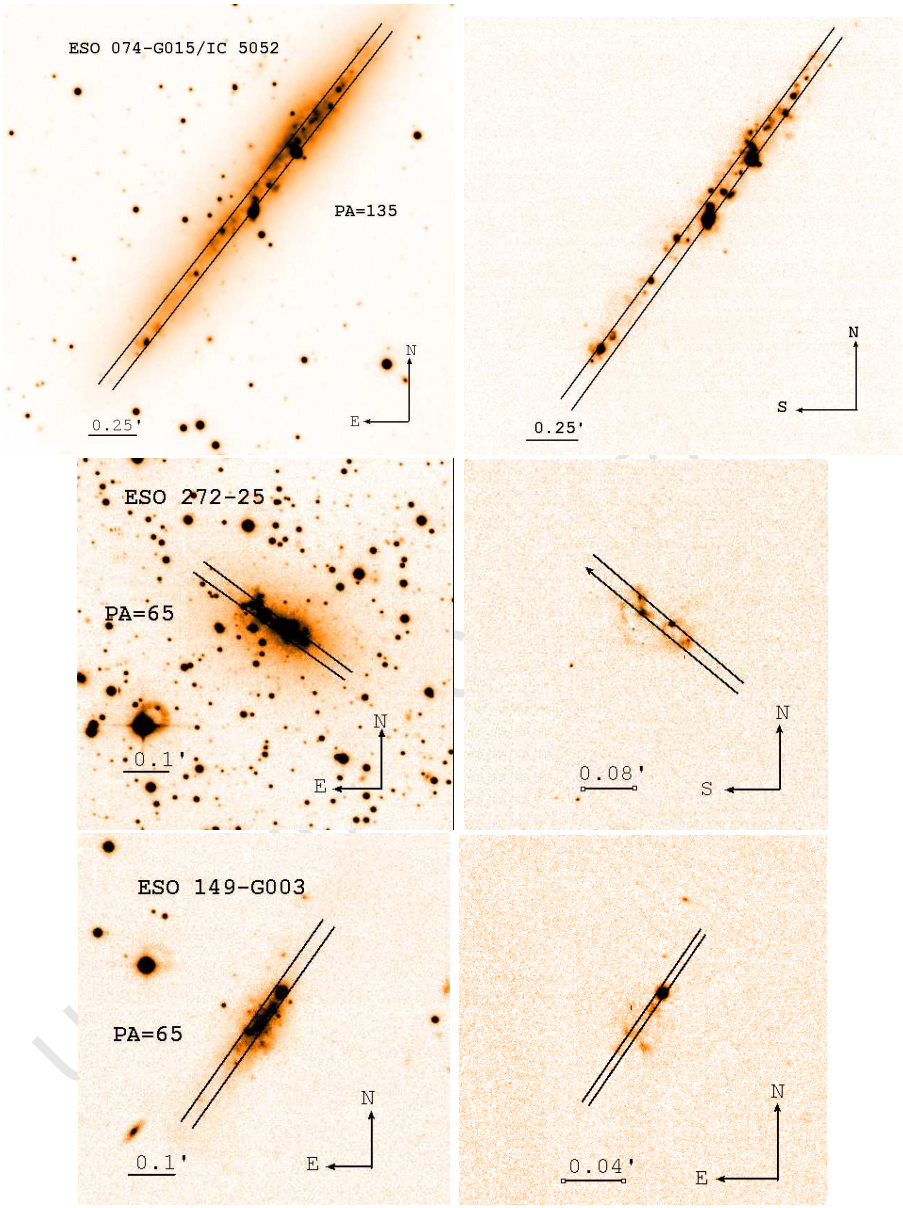

Figure 4.1: *Left panels*: R-band images of the three galaxies with the position angles and the slit position. *Right panels*: Hα images of the corresponding galaxies showing the detected HII regions. Both the R-band and Hα data for all three galaxies are taken from Kaisin et al. (2007) and reproduced.

4.4 Observations

The observations for this work were made with the RSS instrument on SALT during the first performance verification and commissioning phase of the telescope in 2006. As the instruments in the telescope were not fully functional at that moment, all the data we have here are not considered as taken with the full potential of the telescope.

4.4.1 SALT

SALT is a 10m class telescope equipped with instruments capable of doing imaging (SALTICAM) (Buckley et al. 2003; 2004) and spectroscopy (RSS) (Burgh et al. 2003, Kobulnicky et al. 2003). It has an effective field of view of 8' in diameter which makes it suitable for extragalactic observations. The original design of the telescope was based on the Hobby-Eberly Telescope (HET) in Texas. However, many details were modified to ensure that the telescope fits many additional specific requirements.

Figure 4.2: The Southern African Large Telescope (SALT) is an 11 m telescope situated at the South African Astronomical Observatory (SAAO) site in Sutherland. The observations in this work were done using the RSS spectrograph on SALT.

The telescope has 11.1 m × 9.8 m spherical primary mirror that is made up of ninety one hexagonal mirrors operating together. Its mount is Alt-Az design with the optical axis tilted 37 degrees from the vertical. The tracker situated 13 m from the primary mirror tracks objects in the sky by moving up and down parallel to the primary mirror, without the primary changing

the azimuth angle for a period of typically 2 hours. The telescope is situated in Sutherland at the main observational site of the South African Astronomical Observatory (SAAO) [2].

The telescope saw its first light in late 2005 immediately before its inauguration and was operating for performance verification and commissioning until 2007 before its operation was hampered by various issues. The telescope spherical aberration corrector (SAC) had faults leading to image quality issues, while the main instrument (RSS) had a serious throughput shortfall.

The RSS instrument on SALT is a prime-focus spectrograph capable of doing long-slit, multi-object and imaging spectroscopy, together with polarimetric and narrow band imaging capabilities. The instrument makes use of Volume Phase Holographic (VPH) gratings. It has three separate CCD detectors each with 2048×4096 pixels dimension.

Its throughput issue was almost in the entire wavelength coverage but gets worse in the blue end. In Figure 4.3, we present observations done at different wavelengths to show the throughput problem. On the same Figure, the theoretical throughput is also presented for comparison (see the red dots in the Figure).

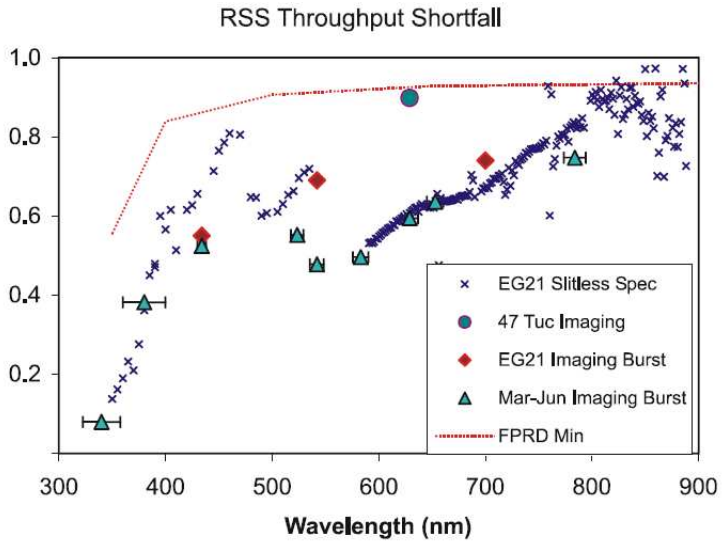

Figure 4.3: The throughput shortfall problem of the RSS instrument on SALT shown with data taken during 2006. The small red dots show the theoretical throughput while the other points show the throughput measured from various observations. The throughput problem is worse in the blue (taken from Southern African Large Telescope RSS Throughput Testing report by Kenneth Nordsieck, 2006).

[2]SALT website: www.saao.ac.za

Currently the problems both on the RSS and the SAC are diagnosed and fixed. Both RSS and SALTICAM are in the process of being returned to the telescope and another phase of commissioning is expected to be started soon.

4.4.2 Observations with RSS

The long-slit data of the three galaxies were acquired using the RSS spectrograph during the performance verification and commissioning phase of SALT which happened between May and August 2006 (Burgh et al. 2003, O'Donoghue et al. 2006) while the RSS was having the throughput problem discussed above. The data were taken over two nights (19 and 24, July 2006) in which the seeing varied between $0.8''$-$2.0''$. The moon illumination in the two nights was 26% and 24% respectively. The physical size of the slit during the entire observation was $1''$ slit width and $8'$ long[3]. The slit width is determined in such a way that it provides good enough spectral resolution and light throughput. Different position angles (PA) were used depending on the orientation of the three galaxies in space and the location of their HII regions within the galaxies themselves. PA angles of 135°, 65° and 135° are used for ESO 074-G015/IC 5052, ESO 272-G025 and ESO 149-G003 respectively. The orientation of the galaxies and the corresponding PA of the slit is illustrated in Figure 4.1 both in R-band and Hα.

A PC03400 order blocking filter and PG900 grating with 13.63° grating and 27.25° camera angle were used in the observations. This set-up using 1" wide slit allowed a spectral resolution of $R \sim 1000$ which is sufficient for the identification of emission lines close to each other for our abundance determinations. For example, we are able to identify the [NII]λ6548 and [NII]λ6584 separately from the Hα line. The set-up also allowed a spectral coverage of 3626-6710Å which is wide enough to include spectral features such as [OII]λ3727 and Hα, the most important lines for our abundance measurement. A 2×2 binning was employed to get a final spatial sampling of $0''.258$ pixel^{-1}.

Two standard stars were observed during the two nights after the science frames (ESO 074-G015 and ESO 149-G003) following an arc in each case. However, in the case of the first galaxy (ESO 272-G025), the standard star observed for target ESO 074-G015 was used. Immediately after each of the observation, a CuAr arc was taken.

A summary of the sequence of observations, exposure times and other details are presented in Table 4.4.

[3]The physical length of the slit is equivalent to the $8'$ by $8'$ field of view of SALT.

Observational details

Date	Object	RA J2000	Dec. J2000	Exp. time (Sec)	Spectral Range (Å)	slit width (arcsec)	Observation Type
19-07-2006	ESO 272-G025	14 43 25.5	-44 42 19	2×600	3627-6710	1	science frame
	CuAr			90	3626-6710	1	Arc
	E074-G015	20 52 00	-69 11 36	2×600	3635-6710	1	science frame
	CuAr			60	3626-6710	1	Arc
	G93-48	21 52 25	02 23 24	2×600	3626-6710	1	Standard
	CuAr			60	3626-6710	1	Arc
24-07-2006	ESO 149-G003	23 52 00	-52 34 40	600	3626-6710	1	science frame
	CuAr			90	3626-6710	1	Arc
	LTT1788	03 48 22	-39 08 33	600	3626-6710	1	Standard
	CuAr			90	3626-6710	1	Arc

Table 4.4: A summary of the observational details of the long slit observations of the galaxy sample.

4.5 Data reduction and analysis

4.5.1 Primary data reduction

The primary data reduction, which prepares individual frames for the main data reduction process, was done using the SALT[4] package in IRAF [5]. The reduction includes: bias subtraction, overscan correction and trimming, gain correction and cross-talk correction. Since RSS has three CCD detectors (each with 2048×4102 pixels) operating together, each observation has three frames. The gain and readnoise therefore vary from one CCD to the other and hence gain correction was important. After that, the PMOSAIC task in IRAF was used to merge the three individual frames for each observation. Finally, before the spectral reduction, cosmic ray removal was done using the XDIMSUM/XZAP task. A comparison of one of the science frames before and after the primary data reduction, PMOSAIC and cosmic ray removal is shown in

[4]See http://www.salt.ac.za/science-support/salt-data-reduction/

[5]The Image Reduction and Analysis Facility is distributed by The National Optical Astronomy Observatory (NOAO), which is operated by the Association of Universities for Research (AURA) under cooperative agreement with the National Science Foundation (NSF).

Figure 4.4.

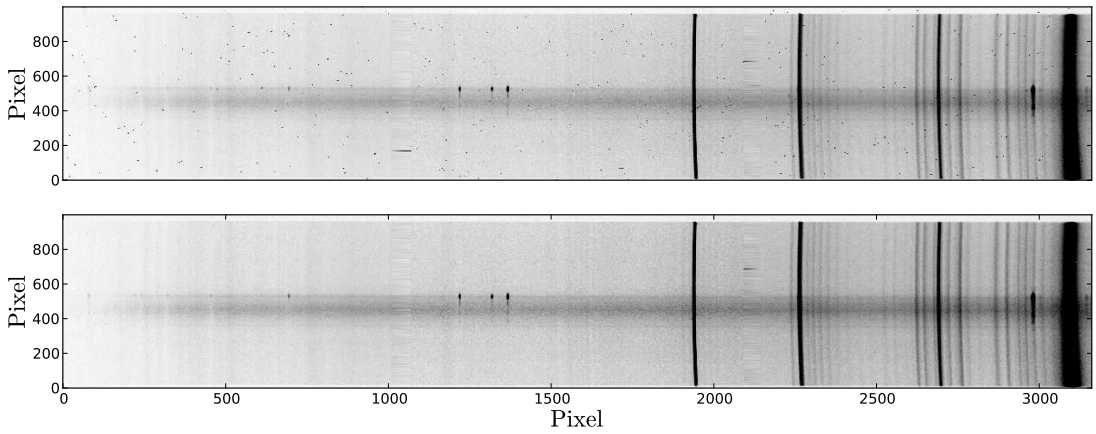

Figure 4.4: *Top panel*: A 2-dimensional (2D) raw spectrum of ESO 149-G003 before primary reduction. *Bottom panel*: A 2D spectrum of the same galaxy after primary reduction. The primary reduction includes bias subtraction, overscan correction and trimming, gain and cross-talk correction, and cosmic ray removal. As an example one can note that the effectiveness of the process of the cosmic ray removal by comparing the two panels.

Once the primary reduction was done, the spectral data reduction processes that include wavelength distortion corrections, wavelength and relative flux calibrations and background subtractions were done using various tasks from IRAF TWODSPEC package in their interactive mode. Even if there were flats observed during each night, we did not use them because at the time of observations the detector response variation of SALT was not well understood. Therefore, none of the observations are flat-fielded.

4.5.2 Reference spectra (Arc) reduction

Wavelength calibration of all the reference spectra were done using the IDENTIFY and REIDENTIFY tasks. In every single reference spectra, a minimum of 20 spectral lines were identified. The centres of each of the identified lines were determined and their positions were fitted with a fifth order Chebyshev function to determine a wavelength solution. This wavelength solution was used to wavelength calibrate the arcs. The wavelength calibration was done with a dispersion solution of RMS values ≤ 0.66Å for all the arcs.

All the frames had wavelength distortions, i.e. there were slight wavelength variations of a given emission line along the spatial axis. As a result of this, emission lines appeared in all the spectra to be curved in the spatial axis. The correction for this effect was based on the 2D

solution found from straightening the arcs. The task used to find the 2D solution from the arcs is the FITCOORD task.

4.5.3 Standard star reduction

The standard stars were both wavelength calibrated (IDENTIFY and REIDENTIFY tasks) and wavelength distortion corrected (TRANSFORM task) using the solution found for the nearest arc in time (see Section 4.5.2) and finally background subtracted (using BACKGROUND task). After this had been done, a sensitivity function was derived for each of the standards by which the science frame flux calibration was made. The sensitivity functions were derived from a comparison of APALL-extracted spectrum of the standard star observation to the real spectral energy distribution (SED) of the same standard stars. Since the standard star observation was not corrected for any flux loss due to the narrow slit width and other potential instrumental effects such as the variable pupil size of SALT, the sensitivity function was used only for a relative flux calibration of the science frames. We present in Figure 4.5 a flux calibrated 1-dimensional spectrum of one of the standard stars, G93-48).

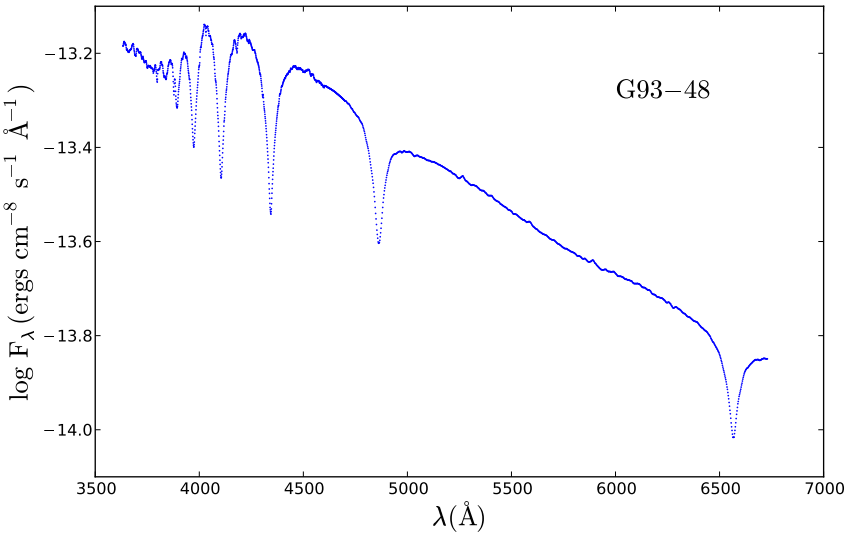

Figure 4.5: The spectral energy distribution of the spectrophotometric standard star (G93-48) recovered by the sensitivity function derived from observational data of the star.

4.5.4 Science frame reduction

Once wavelength calibrations, wavelength distortion corrections and background subtractions were made, the science frames were flux calibrated using the sensitivity functions from the standard stars. The sensitivity function used for each of the galaxies was derived from the standard stars observed in the same night the science observations were made. The standard star, G93-48, is used to calibrate science targets ESO 272-G025 and ESO 074-G015 while the standard star LTT1788 is used to calibrate ESO 149-G003 (see table 4.4 for a description of the sequence of observations done).

Finally, in order to improve the signal of the observations, targets with more than two exposures (ESO 272-G025 and ESO 074-G015) are median combined before they are used for any science analysis. In Figure 4.6, we show 2D spectra of galaxies ESO 149-G003 and ESO 272-G025 after all the reduction was made on each of them. One can note the difference between these final frames and the top spectra of Figure 4.4 which is before any reduction was made on it. Most importantly, all the sky lines are gone after the reduction and the emission lines stand bright.

In order to do the main analysis, a one dimensional (1D) spectrum from the two dimensional spectra of each of the three galaxies was extracted using the APALL task from IRAF. The aperture of the extraction was done at a location in the spatial direction in which all the emission lines including the very weak ones such as [OII]λ3727 were present. The width of the aperture was determined by the physical extent of the lines, i.e. it was as wide as the size of the physically smallest emission line. The extracted 1D spectra are presented in the three panels of Figure 4.7.

The lines [OII]λ3727, [NeIII]λ3869, Hδ, Hγ, [OIII]λ4363, Hβ, [OIII]λ5007, [NII]λ6548, Hα and [NII]λ6584 were clearly identified and their fluxes were measured using the SPLOT package of IRAF. The flux measurement was made by fitting a Gaussian profile to the emission line. The fitting process uses an iterative algorithm based on the Levenberg-Marquart[6] method. The continuum level was estimated by the software based on the initial continuum level given by the user from a close visual examination of both sides of the emission lines. In cases where there were blended lines, a double Gaussian was fitted to de-blend them. Figure 4.8 demonstrates a snapshot of the Gaussian profile fit to Hα emission line of the galaxy ESO 272-G025. The software finally outputs the flux, $F(\lambda)$, the central wavelength and equivalent width.

Error estimation for the measured quantities was done using the same SPLOT task on the flux uncalibrated files. Later, these percentage errors are adopted to the flux and equivalent width measurements from the flux calibrated files.

[6]Levenberg–Marquardt algorithm provides a numerical solution to the problem of minimising a function, generally non-linear, over a space of parameters of the function

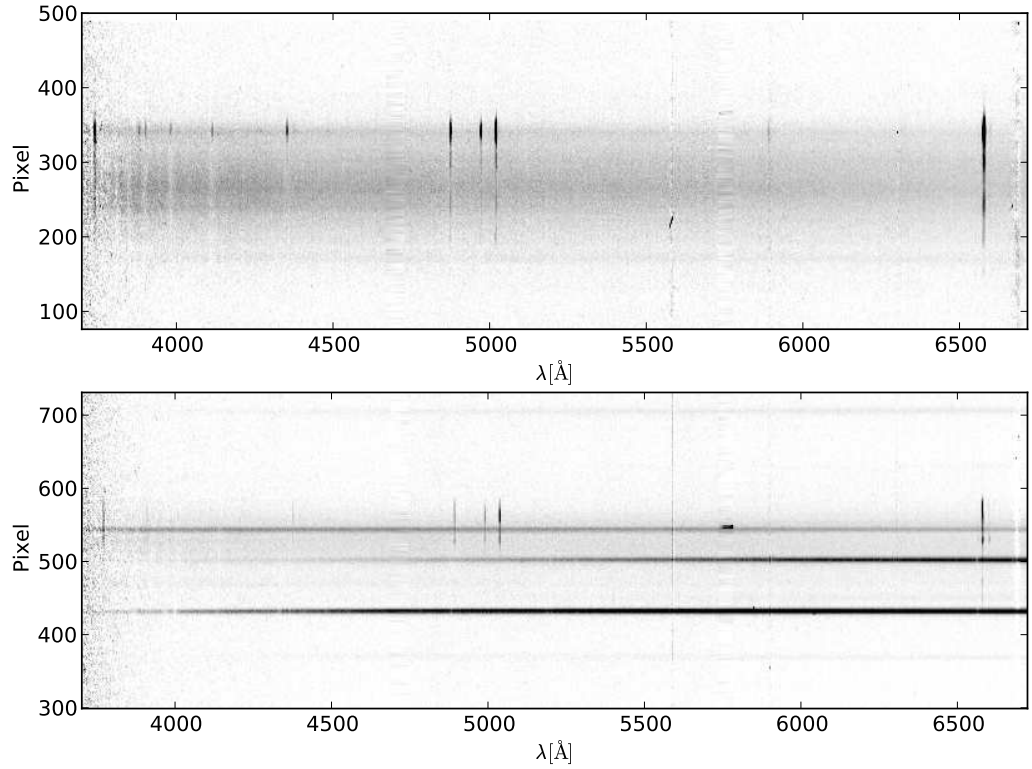

Figure 4.6: 2D spectra of two of the galaxies. *Top panel*: The spectrum for ESO 149-G003. This galaxy has an extended HII region in which [OIII]λ4363 is visible only at one extreme end. *Bottom panel*: The spectrum for the galaxy ESO 272-G025. The spectrum includes three star-like objects also.

4.5.5 Reddening and stellar absorption correction

All the observed hydrogen fluxes were corrected both for reddening and underlying stellar absorption to recover the intrinsic fluxes, $I(\lambda)$, following the treatment by (Izotov et al. 1994, and references therein) & Kniazev et al. (2008). The correction involved the determination of absorption equivalent width, $EW_a(\lambda)$, and the absorption coefficient, C(Hβ), by comparing them to their respective theoretical ratio using the expression:

$$\frac{I(\lambda)}{I(H\beta)} = \frac{EW_e(\lambda) + EW_a(\lambda)}{EW_e(\lambda)} \frac{EW_e(H\beta)}{EW_e(H\beta) + EW_a(H\beta)} \frac{F(\lambda)}{F(H\beta)} \exp\left[C(H\beta)f(\lambda)\right], \tag{4.1}$$

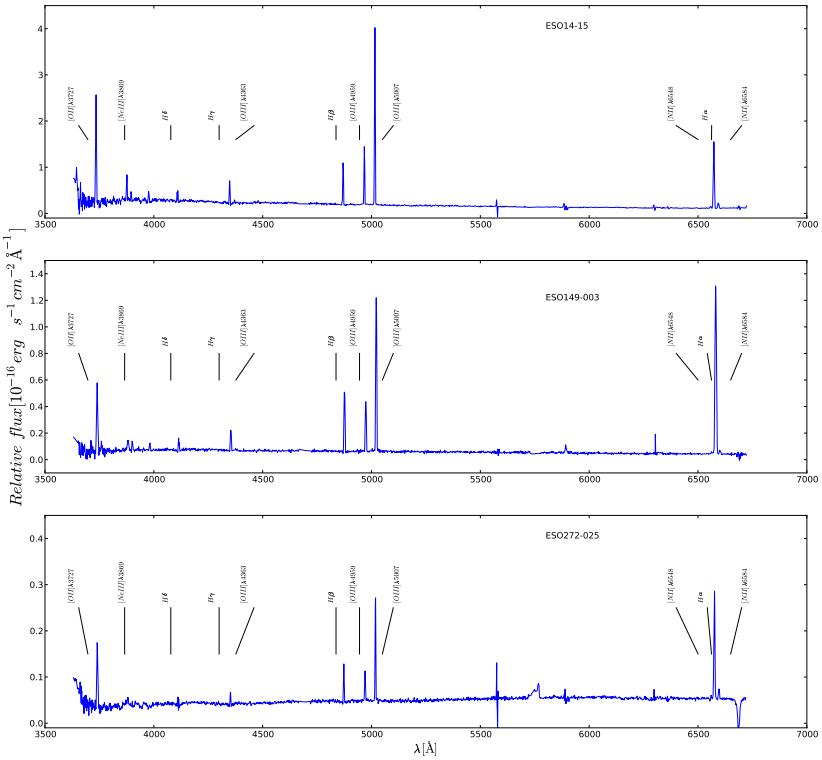

Figure 4.7: One dimensional spectra of the three galaxies presented to show the different features detected. In all three galaxies, the most important lines that can be used to employ a direct method of abundance determination are detected.

where I(λ) is the intrinsic line flux and F(λ) is the observed line flux. EW$_e(\lambda)$ and EW$_a(\lambda)$ are the equivalent widths of the observed emission lines and the stellar absorption lines respectively. We assumed a constant absorption equivalent width for all the hydrogen lines , i.e., $EW(H\alpha) = EW(H\beta) = EW(H\gamma) = EW_a$ (Izotov et al. 1994, Kurucz 1979). This is a fair assumption given some authors found the mentioned equivalent widths are similar within 30% for any given star (Kurucz 1979).

The parameter f(λ) is function derived to represent the dependence of the redenning on wavelength and is called the reddening function. There are different forms reddening function, modeling the dust absorption effects (e.g. Whitford 1958, Savage & Mathis 1979) in a different way. This particular work adopted a reddening function originally determined by Whitford

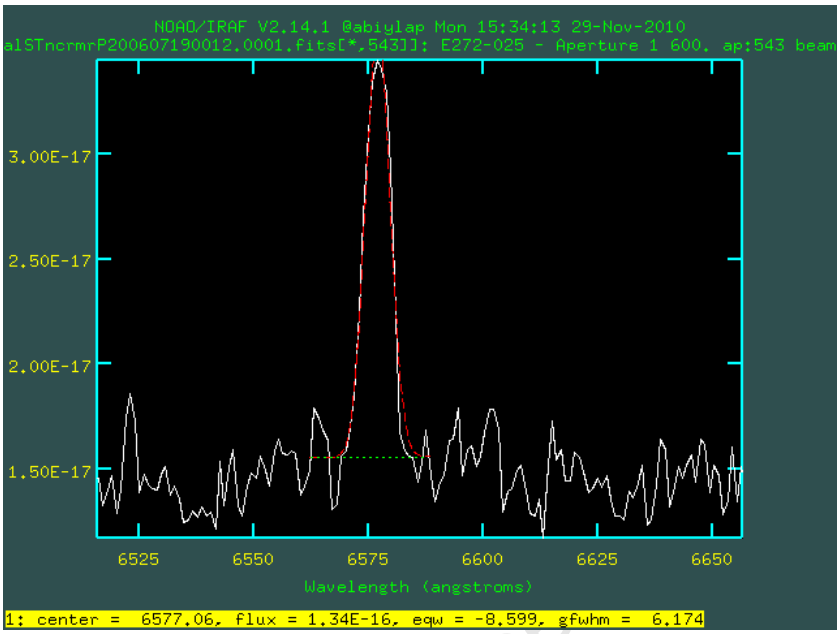

Figure 4.8: A snapshot of a Gaussian fit to the Hα emission line of the galaxy ESO 272-G025. The red dashed lines represent the fitting.

(1958) and later approximated to an accuracy level better than 5% by Izotov et al. (1994) for the entire wavelength regime. The approximate function is widely used in various previous works (e.g. Kniazev et al. 2004, Izotov et al. 1994, Kniazev et al. 2008, Pilyugin et al. 2010) and has produced robust and reliable results. The function, normalized by $H\beta$ is presented as:

$$f(\lambda) = 3.15854 \times 10^{-1.02109\lambda} - 1, \tag{4.2}$$

where the unit used for λ is μm.

Normally the theoretical ratios of the Balmer recombination lines are temperature sensitive, though in most cases this temperature dependence is neglected because it is very weak. In this work, however, we chose to consider the temperature dependence and as a result the correction of the observed hydrogen lines for the absorption effects are temperature dependent. The temperature of the HII regions is also important for the main purpose of this work which is determining the chemical abundances of the different metals because abundances are determined from temperature. The entire process of reddening correction, C($H\beta$), stellar absorption correction (determining EW_a) and determining the electron temperature are interdependent. Therefore, these three parameters, together with other parameters, were determined iteratively.

The theoretical temperature dependent hydrogen recombination lines were taken from (Brocklehurst 1971) and presented as:

$$\frac{H\alpha}{H\beta} = -0.21\ \log(t) + 2.89, \tag{4.3}$$

$$\frac{H\gamma}{H\beta} = 0.01\ \log(t) + 0.47, \tag{4.4}$$

$$\frac{H\delta}{H\beta} = 0.01\ \log(t) + 0.26, \tag{4.5}$$

where $t = 10^{-4}T$. These different equations at the correct temperature (see Section 4.5.6 for detail explanation of the temperature determination) together with Equation 4.1 are used to calculate C($H\beta$) and EW_a.

The errors for the corrected line ratios, C($H\beta$), EW$_e$ and EW$_a$ were calculated from Monte-Carlo simulations. A thousand possible Gaussian random values based on the observational uncertainties for each of the observed Balmer lines were produced. The Gaussian had the observed values as its mean and their corresponding errors as its width. Using each of these lines, we produced possible corrected line ratios for Hα/Hβ, H$_\gamma$/Hβ and Hδ/Hβ together with their corresponding C($H\beta$), EW$_e$ and EW$_a$. Finally, the value for the different parameters corresponding to the realisation that minimised the sum of the squared differences of the corrected lines ratios weighted by their errors from observation was taken. This was done by first evaluating a squared difference of the observed and the theoretical line ratios weighted by their errors for each of the the three lines. We present these three terms as:

$$H\alpha_{term} = (1/err_{\frac{H\alpha}{H\beta}}) \times ((\frac{H\alpha}{H\beta}) - (\frac{H\alpha}{H\beta})_{theory})^2, \tag{4.6}$$

$$H\gamma_{term} = (1/err_{\frac{H\gamma}{H\beta}}) \times ((\frac{H\gamma}{H\beta}) - (\frac{H\gamma}{H\beta})_{theory})^2, \tag{4.7}$$

$$H\delta_{term} = (1/err_{\frac{H\delta}{H\beta}}) \times ((\frac{H\delta}{H\beta}) - (\frac{H\delta}{H\beta})_{theory})^2. \tag{4.8}$$

where $1/err_{\frac{H\alpha}{H\beta}}$, $1/err_{\frac{H\gamma}{H\beta}}$ and $1/err_{\frac{H\delta}{H\beta}}$ are the errors of Hα, Hγ and Hδ with respect to Hβ respectively and all the terms with subscript "theory" are the theoretical ratios of the corresponding lines with Hβ.

After determining these three terms we minimized the sum of the three terms given as:

$$\triangle = H\alpha_{term} + H\gamma_{term} + H\delta_{term}$$

Unlike the hydrogen recombination lines, all the other emission lines being originated from the surrounding ionised gas, are unaffected by the underlying stellar absorption. As a result, all the emission lines except the hydrogen lines require only reddening correction.

Replacing the stellar absorption equivalent width (EW_a) with zero for the non-hydrogen lines, Equation 4.1 can reduced to:

$$\frac{I(\lambda)}{I(H\beta)} = \frac{F(\lambda)}{F(H\beta)} \exp\left[C(H\beta)f(\lambda)\right]. \tag{4.9}$$

With the value of C($H\beta$) being determined from the hydrogen lines, all the non-hydrogen observed flux ratio with Hβ were corrected for reddening effects.

4.5.6 The T_e(OIII) electron temperature and electron number density

Normally the different electron temperatures in HII regions can be established from forbidden line ratios (see the discussion in Chapter 1 section 1.7.2). The most common line ratio that has been used for determining the electron temperature is the I(4959+5007)/I(4363) ratio. Here, we used the approach by (Aller 1984) and (Kniazev et al. 2008) to relate these line ratios to [OIII] electron temperature, T_e(OIII). Electron temperatures for other species were then derived from photoionization models that relate T_e(OIII) to other temperatures (see 4.5.9).

The relation used in (Aller 1984) to determine T_e(OIII) is given as:

$$\frac{I(4959+5007)}{I(4363)} = C_T[\frac{1+a_1x}{1+a_2x}]10^{1.432/t}, \tag{4.10}$$

where $t = 10^{-4}T_e$(OIII), x=$10^{-4}N_e t^{-0.5}$

The parameters C_T, a_1 and a_2 are adopted from Kniazev et al. (2008) and presented below as:

$$C_T = 8.44 - 1.09t + 0.5t^2 - 0.08t^3, \tag{4.11}$$

$$a_1 = 2 \cdot 10^{-4} + 3.13 \cdot 10^{-4} - 1.6 \cdot 10{-}4t^2 + 2.67 \cdot 10^{-5}t^3, \tag{4.12}$$

$$a_2 = 0.0291 + 0.0253t - 0.0128t^2 + 0.00213t^3. \tag{4.13}$$

The electron number density, N_e, is normally calculated from the [SII]λ6717/λ6731 line ratio and it is found that the density for HII regions is very small, $N_e < 10^3$ cm^{-3} (Izotov et al. 2006). As a result the x term containing N_e in Equation 4.10 is often ignored. However, in our work, we have used a constant value of $N_e = 100$ cm^{-3}.

ESO 149-G003

Wavelength	$F(\lambda)/F(\mathrm{H}\beta)$	$I(\lambda)/I(\mathrm{H}\beta)$	EWe(Å)
3727[OII]	1.10±0.02	1.23±0.31	99.16±2.04
3869[NeIII]	0.21±0.01	0.24±0.06	13.09±0.50
4101(Hδ)	0.17±0.01	0.27±0.00	11.57±0.39
4340(Hγ)	0.36±0.01	0.45±0.01	23.03±0.43
4363[OIII]	0.04±0.01	0.06±0.02	2.70±0.45
4861(Hβ)	1.00±0.01	1.00±0.02	81.13±0.67
4959[OIII]	0.88±0.01	0.88±0.21	64.86±0.63
5007[OIII]	2.65±0.03	2.62±0.63	180.00±8.43
6548[NII]	0.03±0.01	0.03±0.02	2.90±0.77
6563(Hα)	3.41±0.03	2.86±0.02	269.00±0.67
6584[NII]	0.09±0.01	0.08±0.02	9.42±0.44

Table 4.5: The stellar absorption and reddening correction for the different lines detected in the galaxy ESO 149-G003. The stellar absorption correction is made only for the hydrogen recombination lines while the reddening is done for all the lines. All the lines are normalised to Hβ.

ESO 074-G015

Wavelength	$F(\lambda)/F(\mathrm{H}\beta)$	$I(\lambda)/I(\mathrm{H}\beta)$	EWe(Å)
3727[OII]	2.59±0.05	2.59±0.05	76.84±1.38
3869[NeIII]	0.66±0.02	0.66±0.02	12.80±0.38
4101(Hδ)	0.25±0.01	0.25±0.00	8.23±0.18
4340(Hγ)	0.44±0.01	0.44±0.00	9.27±0.16
4363[OIII]	0.10±0.01	0.10±0.01	2.08±0.16
4861(Hβ)	1.00±0.01	1.00±0.01	23.68±0.16
4959[OIII]	1.50±0.01	1.50±0.01	30.94±0.20
5007[OIII]	4.62±0.04	4.62±0.04	95.08±0.31
6548[NII]	0.04±0.00	0.04±0.00	1.16±0.05
6563(Hα)	2.57±0.02	2.57±0.12	68.98±0.20
6584[NII]	0.24±0.00	0.24±0.00	6.73±0.09

Table 4.6: The stellar absorption and reddening correction for the different lines detected in the galaxy ESO 074-G015. The stellar absorption correction is made only for the hydrogen recombination lines while the reddening is done for all the lines. All the lines are normalised to Hβ.

ESO 272-G025

Wavelength	$F(\lambda)/F(\mathrm{H}\beta)$	$I(\lambda)/I(\mathrm{H}\beta)$	EWe(Å)
3727[OII]	1.77±0.05	2.26±0.17	68.85±1.76
3869[NeIII]	0.32±0.02	0.39±0.04	8.69±0.52
4101(Hδ)	0.24±0.02	0.29±0.01	7.77±0.58
4340(Hγ)	0.37±0.01	0.41±0.01	9.65±0.25
4363[OIII]	0.05±0.01	0.05±0.01	1.32±0.30
4861(Hβ)	1.00±0.02	1.00±0.02	20.50±0.21
4959[OIII]	0.93±0.017	0.92±0.06	19.15±0.27
5007[OIII]	3.22±0.04	3.15±0.19	65.53±0.40
6548[NII]	0.12±0.01	0.09±0.01	1.59±0.10
6563(Hα)	3.71±0.05	2.85±0.01	52.41±0.24
6584[NII]	0.29±0.013	0.22±0.02	4.24±0.19

Table 4.7: The stellar absorption and reddening correction for the different lines detected in the galaxy ESO 272-G025. The stellar absorption correction is made only for the hydrogen recombination lines while the reddening is done for all the lines. All the lines are normalised to Hβ.

4.5.7 Solving all the parameters iteratively

We finally carried out all the steps in Sections 4.5.5 and 4.5.6 together to solve for all the parameters, i.e. the corrected intrinsic line ratios (I(λ)/I($H\beta$)) of all the lines, their corresponding emission equivalent width EW$_e$, C(Hβ) and T$_e$(OIII) in an iterative process. The iteration process went on until $\frac{I(4959+5007)}{4363}$ calculated from Equation 4.10 was close to the ratio from the corrected line ratio. The iteration process includes error estimations.

The errors in the reddening corrected emission lines and EW_e are derived from a Monte-Carlo simulation that has run based on the initial observed emission lines with their corresponding errors from the observation. The Monte-Carlo simulation was conducted for each single realisation of the iteration process.

The measured intensities, reddening corrected intensities and the corresponding emission equivalent widths are presented in the Tables 4.5, 4.6 and 4.7 for ESO 149-G003, ESO 074-G015, ESO 272-G025 respectively.

4.5.8 Abundance determinations

We used the direct method of abundance determination based on relationships derived by Izotov et al. (2006) using photoionization models. Since the relationships are electron temperature dependent, we first determined the electron temperatures that we needed.

4.5.9 T_e(OII) Electron temperatures

Normally, the temperature throughout HII regions is not uniform (Stasińska 1990) because of the different levels of ionization in the different regions. Since the determination of abundance is a strong function of the electron temperature, it is very important to take the variation of temperature within the HII regions into account when calculating the abundance.

Different models predict the electron temperature of the ionized gas with the assumption of different level of ionization zones. Some models divide the entire HII region into two ionization zones: high and low ionization zones (Stasińska 1990) and others into three with the addition of an intermediate ionization zone (Stasińska & Izotov 2003). The advantage of the latter is that it minimises the mixture of the intermediate ionization zones either with the high or with the low ionization zone and gives a refined method of determining the abundance.

This particular work adopted a three level ionization model originally developed by Stasińska (1990) and later recomputed by Izotov et al. (2006) with the most recent atomic coefficients for line emissivities on appropriate series of photoionization models for the ionization correction factor. However, the difference between the old and new approach is very minimal; in most cases the difference is even less than 1%.

Based on this model, Izotov et al. (2006) have derived a relationship between T_e(OIII) and temperatures of different ions in sequences of photoionization models that match with the observed emission lines in HII galaxies. According to this photoionization model, the temperature of the different ions in HII regions is related to other ions in different ways and the dependence is a function of the level of ionization of the system.

The relationship established between T_e(OIII) and T_e(OII), based on this photoionization model is shown in panel a) while the relationship between T_e(OIII) and T_e(SII) is shown in panel b) of Figure 4.9 in solid lines in both cases. The relations are defined for different metallicity regions that are defined as: high metallicity ("high Z"), intermediate metallicity ("intermediate Z") and low metallicity ("low Z") regions. Each have a metallicity, 12+log(O/H), of approximately 7.2, 7.6 and 8.2 respectively.

Izotov et al. (2006) gave empirical relationship between T_e(OIII) and T_e(OII) at the different metallicity regions defined below as:

$$t(OII) = -0.577 + t \times (2.065 - 0.498t), \text{low Z}, \quad (4.14)$$

$$= -0.744 + t \times (2.338 - 0.610t), \text{intermediate Z}, \quad (4.15)$$

$$= 2.967 + t \times (-4.797 + 2.827t), \text{high Z} \quad (4.16)$$

where t(OII)=$10^{-4}$$T_e$(OII) and t=$10^{-4}$$T_e$(OIII)

When it comes to our work, T_e(OII) was calculated in all the three metallicity regions and the corresponding metallicity was calculated (see below how the metallicities are calculated) and

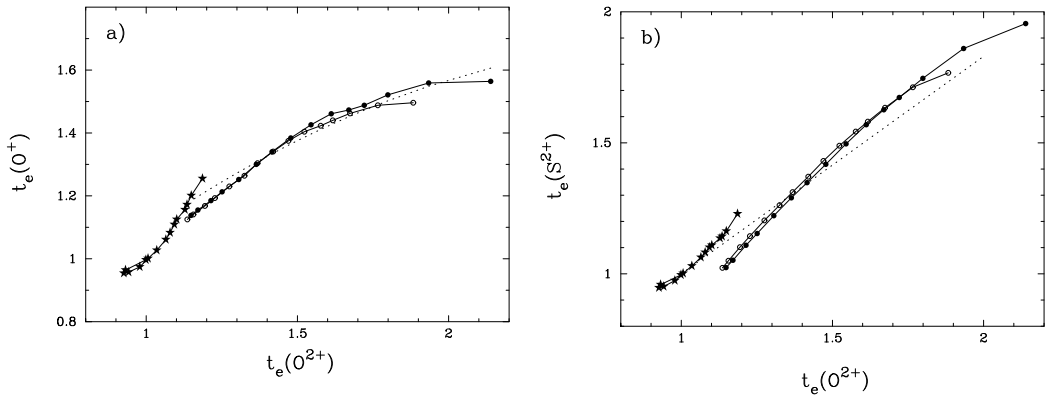

Figure 4.9: Relations between the electron temperature a) t_e(OII) and t_e(OIII) ($t_e = 10^{-4}T_e$) and b) $t_e(SIII)$ and $t_e(OIII)$ obtained from the sequences of photoionization models for HII galaxies (Stasińska & Izotov 2003) using stellar atmosphere models from Smith et al. (2002). Filled circles are for the model with Z=0.02Z$_\odot$ (low metallicity zone), open circles are for the models with Z=0.05Z$_\odot$ (intermediate metallicity models), and stars are for the model with Z=0.2Z$_\odot$(high metallicity zone), where Z$_\odot$ is solar metallicity. The dotted lines are the approximation of the models of Stasińska (1990) in a) and the approximation of the models of Garnett (1992) in b).

checked to establish if it matched with the metallicity regime. In all the three galaxies, the metallicity regimes were found finally to be the intermediate ones (see the values of log (O/H + 12) in the results, Tables 4.8, 4.9 and 4.10).

4.5.10 Ionic abundances of O, N and Ne

Based on the ionization level of the different species at the different ionization zones in the HII regions, according to Izotov et al. (2006), T$_e$(OII) represents the temperature of a region where N^+ reside while T$_e$(OIII) represents the temperature of a region where Ne^{2+} ions reside. We have adopted empirical expression from Izotov et al. (2006) and used these for ionic abundance calculations. The empirical expressions only for the specific ions we are interested in are presented below:

$$12 + \log O^+/H^+ = \log\frac{\lambda 3727}{H\beta} + 5.961 + \frac{1.676}{t} - 0.4\log t - 0.034t + \log(1 + 1.35x) \qquad (4.17)$$

where $t = 10^{-4}$T$_e$(OII)

$$12 + \log O^{2+}/H^+ = \log\frac{\lambda 3727 + \lambda 5007}{H\beta} + 6.200 + \frac{1.251}{t} - 0.55\log t - 0.014t \qquad (4.18)$$

where $t = 10^{-4}\mathrm{T}_e(\mathrm{OIII})$

$$12 + \log N^+/H^+ = \log\frac{\lambda6548 + \lambda6584}{6.234} + \frac{0.950}{t} - 0.42\log t - 0.027t + \log(1 + 0.116x) \quad (4.19)$$

where $t = 10^{-4}\mathrm{T}_e(\mathrm{OII})$

$$12 + \log Ne^{2+}/H^+ = \log\frac{\lambda3869}{H\beta} + 6.444 + \frac{1.606}{t} - 0.42\log t - 0.009t \quad (4.20)$$

where $t = 10^{-4}\mathrm{T}_e(\mathrm{OIII})$

As can be seen here, the ionic abundances are strong functions of their corresponding temperatures. We thus used the different temperatures (T_e(OIII) and T_e(OII)) calculated above to calculate the different ionic abundances. The errors in each of the ionic abundances were propagated from the different emission line errors that are involved in the calculations.

4.5.11 Elemental abundances of O, N and Ne

Normally the elemental abundance for each elements is derived by summing the different ionic abundances of each of the species seen in the optical spectra by accounting for the unseen species using the ionization correction factor (ICF). The total abundance of an element A, for example, is thus given in terms of ICF and its observed ions as:

$$\frac{A}{H} = ICF(A)\frac{A^{+i}}{H^+}, \quad (4.21)$$

where ICF(A) is the ionization correction factor and A^{+i} is the A^i ion of the element A.

According to the photoionization model this work is based on and depending on the metallicity of the HII regions, three ionization factors for each species are possible. We present below the relations the ionization correction factors for N and Ne in the three different metallicity regimes adopted from Izotov et al. (2006).

$$ICF(N^+) = -0.825v + 0.718 + 0.853/v, \text{low Z}, \quad (4.22)$$
$$= -0.809v + 0.712 + 0.852/v, \text{intermediate Z}, \quad (4.23)$$
$$= -1.476v + 1.752 + 0.688/v, \text{high Z} \quad (4.24)$$

$$ICF(Ne^+) = -0.385w + 1.365 + 0.022/w, \text{low Z}, \quad (4.25)$$
$$= -0.405w + 1.382 + 0.021/w, \text{intermediate Z}, \quad (4.26)$$
$$= -0.591w + 0.927 + 0.546/w, \text{high Z}, \quad (4.27)$$

where $v = O^+/(O^+ + O^{2+})$ and $w = O^{2+}/(O^+ + O^{2+})$.

As the metallicity regime of all the three HII regions of our sample is intermediate, we used the ionization correction factor that corresponds to the intermediate regime to determine the elemental abundance of N and Ne.

The elemental abundance of oxygen must normally be determined from the sum of all the three oxygen ions, O^{+}, O^{2+} and O^{3+}. However, if HeII λ4686 line is absent or weak in the HII region spectra, then one can neglect the contribution from O^{3+} ion to the total oxygen abundance (Izotov et al. 2006). Unfortunately, the HeII λ4686 line in our spectra falls in the boundary between the first two CCDs of RSS and as a result we could not check the strength of this line. Though we could not see HeII λ4686 in our spectra, since we could not also see any sign of O^{3+}, our oxygen abundance determination assumed no contribution from O^{3+} ion. The oxygen abundance is thus given as:

$$\frac{O}{H} = \frac{O^{+} + O^{2+}}{H^{+}}. \tag{4.28}$$

In the Tables 4.8, 4.9 and 4.10, we present the T_e(OIII), T_e(OII), the different ionic and elemental abundances of O, N and Ne, C(Hβ) as well as the EW(abs) for all the three galaxies. The errors in each of the elemental abundances and T_e(OII) are propagated from errors of the different emission lines and ionic abundances used to derive them. On the other hand the errors in T_e(OIII), C(Hβ) are derived from a Monte-Carlo simulation as it was explained in Section 4.5.7.

ESO 149-G003	
T_e(O III)(K)	14100 ± 5568
T_e(O II)(K)	13398 ± 3228
O^+/H^+ ($\times 10^5$)	1.624 ± 0.422
$12 + \log(O^+/H^+)$	7.211 ± 0.113
O^{++}/H^+ ($\times 10^5$)	3.381 ± 0.662
$12 + \log(O^{++}/H^+)$	7.529 ± 0.085
O/H ($\times 10^5$)	5.005 ± 0.785
$12 + \log$(O/H)	7.699 ± 0.068
N^+/H^+ ($\times 10^5$)	0.076 ± 0.019
$12 + \log(N^+/H^+)$	5.879 ± 0.108
ICF(N^+/H^+)	3.745
N/H ($\times 10^5$)	0.284 ± 0.085
$12 + \log$(N/H)	6.453 ± 0.131
log(N/O)	-1.247±0.139
Ne^{++}/H^+ ($\times 10^5$)	0.753 ± 0.209
$12 + \log(Ne^{++}/H^+)$	6.877 ± 0.120
ICF(Ne^{++}/H^+)	1.14
Ne/H ($\times 10^5$)	0.858 ± 0.239
$12 + \log$(Ne/H)	6.934 ± 0.121
log(Ne/O)	-0.766±0.130
$C(H\beta)$	0.16 ± 0.10
EW(abs)(Å)	7.0 ± 1.20

Table 4.8: The different electron temperatures (T_e(OIII) and T_e(OII)) as well as the ionic and elemental abundances for O, N, and Ne are calculated for the galaxy ESO 149-G003. All the abundances are calculated using the direct method of abundance determination.

ESO 074-G015	
T_e(O III)(K)	15900±640
T_e(O II)(K)	14313±230
O^+/H^+ ($\times10^5$)	2.748±0.053
12 + log(O^+/H^+)	7.439±0.008
O^{++}/H^+ ($\times10^5$)	4.371±0.027
12 + log(O^{++}/H^+)	7.641±0.003
O/H ($\times10^5$)	7.119±0.059
12 + log(O/H)	7.852±0.004
N^+/H^+ ($\times10^5$)	0.177±0.003
12 + log(N^+/H^+)	6.247±0.006
ICF(N^+/H^+)	3.277
N/H ($\times10^5$)	0.578±0.010
12 + log(N/H)	6.762±0.008
log(N/O)	-1.090±0.008
Ne^{++}/H^+ ($\times10^5$)	1.488±0.045
12 + log(Ne^{++}/H^+)	7.173±0.013
ICF(Ne^{++}/H^+)	1.168
Ne/H ($\times10^5$)	1.737±0.053
12 + log(Ne/H)	7.240±0.013
log(Ne/O)	-0.613±0.014
$C(H\beta)$	0.0±0.000
EW(abs)(Å)	0.0±0.000

Table 4.9: The different electron temperatures (T_e(OIII) and T_e(OII)) as well as the ionic and elemental abundances for O, N, and Ne are calculated for the galaxy ESO 074-G015. All the abundances are calculated using the direct method of abundance determination.

ESO 272-G025	
T_e(O III)(K)	14200±2047
T_e(O II)(K)	13459±1161
O^+/H^+ ($\times 10^5$)	2.943±0.217
12 + log(O^+/H^+)	7.469±0.032
O^{++}/H^+ ($\times 10^5$)	3.866±0.186
12 + log(O^{++}/H^+)	7.587±0.021
O/H ($\times 10^5$)	6.809±0.286
12 + log(O/H)	7.833±0.018
N^+/H^+ ($\times 10^5$)	0.221±0.016
12 + log(N^+/H^+)	6.345±0.032
ICF(N^+/H^+)	3.004
N/H ($\times 10^5$)	0.665±0.055
12 + log(N/H)	6.823±0.036
log(N/O)	-1.010±0.041
Ne^{++}/H^+ ($\times 10^5$)	1.216±0.130
12 + log(Ne^{++}/H^+)	7.085±0.046
ICF(Ne^{++}/H^+)	1.189
Ne/H ($\times 10^5$)	1.446±0.155
12 + log(Ne/H)	7.160±0.047
log(Ne/O)	-0.673±0.050
$C(H\beta)$	0.34±0.02
EW(abs)(Å)	0.3±0.2

Table 4.10: The different electron temperatures (T_e(OIII) and T_e(OII) as well as the ionic and elemental abundances for O, N, and Ne are calculated for the galaxy ESO 272-G025. All the abundances are calculated using the direct method of abundance determination.

4.6 Results

The different parameters measured for the three galaxies are presented in the three tables in the above Section. In Table 4.5, 4.6 and 4.7, we presented the different measured line fluxes ratios relative to Hβ, $F(\lambda)/F(\beta)$, the reddening corrected line intensities, $I(\lambda)/I(\beta)$, and as well as the emission equivalent widths. In Tables 4.8, 4.9 and 4.10, we list O/H, N/H, Ne/H, T_e(OIII), T_e(OII), C(Hβ), EW(abs) and ICF. All the galaxies have oxygen abundance (12+log(O/H)) below 8.0 dex which is normally considered to be a low metallicity value. Given the metal-poor nature of dwarf irregulars, this metallicity seems reasonable and agrees with different previous results (e.g. Kunth & Östlin 2000). N/H, Ne/H, T_e(OIII), T_e(OII) values we have found are also in reasonable agreement with values found in the literature for dIrr galaxies (e.g. Croxall et al. 2009).

4.6.1 The metallicity-luminosity relationship

In this Section we compared how well the three galaxies fit to an already established metallicity-luminosity relationship for other dIrr galaxies from the work by Lee et al. (2007). Figure 4.10 shows a metallicity-luminosity relationship for the galaxies, where the luminosity is represented by their B-band absolute magnitude. The data includes mainly dIrr galaxies from the Centaurus A group (cen A) and Sculptor group (Scl) and some from different literature (see the detail discussion in Lee et al. 2007). The thick unfilled black points in the figure represent our three galaxies.

It is noted from Figure 4.10 that the usual metallicity-luminosity trend exists though there is quite a bit of scatter in the relationships for both the Cen A and Scl group galaxies. This result comes because some of the metallicities are not calculated using the direct method (see the unfilled squares and triangles). On the other hand, both for the Cen A and Scl groups whose metallicities are calculated using the direct method, their values seem to agree within the 0.1 dex sigma value to the best fit (see the filled points).

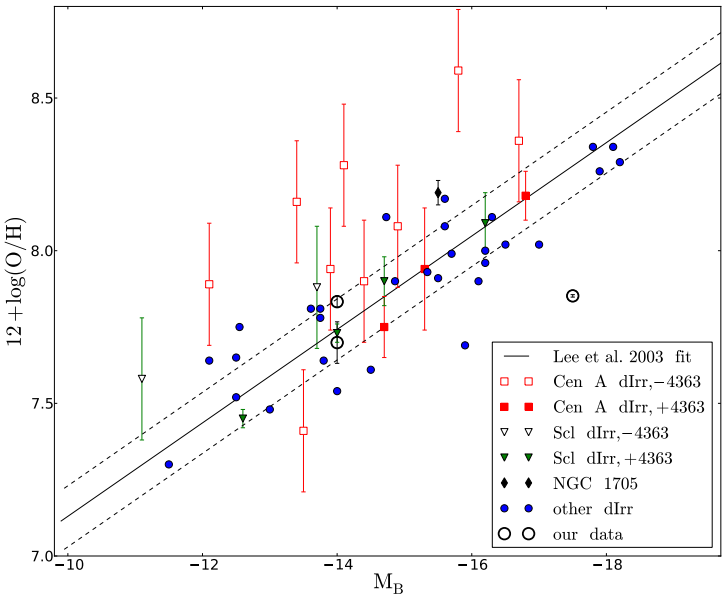

Figure 4.10: B-band luminosity–metallicity relation for dwarf irregular galaxies. The squares and triangles mark locations of Cen A and Scl dwarf galaxies respectively. Filled triangles and squares represent metallicity calculated from bright line method while the unfilled triangles and squares are calculated using the direct method of abundance calculation. Small circles indicate nearby dwarf irregular galaxies in the Local Volume. [OIII] λ4363 detections are shown as filled symbols. The diamond marks the location of the nearby dwarf starburst galaxy NGC1705. The solid line is a fit to a sample of nearby dwarf irregulars described in Lee et al. 2003. We note that Cen A and Scl group dwarfs with [OIII] λ4363 abundances are within 0.1 dex (dotted lines) of the fit (a detailed description of the individual samples used to produce this plot is found in Lee et al. (2007)). The three thick unfilled circles are our sample.

As can be seen in the plot (Figure 4.10), our two galaxies (ESO 149-G003 and ESO 272-G025) fall well within the one sigma error limit of the best fit for dIrr galaxies whose metallicities are calculated with the direct method of abundance determination. The third galaxy (ESO 074-G015), however, shows deviation from the usual trend for dIrr galaxies' metallicity-luminosity relationship considered for comparison.

Assuming that the dIrr nature and the magnitude of third galaxy are true, it should have a metallicity of about ~ 8.2 according to the trend in Figure 4.10. Given its magnitude (and hence mass), this galaxy should have much more resistance to anything that would drive out its metals. Hence, it appears, that for some reason, the metal production in the galaxy is not that efficient or possibly some kind of unusually strong feedback mechanism (AGN, stellar or supernova) or some other environmental factor drives out the metals very efficiently. Whatever the case is, this particular galaxy seems to have a different metallicity, and hence star formation history, than the usually known trend for dIrr galaxies.

The other possibility could be that its magnitude was measured wrongly perhaps because of uncertainties in its distance. If that is so, it should have a M_B of about 3.5 magnitude brighter (~ -15) than what it is normally calculated (~ -17.5) based on information from the literature (Kaisin et al. 2007) in order to fit to the normal metallicity-luminosity for dIrr. Given the unavailability of additional distance measurements for its distance, it is difficult to cross check the magnitude we calculated.

4.6.2 The metallicity gradient of ESO 074-G015

It is known that the metallicity of disk galaxies declines with radius, i.e., there is more efficient interstellar material processing (production of heavy elements or metals) in the centre than in outer regions (Searle 1971, Magrini et al. 2010, Bresolin et al. 2009). The reason for this could be that there is progressively less gas available as one goes out from the centre (non-uniform distribution of raw material) or alternatively, the efficiency of turning gas into stars (the star formation mechanism) is not uniform throughout the disk. Different classes of disk galaxies show different gradient rates. For example, the metallicity of M101 and M33 which are typical spiral galaxies decline by a factor of 10 at the outer region as compared to the case at nuclear region (Denicoló et al. 2002, Osterbrock 1989).

Despite their somewhat disky nature, irregular galaxies, on the other hand, seem to have weak spatial gradients of metallicity (Kobulnicky et al. 1999). This can be partly because of the presence of high level of mixing in their interstellar medium for different reasons. Their self-regulated star formation mechanism (which was discussed in Chapter 1 Section 1.7.1) mixes up the processed and the unprocessed pristine material as the star formation propagates throughout the galaxy.

In this Section we will calculate the metallicity gradient for the galaxy ESO 074-G015. This galaxy has an edge-on orientation in the sky (see the left top panel of Fig. 4.1) and has

extended HII regions. This orientation gives us access to the different emission lines originating from nearly all parts of the galaxy to the extent that it would be difficult to identify their actual spatial origin inside the galaxy.

In Figure 4.11, we show the 2-dimensional spectrum of this galaxy. One can note that the [OIII]λ4363 line is observed only within 0.5 kpc of the centre and on the other hand Hα, Hβ, [OII]λ3727, [OIII]λ4959 and [OIII]λ5007 are visible almost throughout the galaxy.

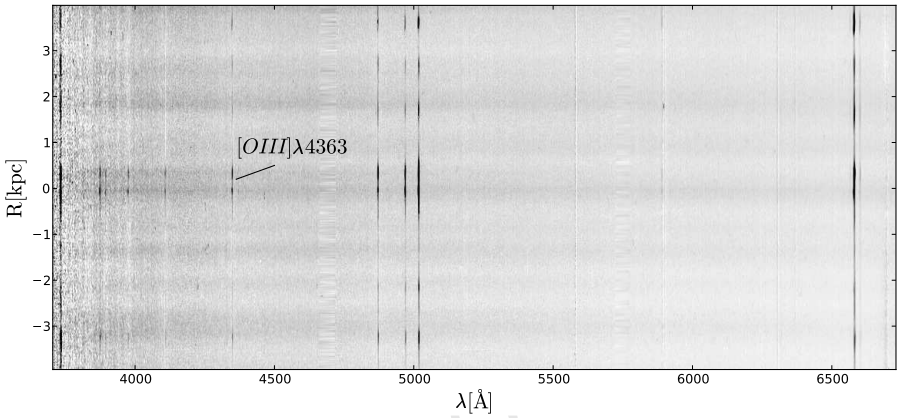

Figure 4.11: The 2-dimensional spectrum of the galaxy ESO 074-G015. The galaxy is edge-on and has very extended HII regions, while [OIII]λ4363 is seen only at the centre.

At the centre of the galaxy, it is possible to employ the direct method of metallicity determination because [OIII]λ4363 line is detectable and hence we adopted the metallicity determined in Table 4.9 using the direct method. However, at the other parts, where [OIII]λ4363 is not detectable, we have to rely on other methods of metallicity determination. In this particular case, we employed the R_{23} method which is discussed briefly in Chapter 1, Section 1.7.2 (see Yin et al. (2007) for a detailed discussion of the method). The approach is based on the ratios of the strong optical lines [OII]λ3727, [OIII]$\lambda\lambda$4959, 5007 and is given as

$$R_{23} = ([OII]\lambda 3727 + [OIII]\lambda\lambda 4959, 5007)/H\beta. \tag{4.29}$$

The method is double valued (two metallicities for a single R_{23} ratio). The double values are generally categorised as low (12 + log (O/H) $<$ 7.9) and high metallicity (12+log(O/H)$>$8) branches.

We have extracted eight spectra at various distances from the centre and calculated 12+log(O/H). At the central region of the galaxy, where [OIII]λ4363 line is observed, an oxygen abundance of 12+log(O/H)=7.8 is determined using the direct method. Even if this metallicity is normally an intermediate metallicity according to the three ionization zones, it is the maximum metallicity

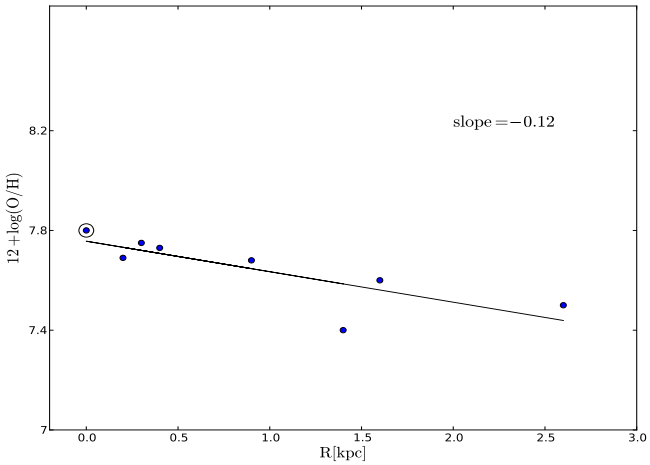

Figure 4.12: The metallicity gradient of ESO 074-G015. Metallicity is calculated using the R_{23} method throughout except at the centre where the direct method is used (this point is indicated by the dot inside the circle).

of the low metallicity branch of the R_{23} method.

For the above reason, in the regions where [OIII]λ4363 is not seen (throughout the galaxy except at the centre), we used the lower metallicity branch of R_{23} and calculated the metallicities using the lower branch R_{23} relation seen in Equation 4.30 below and adopted from Yin et al. (2007):

$$12 + \log(O/H) = 6.486 + 1.401 \times \log(R_{23}), \tag{4.30}$$

where $\log(R_{23})$ is the the ratio defined in Equation 4.29.

The result found is in fact within the lower branch metallicity regime and all are below the metallicity found at the centre. In Figure 4.12, we present the metallicity-radius correlation found. The result shows there is a metallicity gradient with a slope of -0.12 dex/ kpc. Note that in this Figure we combine the results from two different methods (direct method in the central point and the R_{23} method for the rest of the galaxy). This does not affect the main result presented here, namely the existence of a strong gradient.

As it is mentioned in Section 4.3, the galaxy ESO 074-G015 has an edge-on orientation. An edge-on orientation is not the ideal orientation to study the spatial distribution of physical properties such as metallicities in disky galaxies for two main reasons. The first reason is, if the galaxy has a physically and optically thick disk, the calculated metallicity suffers severely from dust extinction since whatever light emitted should travel in the plane of the disk before

it makes it to the outside of the galaxy. As a result, the emerging light does not necessarily reflect the reality. However, we found that the reddening coefficient ($C(H\beta)$) for this galaxy is zero. This galaxy then seems to have an optically thin disk at least at the HII regions observed; consequently, the metallicity calculation is not affected by extinction. Alternatively, in principle it could be possible that we only see the edge og the galaxy either due to extreme optical depth inside, or just the spatial distribution of HII regions. However, in this case, we should not expect to see any gradient because essentially all the light are coming from the extreme edges of the galaxy. Since we see a gradient, we rule out this possibility and it is highly likely that we are seeing through the disk and indeed the extinction is very low (C($H\beta$)=0).

Now that it is very likely that we see through the disk, it seems that light contamination within the galaxy itself is an unavoidable problem. Since the orientation of the disk is edge-on, the emission coming from the centre (R=0) is contaminated by background and foreground light from different part of the disk. However, as one goes out from the centre perpendicular to the line of sight direction, the contamination gets less and less and finally at the maximum radius, the emission is no longer contaminated. Our calculation of metallicity for this galaxy so far did not consider this contamination effect and the result found in Figure 4.12 might be different in reality. In fact, if the background and foreground contaminations are corrected, all the metallicities found might increase by a certain amount. Since the effect is radius dependent, any correction that needs to be made in order to account for the contamination is less as one goes out from the centre. Though it is not clear how much the exact correction at a given radius could be, it is possible to find a gradient more than the one we found without correction.

The metallicity gradient found indicates that star formation rate is not uniform throughout the galaxy. It might then be possible to conclude that the gas concentration is higher as one approaches the centre of the galaxy assuming equally efficient star formation mechanism throughout the galaxy. When the molecular gas concentration drops with radius and as the gas gets consumed, the minimum threshold amount of gas that is needed to keep the star formation going starts to finish first at the outskirts and then progressively closer to the centre. As this happens, the star formation gets weaker and weaker with radius and it is possible to see a gradient in the metallicity.

Observationally, it has been found that almost all dIrr have very modest or no abundance gradient. However, NGC 6822 has been presented as a case of a dIrr galaxy with a strong gradient of -0.16±0.05 dex kpc^{-1} (Lee et al. 2006). When the measured abundance gradient of ESO 074-G015 found in this work is compared with the value for NGC 6822, the difference is only about 0.02 dex kpc^{-1} and this means these two dIrr galaxies seem to have a similar gradient, if not exactly the same. On the other hand, when the gradient of ESO 074-G015 is compared to values observed for spiral galaxies, the value is quite high (e.g. Martin & Roy 1992, Cedrés et al. 2004, Magrini et al. 2010). The abundance gradient observed for M33 by Magrini et al. (2010) for example is -0.037 ± 0.009 dex kpc^{-1} in the entire radial range of up to 8 kpc, and -0.044 ± 0.009 dex kpc^{-1} excluding the value at the central part. This result together with

the result found for NGC 6822 highlights the fact that the previous general assumption that dIrrs have no gradients seems not be clear at all, and requires further data and investigation.

With its strong abundance gradient found in this work, ESO 074-G015 seems to be the second dIrr discovered so far with a strong abundance gradient. ESO 074-G015 and NGC 6822 could be a good laboratory to understand the mixing process in the ISM of dIrr galaxies that lead to abundance gradients (or the lack thereof). As it is explained in Chapter 1, the ISM of dIrr galaxies is often chaotic, and as a result, metals produced at one episode of SF at a given part of the galaxy would be distributed uniformly throughout the galaxy over a couple of hundreds Myrs (Kunth & Östlin 2000, Kobulnicky et al. 1999, references therein). Hence, dIrr are believed to be devoid of any abundance inhomogeneity. However, if any inhomogeneity is observed in dIrr, it may be because the mixing process is not strong or fast enough to smooth out the metallicity variations for various reasons. The gradient found in ESO 074-G015 could hence be due to a scenario where the mixing processes was not strong enough to wipe out the spatial variation.

Another possible explanation for the existence of such unusual gradient in dIrrs like ESO 074-G015 would be the dominance of its disky nature. ESO 074-G015 is reported to have a well established disk that makes it classified as an Sd galaxy in (Kaisin et al. 2007). It could be possible that the same physical mechanism driving abundance gradients in disky galaxies is driving the abundance gradient in ESO 074-G015. However, this assertion does not seem to be in agreement with the case of NGC 6822 where there is no sign of disk dominance.

4.7 Conclusions and summary

This chapter determined the elemental and ionic abundance, electron temperature and the extinction coefficients of three isolated dwarf irregular galaxies which are part of pilot project. This pilot project examined the capabilities of the long-slit spectroscopic mode of the Robert Stobie Spectrograph (RSS) on the Southern African Large Telescope for a larger future project on the study of the spectroscopic properties (such as star formation and chemical evolution) of a large sample of Southern dwarf galaxies and other star forming galaxies in order to understand better star formation and chemical evolution in different types of galaxies at different environments. The data were taken during the performance verification and commissioning phases of SALT.

Our first result shows that two of the three galaxies follow the metallicity-luminosity relationship known for dwarf irregular galaxies. We have compared where these galaxies lie in a metallicity-luminosity relationship established for dwarf irregular galaxies and their metallicity is found comparable to their B-band absolute magnitude. However, the third galaxy (ESO 074-G015) seems to deviate from this relationship. However this difference could be a result of uncertain distance calculations.

We investigated whether there is a metallicity gradient in the third galaxy for which extended HII regions are visible. The metallicity determination used the direct method at the centre

because the emission line [OIII]λ4363 is strong while at the other parts the R_{23} method is used because the line [OIII]λ4363 is not detectable. Indeed we have found a metallicity gradient with a slope of -0.12 dex/ kpc.

Overall, given the RSS throughput shortfall problem at the time of observations, our results are very encouraging for carrying out a larger scale future study on the spectroscopic properties of dwarf star forming galaxies and other star forming galaxies using the long-slit capabilities of SALT. The result from this pilot project will be incorporated in the future large sample study in trying to understand the bigger picture of star formation and chemical evolution of the these galaxies as a function of environment.

Currently all the major problems including the throughput issue in the RSS are fixed and SALT is expected to be starting commissioning phase observations very soon again. When the telescope is fully functional, it is believed that it will produce much better quality data than what was used here in this work.

5

Conclusions and summary

Though both Luminous Infrared Galaxies (LIRGs) and dwarf irregular galaxies (dIrr) are star forming galaxies, they represent the extremes of star formation rate among the family of star forming galaxies. LIRGs often form their stars through interaction and mergers whereas the star formation mechanisms in dIrr is not always obvious. Both environmental factors as well as self regulated stochastic star formation mechanisms are suggested as possible mechanisms. These galaxies have different significance for various astronomical processes in the Universe. The importance of LIRGs ranges from their implications for the understanding of the cosmic star formation history to the growth of black holes and nuclear activity in galaxies. On the other hand, dIrr are important for understanding the general chemical enrichment and mass assembly history of the Universe, for example. Motivated by the afore-mentioned, and, other reasons, these two types of galaxies have been the subject of many studies. Though most issues regarding their formation and evolution are still far from conclusion, a number of milestones and encouraging steps have been achieved. This work investigated the star formation-density relationship of local LIRGs and the abundances of three Local Volume dIrr. We used various redshift surveys for the former and spectroscopic data from the Southern African Large Telescope (SALT) for the later.

5.1 The relationship between star formation rate and environment of local LIRGs and dark matter haloes and LIRGs

We have studied the environments of local LIRGs in comparison to other types of local and high redshift galaxies in order to understand the nature of their star formation, and their possible origin and evolution. Both the LIRG and non-LIRG IR galaxies are drawn from IRAS catalogs. The local environment is quantified using the number counts of PSCz and 6dF galaxies in a cylinder of $2h^{-1}$ Mpc radius and $10h^{-1}$ Mpc length.

The most important result of this work revealed that the IR luminosity value $L_{IR} \sim 10^{11}h^{-2}L_{\odot}$ is an important luminosity point among IR galaxies. There is a dramatic density rise above $L_{IR} = 10^{11}h^{-2}L_{\odot}$ (LIRGs) while IR galaxies below this luminosity point (non-LIRG IR galaxies) have a local density equal to the mean galaxy density in the universe. The environment found for both populations is consistent with their respective dominant form of star formation mechanism found in previous studies (Sanders & Mirabel 1996). In the case of LIRGs, their star formation is often the result of mergers and interaction which is a common phenomenon in dense environments such as group and clusters.

The local density around LIRGs is not only higher than the environment around non-LIRG IR galaxies, but it is also found to be monotonically proportional with their L_{IR} output (which we used as a measure of star formation). Even if this study could not cover the entire ULIRG luminosity range because of lack of data, it was shown that the relationship between L_{IR} and density continues in the same manner until low L_{IR} ULIRGs. The non-LIRG IR galaxies, LIRGs, and low L_{IR} ULIRGs live in fields (or near the transition between group and field environments), groups, and cluster environments respectively. The non-LIRG IR galaxies do not only live in less dense environments than LIRGs, but they also experience a flat L_{IR}-density trend.

We found that, at a constant stellar mass, SFR of LIRGs is correlated with their local density. On the other hand, at constant SFR value, no trend is observed between stellar mass and density. In addition, it is found that IR-galaxies seem to require a certain minimum stellar mass at a given SFR (or L_{IR}) for their existence and this stellar mass limit is linearly correlated with L_{IR}. Once the minimum stellar mass limit is met and they become LIRGs, any additional mass they acquire does not seem to have any effect on their star formation rate. To form stars at a higher rate, their environment must become denser.

LIRGs are found to be similar in their star formation-density relationships with $z \sim 1$ blue cloud galaxies, as witnessed by some studies. We also noted a similarity in the origin of the SFR-density relationship of LIRGs and $z \sim 1$ blue cloud galaxies. The origin in both cases appears to arise from the relationship between stellar mass and density. These similarities suggest that the formation mechanism of local LIRGs and $z \sim 1$ blue galaxies might be similar. The two populations may have formed via similar processes but at different times. Alternatively, local LIRGs might be survivors of whatever process transformed $z \sim 1$ blue cloud galaxies into the present red sequence galaxies.

We also studied the star-formation density connection of LIRGs by quantifying their local environment using their dark matter halo. Volume-limited samples from the 2MASS redshift survey (2MRS) are used to identify galaxy groups/clusters and then the low L_{IR} volume-limited LIRG sample is cross correlated to the identified groups/clusters to find what environments the LIRGs live in, and draw correlations with their star formation.

The result turned out not to be too far from what we found using number count of galaxies to quantify local environment. A comparison made between the probability of finding LIRGs and 2MASS galaxies at a given halo mass size revealed that the relative probability of finding LIRGs both in cluster and field environment is very minimal. The highest relative probability appears to be at a halo mass near the transition between field and group, though the error bars are not insignificant. Given the L_{IR} distribution of our sample (mostly low-L_{IR} LIRGs) and the correlation found between the environments of LIRGs and their corresponding L_{IR} values, the result seems consistent both with the level of SF and the already known effective SF mechanism for LIRGs.

We now know that the low-L_{IR} LIRGs prefer a low mass group environment. However, it is not clear where exactly they live inside these group environments, outskirts or at the centre. Depending on where exactly they live in their environment, the star formation mechanism could be different. We found that, on average, these galaxies live within $0.5R_{vir}$ radius of the centre of the galaxy system they are associated with. Moreover, it is found that LIRGs that live close to the centre form stars at a higher rate than those that are far out from the centre. This result is in agreement with the star formation-environment correlation in a group size environments in the local Universe. Unlike the case in cluster environments, processes such as interaction and mergers are more effective close to the centre of group size environments than at the outskirts. It is also found that the clusto-centric distance of LIRGs increases with the increase of the halo mass of the system they belong to. This is observed especially in the very few cases where the size of their halo is in transition from group size to cluster size halo.

5.2 The chemical abundance of dwarf irregular galaxies

This work also determined the metallicity of three dIrr galaxies and studied their metallicity-luminosity relationships as well as the metallicity gradient in one of the galaxies. The work was carried out as a pilot project to examine the capabilities of Robert Stobie Spectrograph (RSS) on SALT for future projects with bigger samples. The data were acquired during the commissioning phase of SALT, when RSS was having a throughput shortfall.

The result revealed that two of the three galaxies fit well to an already established metallicity-luminosity relationship for dIrr galaxies. This implies that they have star formation history measured in terms of their oxygen abundance is normal for their luminosity. However, the third galaxy exhibits a metallicity much smaller for its magnitude. If this result is true, it means that this galaxy follows a different star formation history despite being a dIrr galaxy.

The third galaxy has an edge-on orientation with very extended HII regions. This allowed us to carry out a metallicity gradient investigation. Since [OIII]λ4363 is observed only at the centre of the galaxy, the direct method of abundance determination is used only at the centre and at the other parts the R_{23} method was used.The result showed that there is a metallicity gradient with a slope -0.12 dex/ kpc. There is a possibility that this result is affected by the background and/or foreground contamination within the galaxy itself and it is important to take that effect into account to validate the calculated gradient. If, however, a correction for the contamination is made, one expects an even steeper slope as the correction is much larger at the centre than at the outskirts because of the orientation of the galaxy. The implication of this result is that star formation throughout the galaxy is not uniform.

Generally, given the RSS throughput problem at the time when the observations for this study were made, the results are encouraging to make use of RSS for similar future projects.

6 Future prospects

6.1 Metallicity of LIRGs

The metallicities of IR galaxies, especially LIRGs, are poorly studied to date. This is partly because (U)LIRGs are note very bright in the optical and it is essential to use large telescopes, such as the 10m class telescope like SALT, in order to get good quality spectroscopic data to perform detailed abundance analysis beyond just using simple empirical bright-line relations. The few works done so far found that the nuclear metallicities of (U)LIRGs are underabundant by a factor of two in average (Liang et al. 2004, Rupke et al. 2008) compared to other galaxies of similar luminosity and mass. This is interpreted in the studies as being due to interaction processes, where the high rate of mixing of interstellar material has a significant impact on the metallicity of the resulting system. These works concentrate on observations acquired through either long-slit or single-aperture spectrographs which do not allow in-depth investigations of the different spatial components of the (U)LIRGs, which could be achieved by analyzing larger sets of HII regions per galaxy. These latter kinds of studies would be very important in the case of (U)LIRGs because their chemical abundances in both the nuclear and peripheral regions would be expected to be strongly tied to their kinematics and morphological properties. Understanding this important point, there are already some on-going surveys making use of Integral Field Spectroscopy to study chemical abundances spatially in star-forming nearby spirals (Rosales-Ortega et al. 2011) and in (U)LIRGS in particular (Arribas et al. 2008, García-Marín et al. 2009). The surveys aim to eventually address the connection of internal structure, kinematics and their metallicity of (U)LIRGs in great detail.

(U)LIRGs often being merging systems, it should be expected that they would exhibit similar metallicity gradients than other merging and interacting galaxies. Interacting systems are expected to have shallower abundance gradients than their progenitor galaxies due to low metallicity material from the outskirts being pushed to the centre during the interaction/merging process (Rupke et al. 2008, Kewley et al. 2006). A recent work by Rupke et al. (2010), for example, compared the metallicities of isolated spirals and merging systems and found that the gradients of interacting systems is only half of that of isolated spirals. Other studies, moreover, found no oxygen abundance gradients at all in the tidal features of interacting galaxies, suggesting stronger level of mixing which would wipe out all inhomogeneities of the systems (e.g. Chien et al. 2007). Similar trend of weakened abundance gradients are also observed in barred galaxies because of gas motions induced by bar activities (Zaritsky et al. 1994, Roy & Walsh 1997, Vila-Costas & Edmunds 1992). Gradients of bar origin are often very shallow and truncated compared to merger induced gradients (Dutil & Roy 1999).

The degree of low metallicity material being pushed to the central regions of merging (U)LIRG system depends strongly on how strong the merger is. Since the strength of the merger might also be correlated to the L_{IR} output of the system, it might be possible to see a trend between metallicity of (U)LIRGs and their L_{IR} output. The expected trend would be a metallicity that is inversely proportional to the L_{IR}. This is planned to be investigated in the future.

When it comes to the mass/luminosity-metallicity (M/L-Z) relationship of interacting galaxies, they are seen to experience a metallicity offset of few dex at a given mass/luminosity in the lower direction (Ellison et al. 2008, Kewley et al. 2006). For example Kewley et al. (2006) showed that galaxy pairs with projected separations less than 20 kpc have systematically lower (central) metallicity by about 0.2 dex on average than field galaxies of the same luminosity. Rupke et al. (2010) also found similar results for strongly interacting galaxies. This underabundance explains the scatter observed in the M-L relationships of the general populations of galaxies, both at high and low mass ends (Ekta & Chengalur 2010, Peeples et al. 2009). Again, given the interacting and merging nature of (U)LIRGs, one expects (U)LIRGs to follow similar M/L-Z trend with other interacting or merging galaxies. A study conducted on local (U)LIRGs by Rupke et al. (2008) concluded that (U)LIRGs have lower oxygen abundances compared to galaxies of the same luminosity and mass. The lower central metallicity of (U)LIRGs is attributed to the radial inflow of gas to the nuclear region due to merging.

Understanding the metallicities in (U)LIRGs can give important insights into the formation and evolution processes of (U)LIRGs. There are many issues that are not yet understood about the detailed process of gas motion and its consequences leading to the onset of a starburst and nuclear activity in (U)LIRGs (e.g. Hopkins et al. 2006). In contrast to the work done on metallicities of optically identified interacting and merging systems, not many aspects of the metallicities of (U)LIRGs are explored. Even though (U)LIRGs fall under the larger class of interacting galaxies, the work in this thesis revealed that there is indeed an important and

fundamental difference between (U)LIRGs and other types of galaxies – a fundamental difference seen in their divergent environmental characteristics.

Though we found in Chapter 2 that the luminosity point ($L_{IR} \sim 10^{11} L_{\odot}$) is a special luminosity level among IR galaxies, the physical origin of this point remains unclear. To explore the reasons for the break point further, we need to find whether the density break seen at this luminosity extends to other properties of IR galaxies. What would those properties be? Does the correlation between SF and environment for LIRGs extend to the entire ULIRG regime or does it follow a different trend? If so, what are the implications on the star formation mechanism of ULIRGs? All these questions need to be addressed if one wants to grasp the broader picture of the formation, evolution and other properties of IR galaxies, especially LIRGs and ULIRGs.

Based on the discussion above, it makes sense to start the effort in understanding the above questions by examining whether the break seen at $L_{IR} \sim 10^{11} L_{\odot}$ in density-L_{IR} relationship extends to metallicities, and to see how these metallicites correlate with the environment. By studying the spatially resolved metallicity of IR galaxies both above and below the LIRG classification we will investigate whether the environmental divide extends to metallicity gradients of IR-selected galaxies. If differences in metallicities, whether nuclear or gradient, or both, exist, we will correlate these to luminosities, SF and merger stage characteristics, and kinematic states of the IR-selected galaxies. Furthermore, it is possible to develop a way of calibrating the level of interaction using the level of mixing and in-fall of material in such galaxies derived from metallicity gradients.

We already have an approved project to use SALT for this particular future work. We have proposed to take moderate resolution spectra of IR galaxies both with $L_{IR} \geq 10^{11} L_{\odot}$ and $L_{IR} \leq 10^{11} L_{\odot}$. Though the nature of the dIrr galaxies is different to that of LIRGs and ULIRGs, with the pilot project we have made in this work, we have shown that it is possible to use RSS for similar studies. With RSS, we can cover wavelength ranges from the blue end to the red to pick up the most important emission lines such as [OII]λ3727, [OIII]λ4959, [$OIII$]λ5007 and the hydrogen recombination lines that can be used in the direct method of abundance calculations.

We can also do Fabry-Perot spectroscopy using SALT on a few selected galaxies in order to do a spatial mapping of two or three different emission lines separately with a higher spectral resolution. This would complement the long-slit and MOS spectroscopy which covers the full spectral range needed for proper abundance analysis, by also getting a full spatial map over the whole area of the interacting system, with more accurate kinematics, and abundance maps derived using empirical relations, but now calibrated with our own overlapping long-slit or MOS data.

In summary, as an immediate objective we would in particular answer the following questions with our observations: i) Does the M/L-Z relationship that is observed in (U)LIRGs have anything to do with their L_{IR} activity? And if it does correlate, what does it mean? ii) Does the gradient observed in (U)LIRGs correlate with L_{IR}? It is expected that such correlations exists because the M/L-Z relation and gradients are driven by the inflow of gas towards the

nuclear region, and the same activity also drives the L_{IR} activity, at least to some extent.

Finally, in the longer term, there are other science questions related to the results of this thesis in Chapters 2 and 3, combined with the metallicity aspect, that would be relevant to investigate further. Are there any similarities between high and low redshift (U)LIRGs in terms of their metallicity? The work in Chapter 2 found considerable similarity in the SFR-density trend of local LIRGs and the high redshift Universe (Cooper et al. 2008). We found that the SFR of LIRGs is proportional to their environment. This relationship between SF and environment of LIRGs is similar to what is witnessed for blue cloud galaxies at $z \sim 1$. These similarities suggest that the formation mechanism of local LIRGs and $z \sim 1$ blue cloud galaxies might be similar, that the two populations may have formed via similar processes but at different times. Alternatively, local LIRGs might be survivors of whatever process transformed $z \sim 1$ blue cloud galaxies into the present red sequence galaxies. A comparative study of M/L-Z and the abundance gradients between high and low redshift LIRGs might thus be ideal in exploring further whether there is any evolutionary connection between high and low redshift LIRGs. If there will be any, then the two population of LIRGs must experience similar trend that could trace back its origin on the same mechanism, i.e., interaction or mergiger.

These kind of studies could also shed light to the redshift evolution of the SFR in the Universe, an important topic in modern cosmology. It is conceivable that the redshift evolution of the M/L-Z and abundance gradient studies can help in understanding what mechanism is responsible in driving star formation at different redshifts in the history of the Universe. If interaction is dominant, one then expects to see a shallow abundance gradient and an offsetted M/L-Z relations to the negative direction will be observed. However, if quiescent form of star formation (such as star formation seen in "normal" spirals), one expects the above relation to show no divergence from what is expected from spirals. There are already some works that look at the metallicity of star forming galaxies at high redshift Universe (see a recent review by Erb 2010) but these works neither look at the extreme form of star formation that is responsible for the big portion of the star formation budget of the Universe at all nor they do investigate the issue in depth (e.g. Rich et al. 2011).

6.2 Metallicity of dIrr and a spectroscopic follow-up study of ESO 074-G015

The pilot study done on the chemical abundances of the three dIrr galaxies (see Chapter 5) showed that it is possible to use the RSS instrument on SALT to carry out a similar but a larger scale project. The work started in this PhD thesis could investigate various aspects of dIrr galaxies, including the influence of environment on their star formation in a well defined sample constructed by examining close pair fractions and by looking for evidence of close by neighbors and causes for their morphological disturbances. A project like this would benefit from the deep

imaging capabilities of SALT.

A strong abundance gradient is a very rare phenomenon among dIrr galaxies, they are normally thought as being chemically very homogeneous (Kobulnicky & Skillman 1996, Kunth & Östlin 2000). The homogeneity is thought to be the result of their chaotic interstellar medium, resulting from e.g. stellar and supernova feedback processes (Kobulnicky et al. 1999), which erase any inhomogeneities due to freshly produced metals in time scales of less than 10^8 years (e.g. Roy & Kunth 1995, Recchi et al. 2006). Nevertheless, the pilot project in Chapter 4 revealed that ESO 074-G015 dIrr galaxy has a strong abundance gradient that is similar to the only previously observed such case in NGC 6822 (Lee et al. 2006). Whether or not gradients or full homogeneity are seen, it has to be a result of how star formation, and hence metal production, has progressed in the galaxies. The chemical homogeneity of dwarfs must, then, have significant relevance to the physics of the metal mixing and cooling processes, in addition to their star formation histories, and thus simple observations of whether or not dwarf irregulars are chemically homogeneous or not can already constrain these models (see e.g. Magrini et al. 2007).

With the questions above in mind, we would continue our dIrr study with SALT as follows:

- To first make a follow-up spectroscopic study and make sure that the abundance gradient determined in the pilot project of this thesis can be verified by more detailed and deeper data over more slit-positions throughout the galaxy.
- To study the kinematics of the interstellar medium in order to see if there is indeed any deviation from the usual chaotic interstellar medium in dIrr galaxies. If the level of ISM movements and mixing in the galaxy is as large as what is observed in the majority of dIrrs, one can deduce that there should be another physical mechanism operating *against* the mixing processes to produce the observed gradient.

To tackle these and similar questions regarding the nature of ESO 074-G015, the collecting area and spectroscopic capabilities of SALT are ideal. High resolution spectroscopy using RSS enables the examination of the details of the kinematics of the galaxy. These future projects will benefit from lessons and skills learned in Chapter 4 of this thesis, together with the different tools we have developed for the metallicity and abundance calculation.

6.3 The connection of environment and star formation in ULIRGs

As one can note, the environmental study in this thesis in Chapters 2 and 3 did not go much above the LIRG regime to study ULIRGs. It is, however, worth trying to extend the same study well above the ULIRG limit, since this way one can get a more general and complete picture of the nature and evolution of star formation including the most extreme cases. Though such kind of studies are hampered with the unavailability of deep IR surveys and related redshifts, there are at least two possibilities to easily extend the present work. Firstly, by merely including

the photometric redshifts of the various IRAS surveys, we would have an IR galaxy sample four or five times larger extending to both higher redshift and luminosity. We did not use the photometric redshifts in this work because we wanted to be certain of the results, but the present work can now be used as a calibrator. Secondly, the recent AKARI[1] mission (Murakami et al. 2007) has provided a more accurate (spatial resolution and flux) all-sky far-infrared sample of galaxies (see e.g. Totani et al. 2011) which should soon be publicly available for cross-correlations with both spectroscopic and photometric redshifts from elsewhere.

[1] AKARI is a 68.5 cm telescope cooled down to 6K, and observe in the wavelength range from 1.7 (near-infrared) to 180 (far-infrared) μm

Bibliography

Aller L. H., ed. 1984, Physics of thermal gaseous nebulae Vol. 112 of Astrophysics and Space Science Library

Armus L., Mazzarella J. M., Evans A. S., Surace J. A., Sanders D. B., Iwasawa K., Frayer D. T., Howell J. H., Chan B., Petric A., Vavilkin T., Kim D. C., Haan S., Inami H., Murphy E. J., Appleton P. N., Barnes J. E., Bothun G., Bridge C. R., 2009, , 121, 559

Arribas S., Colina L., Monreal-Ibero A., Alfonso J., García-Marín M., Alonso-Herrero A., 2008, A&A, 479, 687

Barnes J. E., Hernquist L., 1996, ApJ, 471, 115

Becklin E. E., Neugebauer G., 1969, ApJL, 157, L31

Bell E. F., de Jong R. S., 2001, ApJ, 550, 212

Bell E. F., Papovich C., Wolf C., Le Floc'h E., Caldwell J. A. R., Barden M., Egami E., McIntosh D. H., Meisenheimer K., Pérez-González P. G., Rieke G. H., Rieke M. J., Rigby J. R., Rix H., 2005, ApJ, 625, 23

Bender R., Burstein D., Faber S. M., 1992, ApJ, 399, 462

Berlind A. A., 2006, in Bulletin of the American Astronomical Society Vol. 38 of Bulletin of the American Astronomical Society, The Clustering of Galaxy Groups: Dependence on Mass and Other Properties. p. 1075

Berlind A. A., Blanton M. R., Hogg D. W., Weinberg D. H., Davé R., Eisenstein D. J., Katz N., 2005, ApJ, 629, 625

Berlind A. A., Frieman J., Weinberg D. H., Blanton M. R., Warren M. S., Abazajian K., Scranton R., Hogg D. W., Scoccimarro R., Bahcall N. A., Brinkmann J., Gott III J. R., Kleinman S. J., 2006, ApJS, 167, 1

Berlind A. A., Frieman J., Weinberg D. H., Blanton M. R., Warren M. S., Abazajian K., Scranton R., Hogg D. W., Scoccimarro R., Bahcall N. A., Brinkmann J., Gott III J. R., Kleinman S. J., Krzesinski J., Lee B. C., 2006, ApJS, 167, 1

Berlind A. A., Weinberg D. H., 2002, ApJ, 575, 587

Binney J., Tremaine S., 1987, Natur, 326, 219

Blain A. W., Smail I., Ivison R. J., Kneib J., Frayer D. T., 2002, , 369, 111

Blanton M. R., Eisenstein D., Hogg D. W., Zehavi I., 2006, ApJ, 645, 977

Blanton M. R., Hogg D. W., Bahcall N. A., Baldry I. K., Brinkmann J., Csabai I., Eisenstein D., Fukugita M., Gunn J. E., Ivezić Ž., Lamb D. Q., 2003, ApJ, 594, 186

Bresolin F., Garnett D. R., Kennicutt Jr. R. C., 2004, ApJ, 615, 228

Bresolin F., Ryan-Weber E., Kennicutt R. C., Goddard Q., 2009, ApJ, 695, 580

Bridge C. R., Appleton P. N., Conselice C. J., Choi P. I., Armus L., Fadda D., Laine S., Marleau F. R., Carlberg R. G., Helou G., Yan L., 2007, ApJ, 659, 931

Brinchmann J., Charlot S., White S. D. M., Tremonti C., Kauffmann G., Heckman T., Brinkmann J., 2004, MNRAS, 351, 1151

Brocklehurst M., 1971, MNRAS, 153, 471

Brosch N., Bar-Or C., Malka D., 2006, MNRAS, 368, 864

Buckley D. A. H., Cottrell P. L., Nordsieck K. H., O'Donoghue D. E., Williams T. B., 2004, in A. F. M. Moorwood & M. Iye ed., Society of Photo-Optical Instrumentation Engineers (SPIE) Conference Series Vol. 5492 of Presented at the Society of Photo-Optical Instrumentation Engineers (SPIE) Conference, The first-generation instruments for the Southern African Large Telescope (SALT). pp 60–74

Buckley D. A. H., Hearnshaw J. B., Nordsieck K. H., O'Donoghue D., 2003, in P. Guhathakurta ed., Society of Photo-Optical Instrumentation Engineers (SPIE) Conference Series Vol. 4834 of Presented at the Society of Photo-Optical Instrumentation Engineers (SPIE) Conference, Science drivers and first generation instrumentation for the Southern African Large Telescope (SALT). pp 264–275

Bundy K., Fukugita M., Ellis R. S., Kodama T., Conselice C. J., 2004, ApJL, 601, L123

Burbidge G. R., Stein W. A., 1970, ApJ, 160, 573

Burgh E. B., Nordsieck K. H., Kobulnicky H. A., Williams T. B., O'Donoghue D., Smith M. P., Percival J. W., 2003, in M. Iye & A. F. M. Moorwood ed., Society of Photo-Optical Instrumentation Engineers (SPIE) Conference Series Vol. 4841 of Presented at the Society of Photo-Optical Instrumentation Engineers (SPIE) Conference, Prime Focus Imaging Spectrograph for the Southern African Large Telescope: optical design. pp 1463–1471

Caldwell N., Bothun G. D., 1987, AJ, 94, 1126

Caputi K. I., Lilly S. J., Aussel H., Le Floc'h E., Sanders D., Maier C., Frayer D., Carollo C. M., Contini T., Kneib J.-P., 2009, ApJ, 707, 1387

Cedrés B., Urbaneja M. A., Cepa J., 2004, A&A, 422, 511

Chary R., Elbaz D., 2001, ApJ, 556, 562

Chien L.-H., Barnes J. E., Kewley L. J., Chambers K. C., 2007, ApJL, 660, L105

Cooper M. C., Newman J. A., Madgwick D. S., Gerke B. F., Yan R., Davis M., 2005, ApJ, 634, 833

Cooper M. C., Newman J. A., Weiner B. J., Yan R., Willmer C. N. A., Bundy K., Coil A. L., Conselice C. J., Davis M., Faber S. M., Gerke B. F., Guhathakurta P., Koo D. C., Noeske K. G., 2008, MNRAS, 383, 1058

Cowie L. L., Barger A. J., Fomalont E. B., Capak P., 2004, ApJL, 603, L69

Croxall K. V., van Zee L., Lee H., Skillman E. D., Lee J. C., Côté S., Kennicutt R. C., Miller B. W., 2009, ApJ, 705, 723

Cucciati O., Iovino A., Marinoni C., Ilbert O., Bardelli S., Franzetti P., Le Fèvre O., Pollo A., Zamorani G., Cappi A., 2006, A&A, 458, 39

de Ravel L., Le Fèvre O., Tresse L., Bottini D., Garilli B., Le Brun V., Maccagni D., Scaramella R., Scodeggio M., Vettolani G., Zanichelli A., Adami C., Arnouts S., Bardelli S., Bolzonella M., 2009, A&A, 498, 379

Debuhr J., Quataert E., Ma C., 2010, MNRAS, p. 1881

Dekel A., Silk J., 1986, ApJ, 303, 39

Denicoló G., Terlevich R., Terlevich E., 2002, in W. J. Henney, J. Franco, & M. Martos ed., Revista Mexicana de Astronomia y Astrofisica Conference Series Vol. 12 of Revista Mexicana de Astronomia y Astrofisica Conference Series, New Light on the Search for Low-Metallicity Galaxies. pp 257–257

Di Matteo P., Combes F., Melchior A., Semelin B., 2007, A&A, 468, 61

Díaz A. I., Castellanos M., Terlevich E., Luisa García-Vargas M., 2000, MNRAS, 318, 462

Dressler A., 1980, ApJ, 236, 351

Duc P., Fadda D., Poggianti B., Elbaz D., Biviano A., Flores H., Moorwood A., Franceschini A., Cesarsky C., 2004, in A. Diaferio ed., IAU Colloq. 195: Outskirts of Galaxy Clusters: Intense Life in the Suburbs Luminous infrared starbursts in a cluster of galaxies. pp 347–351

Dutil Y., Roy J.-R., 1999, ApJ, 516, 62

Efstathiou G., Silk J., 1983, , 9, 1

Eke V. R., Baugh C. M., Cole S., Frenk C. S., Norberg P., Peacock J. A., Baldry I. K., Bland-Hawthorn J., Bridges T., Cannon R., Colless M., Collins C., Couch W., Dalton G., de Propris R., Driver S. P., Efstathiou G., 2004, MNRAS, 348, 866

Ekta B., Chengalur J. N., 2010, MNRAS, 406, 1238

Elbaz D., Daddi E., Le Borgne D., Dickinson M., Alexander D. M., Chary R., Starck J., Brandt W. N., Kitzbichler M., MacDonald E., Nonino M., Popesso P., Stern D., Vanzella E., 2007, A&A, 468, 33

Ellison S. L., Patton D. R., Simard L., McConnachie A. W., 2008, AJ, 135, 1877

Ellison S. L., Patton D. R., Simard L., McConnachie A. W., Baldry I. K., Mendel J. T., 2010, MNRAS, 407, 1514

Erb D. K., 2010, in K. Cunha, M. Spite, & B. Barbuy ed., IAU Symposium Vol. 265 of IAU Symposium, Chemical Abundances in Star-Forming Galaxies at High Redshift. pp 147–154

Erdoğdu P., Lahav O., Huchra J. P., Colless M., Cutri R. M., Falco E., George T., Jarrett T., Jones D. H., Macri L. M., Mader J., Martimbeau N., Pahre M. A., Parker Q. A., Rassat A., Saunders W., 2006, MNRAS, 373, 45

Esteban C., García López R., Herrero A., Sánchez F., eds, 2004, Cosmochemistry. The melting pot of the elements

Evrard A. E., 2004, in J. S. Mulchaey, A. Dressler, & A. Oemler ed., Clusters of Galaxies: Probes of Cosmological Structure and Galaxy Evolution Galaxy Clusters as Probes of Cosmology and Astrophysics. p. 1

Farouki R., Shapiro S. L., 1981, ApJ, 243, 32

Feldmann R., Carollo C. M., Mayer L., Renzini A., Lake G., Quinn T., Stinson G. S., Yepes G., 2010, ApJ, 709, 218

Ferland G., 1995, in R. Williams & M. Livio ed., The Analysis of Emission Lines: A Meeting in Honor of the 70th Birthdays of D. E. Osterbrock M. J. Seaton The Lexington Benchmarks for Numerical Simulations of Nebulae. p. 83

Feruglio C., Aussel H., Le Floc'h E., Ilbert O., Salvato M., Capak P., Fiore F., Kartaltepe J., Sanders D., Scoville N., Koekemoer A. M., Ideue Y., 2010, ApJ, 721, 607

Finn R. A., Desai V., Rudnick G., Poggianti B., Bell E. F., Hinz J., Jablonka P., Milvang-Jensen B., Moustakas J., Rines K., Zaritsky D., 2010, ApJ, 720, 87

Finn R. A., Zaritsky D., McCarthy Jr. D. W., Poggianti B., Rudnick G., Halliday C., Milvang-Jensen B., Pelló R., Simard L., 2005, ApJ, 630, 206

Fisher J. R., Tully R. B., 1975, A&A, 44, 151

García-Marín M., Colina L., Arribas S., Monreal-Ibero A., 2009, A&A, 505, 1319

Garnett D. R., 1992, AJ, 103, 1330

Garnett D. R., 2004, in C. Esteban, R. García López, A. Herrero, & F. Sánchez ed., Cosmochemistry. The melting pot of the elements Element abundances in nearby galaxies. pp 171–216

Geller M. J., Huchra J. P., 1983, ApJS, 52, 61

Glazebrook K., Peacock J. A., Miller L., Collins C. A., 1995, MNRAS, 275, 169

Gómez P. L., Nichol R. C., Miller C. J., Balogh M. L., Goto T., Zabludoff A. I., Romer A. K., Bernardi M., Sheth R., Hopkins A. M., Castander F. J., Connolly A. J., Schneider D. P., Brinkmann J., Lamb D. Q., SubbaRao M., York D. G., 2003, ApJ, 584, 210

Gonzalez-Delgado R. M., Perez E., Tenorio-Tagle G., Vilchez J. M., Terlevich E., Terlevich R., Telles E., Rodriguez-Espinosa J. M., Mas-Hesse M., Garcia-Vargas M. L., Diaz A. I., Cepa J., Castaneda H., 1994, ApJ, 437, 239

Graham A. W., 2005, in H. Jerjen & B. Binggeli ed., IAU Colloq. 198: Near-fields cosmology with dwarf elliptical galaxies Structural properties of dwarf ellipticals and the connection with (ordinary) elliptical galaxies. pp 303–310

Grebel E. K., Gallagher III J. S., Harbeck D., 2003, AJ, 125, 1926

Gunn J. E., Gott III J. R., 1972, ApJ, 176, 1

Heavens A., Panter B., Jimenez R., Dunlop J., 2004, Natur, 428, 625

Hermit S., Santiago B. X., Lahav O., Strauss M. A., Davis M., Dressler A., Huchra J. P., 1996, MNRAS, 283, 709

Hirashita H., 2000, PASJ, 52, 107

Hogg D. W., 1999, arXiv:astro-ph/9905116

Holden B. P., Illingworth G. D., Franx M., Blakeslee J. P., Postman M., Kelson D. D., van der Wel A., Demarco R., Magee D. K., Tran K., Zirm A., Ford H., Rosati P., Homeier N., 2007, ApJ, 670, 190

Holmberg E., 1958, Meddelanden fran Lunds Astronomiska Observatorium Serie II, 136, 1

Hopkins P. F., Hernquist L., Cox T. J., Di Matteo T., Robertson B., Springel V., 2006, ApJS, 163, 1

Howell J. H., Armus L., Mazzarella J. M., Evans A. S., Surace J. A., Sanders D. B., Petric A., Appleton P., Bothun G., Bridge C., Chan B. H. P., Charmandaris V., Frayer D. T., Haan S., Inami H., 2010, ApJ, 715, 572

Hubble E. P., 1926, ApJ, 64, 321

Hubble E. P., 1936, Realm of the Nebulae. Yale University Press

Huchra J. P., Geller M. J., 1982, ApJ, 257, 423

Hunter D. A., Wilcots E. M., 2002, AJ, 123, 2449

Hwang H. S., Elbaz D., Lee J. C., Jeong W., Park C., Lee M. G., Lee H. M., 2010, arXiv:astro-ph/1006.2166

Ilbert O., Lauger S., Tresse L., Buat V., Arnouts S., Le Fèvre O., Burgarella D., Zucca E., Bardelli S., Zamorani G., Bottini D., Garilli B., Le Brun V., Maccagni D., 2006, A&A, 453, 809

Izotov Y. I., Stasińska G., Meynet G., Guseva N. G., Thuan T. X., 2006, A&A, 448, 955

Izotov Y. I., Thuan T. X., Lipovetsky V. A., 1994, ApJ, 435, 647

Jarrett T. H., Chester T., Cutri R., Schneider S., Skrutskie M., Huchra J. P., 2000, AJ, 119, 2498

Jenkins A., Frenk C. S., White S. D. M., Colberg J. M., Cole S., Evrard A. E., Couchman H. M. P., Yoshida N., 2001, MNRAS, 321, 372

Jones D. H., Read M. A., Saunders W., Colless M., Jarrett T., Parker Q. A., Fairall A. P., Mauch T., Sadler E. M., Watson F. G., Burton D., Campbell L. A., Cass P., Croom S. M., et al. 2009, MNRAS, 399, 683

Joseph R. D., 1989, in J. E. Beckman & B. E. J. Pagel ed., Evolutionary Phenomena in Galaxies Evolutionary effects of interactions between galaxies. pp 441–452

Kaisin S. S., Kasparova A. V., Knyazev A. Y., Karachentsev I. D., 2007, Astronomy Letters, 33, 283

Kauffmann G., White S. D. M., Guiderdoni B., 1993, MNRAS, 264, 201

Kauffmann G., White S. D. M., Heckman T. M., Ménard B., Brinchmann J., Charlot S., Tremonti C., Brinkmann J., 2004, MNRAS, 353, 713

Kennicutt R. C., Hao C., Calzetti D., Moustakas J., Dale D. A., Bendo G., Engelbracht C. W., Johnson B. D., Lee J. C., 2009, ApJ, 703, 1672

Kennicutt Jr. R. C., 1998a, ARA&A, 36, 189

Kennicutt Jr. R. C., 1998b, ApJ, 498, 541

Kennicutt Jr. R. C., Bresolin F., Garnett D. R., 2003, ApJ, 591, 801

Kewley L. J., Geller M. J., Barton E. J., 2006, AJ, 131, 2004

Kewley L. J., Jansen R. A., Geller M. J., 2005, , 117, 227

Kleinmann D. E., Low F. J., 1970, ApJL, 159, L165

Kleinmann S. G., Hamilton D., Keel W. C., Wynn-Williams C. G., Eales S. A., Becklin E. E., Kuntz K. D., 1988, ApJ, 328, 161

Kniazev A. Y., Pustilnik S. A., Grebel E. K., Lee H., Pramskij A. G., 2004, ApJS, 153, 429

Kniazev A. Y., Zijlstra A. A., Grebel E. K., Pilyugin L. S., Pustilnik S., Väisänen P., Buckley D., Hashimoto Y., Loaring N., Romero E., Still M., Burgh E. B., Nordsieck K., 2008, MNRAS, 388, 1667

Kobulnicky H. A., Kennicutt Jr. R. C., Pizagno J. L., 1999, ApJ, 514, 544

Kobulnicky H. A., Nordsieck K. H., Burgh E. B., Smith M. P., Percival J. W., Williams T. B., O'Donoghue D., 2003, in M. Iye & A. F. M. Moorwood ed., Society of Photo-Optical Instrumentation Engineers (SPIE) Conference Series Vol. 4841 of Presented at the Society of Photo-Optical Instrumentation Engineers (SPIE) Conference, Prime focus imaging spectrograph for the Southern African large telescope: operational modes. pp 1634–1644

Kobulnicky H. A., Skillman E. D., 1996, ApJ, 471, 211

Kormendy J., 1985, ApJ, 295, 73

Kormendy J., Djorgovski S., 1989, ARA&A, 27, 235

Kunth D., Östlin G., 2000, A&ARV, 10, 1

Kurucz R. L., 1979, ApJS, 40, 1

Laag E. A., 2006, in Bulletin of the American Astronomical Society Vol. 38 of Bulletin of the American Astronomical Society, The Extended Environments of ULIRGS and LIRGS: Clusters in Formation. p. 1198

Lahav O., Suto Y., 2004, Living Reviews in Relativity, 7, 8

Larson R. B., 1974, MNRAS, 169, 229

Le Floc'h E., Papovich C., Dole H., Bell E. F., Lagache G., Rieke G. H., Egami E., Pérez-González P. G., Alonso-Herrero A., Rieke M. J., Blaylock M., Engelbracht C. W., Gordon K. D., Hines D. C., 2005, ApJ, 632, 169

Lee H., McCall M. L., Richer M. G., 2003, AJ, 125, 2975

Lee H., Skillman E. D., Venn K. A., 2006, ApJ, 642, 813

Lee H., Zucker D. B., Grebel E. K., 2007, MNRAS, 376, 820

Lemonon L., Pierre M., Cesarsky C. J., Elbaz D., Pello R., Soucail G., Vigroux L., 1998, A&A, 334, L21

Lemson G., Kauffmann G., 1999, MNRAS, 302, 111

Lequeux J., Peimbert M., Rayo J. F., Serrano A., Torres-Peimbert S., 1979, A&A, 80, 155

Li I. H., Glazebrook K., Gilbank D., Balogh M., Bower R., Baldry I., Davies G., Hau G., McCarthy P., 2011, MNRAS, 411, 1869

Liang Y. C., Hammer F., Flores H., Elbaz D., Marcillac D., Cesarsky C. J., 2004, A&A, 423, 867

Lilly S. J., Le Fevre O., Hammer F., Crampton D., 1996, ApJL, 460, L1

Lin L., Patton D. R., Koo D. C., Casteels K., Conselice C. J., Faber S. M., Lotz J., Willmer C. N. A., Hsieh B. C., Chiueh T., Newman J. A., Novak G. S., Weiner B. J., Cooper M. C., 2008, ApJ, 681, 232

Loveday J., Maddox S., Efstathiou G., Peterson B., 1995, in S. J. Maddox & A. Aragon-Salamanca ed., Wide Field Spectroscopy and the Distant Universe Variation of Galaxy Clustering with Morphology and Luminosity in the Stromlo-APM Redshift Survey. p. 157

Ma B., Meng K., Pan J., Huang J., Feng L., 2009, Research in Astronomy and Astrophysics, 9, 979

Mac Low M., Ferrara A., 1999, ApJ, 513, 142

Madau P., Pozzetti L., Dickinson M., 1998, ApJ, 498, 106

Magrini L., Corbelli E., Galli D., 2007, A&A, 470, 843

Magrini L., Stanghellini L., Corbelli E., Galli D., Villaver E., 2010, A&A, 512, A63

Mamon G. A., 1992, ApJL, 401, L3

Mamon G. A., 2000, in F. Combes, G. A. Mamon, & V. Charmandaris ed., Dynamics of Galaxies: from the Early Universe to the Present Vol. 197 of Astronomical Society of the Pacific Conference Series, Theory of Galaxy Dynamics in Clusters and Groups. p. 377

Marcillac D., Rieke G. H., Papovich C., Willmer C. N. A., Weiner B. J., Coil A. L., Cooper M. C., Gerke B. F., Woo J., Newman J. A., Georgakakis A., Laird E. S., Nandra K., Fazio G. G., Huang J., Koo D. C., 2008, ApJ, 675, 1156

Martig M., Bournaud F., 2008, MNRAS, 385, L38

Martin P., Roy J.-R., 1992, ApJ, 397, 463

Mateo M. L., 1998, ARA&A, 36, 435

Melbourne J., Koo D. C., Le Floc'h E., 2005, ApJL, 632, L65

Melnick J., Mirabel I. F., 1990, A&A, 231, L19

Metzler C. A., White M., Norman M., Loken C., 1999, ApJ, 520, L9

Mihos J. C., 2004, Clusters of Galaxies: Probes of Cosmological Structure and Galaxy Evolution, p. 277

Mihos J. C., Hernquist L., 1994, ApJL, 431, L9

Mihos J. C., Hernquist L., 1996, ApJ, 464, 641

Mo H., van den Bosch F. C., White S., 2010, Galaxy Formation and Evolution. Cambridge University Press

Moiseev A. V., Pustilnik S. A., Kniazev A. Y., 2010, MNRAS, 405, 2453

Moore B., Katz N., Lake G., Dressler A., Oemler A., 1996, Natur, 379, 613

Moshir M., Kopman G., Conrow T. A. O., 1992, IRAS Faint Source Survey, Explanatory supplement version 2. California Institute of Technology

Murakami H., Baba H., Barthel P., Clements D. L., Cohen M., Doi Y., Enya K., Figueredo E., Fujishiro N., Fujiwara H., Fujiwara M., Garcia-Lario P., Goto T., Hasegawa S., Hibi Y., 2007, PASJ, 59, 369

Nardini E., Risaliti G., Salvati M., Sani E., Watabe Y., Marconi A., Maiolino R., 2009, MNRAS, 399, 1373

Navarro J. F., Frenk C. S., White S. D. M., 1997, ApJ, 490, 493

Negroponte J., White S. D. M., 1983, MNRAS, 205, 1009

Neugebauer G., Habing H. J., van Duinen R., Aumann H. H., Baud B., Beichman C. A., Beintema D. A., Boggess N., Clegg P. E., de Jong T., Emerson J. P., Gautier T. N., Gillett F. C., Harris S., et al. 1984, ApJL, 278, L1

Neugebauer G., Soifer B. T., Miley G., Habing H. J., Young E., Low F. J., Beichman C. A., Clegg P. E., Harris S., Rowan-Robinson M., 1984, ApJL, 278, L83

Noguchi M., Ishibashi S., 1986, MNRAS, 219, 305

O'Donoghue D., Buckley D. A. H., Balona L. A., Bester D., Botha L., Brink J., Carter D. B., Charles P. A., Christians A., Ebrahim F., Emmerich R., Esterhuyse W., Evans G. P., Fourie C., 2006, MNRAS, 372, 151

Oey M. S., Shields J. C., 2000, ApJ, 539, 687

Oliver S. J., Rowan-Robinson M., Broadhurst T. J., McMahon R. G., Saunders W., Taylor A., Lawrence A., Lonsdale C. J., Hacking P., Conrow T., 1996, MNRAS, 280, 673

Osterbrock D. E., 1989, Astrophysics of gaseous nebulae and active galactic nuclei. CA, University Science Books

Osterbrock D. E., Ferland G. J., 2006, Astrophysics of gaseous nebulae and active galactic nuclei. CA: University Science Books

Ostriker J. P., Peebles P. J. E., Yahil A., 1974, ApJL, 193, L1

Patel S. G., Holden B. P., Kelson D. D., Illingworth G. D., Franx M., 2009, ApJL, 705, L67

Peacock J. A., 2002, in S. Bonometto, V. Gorini, & U. Moschella ed., Modern Cosmology An introduction to the physics of cosmology. pp 9–107

Peeples M. S., Pogge R. W., Stanek K. Z., 2009, ApJ, 695, 259

Pérez-González P. G., Rieke G. H., Egami E., Alonso-Herrero A., Dole H., Papovich C., Blaylock M., Jones J., Rieke M., Rigby J., Barmby P., Fazio G. G., Huang J., Martin C., 2005, ApJ, 630, 82

Pilyugin L., 2003, ApSS, 284, 775

Pilyugin L. S., 2001, A&A, 374, 412

Pilyugin L. S., Mattsson L., 2010, arXiv:astro-phs/1011.1431

Pilyugin L. S., Vílchez J. M., Cedrés B., Thuan T. X., 2010, MNRAS, 403, 896

Pilyugin L. S., Vílchez J. M., Thuan T. X., 2010, ApJ, 720, 1738

Popescu C. C., Tuffs R. J., Dopita M. A., Fischera J., Kylafis N. D., Madore B. F., 2011, A&A, 527, A109

Pustilnik S. A., Kniazev A. Y., Lipovetsky V. A., Ugryumov A. V., 2001, A&A, 373, 24

Quintero A. D., Berlind A. A., Blanton M. R., Hogg D. W., 2005, arXiv:astro-ph/0512004

Ratag M. A., Pottasch S. R., Dennefeld M., Menzies J., 1997, A&AS, 126, 297

Recchi S., Hensler G., 2007, in E. Emsellem, H. Wozniak, G. Massacrier, J.-F. Gonzalez, J. Devriendt, & N. Champavert ed., EAS Publications Series Vol. 24 of EAS Publications Series, Star Formation Regulation, Gas Cycles and the chemical evolution of dwarf irregular galaxies. pp 101–106

Recchi S., Hensler G., Angeretti L., Matteucci F., 2006, A&A, 445, 875

Rees M. J., Silk J. I., Werner M. W., Wickramasinghe N. C., 1969, Natur, 223, 788

Reiprich T. H., Böhringer H., 2002, ApJ, 567, 716

Rhoads J. E., 1998, AJ, 115, 472

Rich J., Kewley L., Dopita M., 2011, in American Astronomical Society Meeting Abstracts #217 Vol. 43 of Bulletin of the American Astronomical Society, WiFeS GOALS: An IFU Study Of Metallicity, Shocks, And More In Nearby U/LIRGS. pp 114.05–+

Richer M. G., McCall M. L., 1995, ApJ, 445, 642

Richstone D. O., 1976, ApJ, 204, 642

Rieke G. H., Lebofsky M. J., 1986, ApJ, 304, 326

Roberts M. S., Haynes M. P., 1994, ARA&A, 32, 115

Roberts M. S., Rots A. H., 1973, A&A, 26, 483

Rosales-Ortega F. F., Díaz A. I., Kennicutt R. C., Sánchez S. F., 2011, MNRAS, pp 707–+

Rowan-Robinson M., Broadhurst T., Oliver S. J., Taylor A. N., Lawrence A., McMahon R. G., Lonsdale C. J., Hacking P. B., Conrow T., Saunders W., Ellis R. S., Efstathiou G. P., Condon J. J., 1991, Natur, 351, 719

Roy J., Walsh J. R., 1997, MNRAS, 288, 715

Roy J.-R., Kunth D., 1995, A&A, 294, 432

Rubin V. C., Thonnard N., Ford Jr. W. K., 1978, ApJL, 225, L107

Rupke D. S. N., Kewley L. J., Chien L.-H., 2010, ApJ, 723, 1255

Rupke D. S. N., Veilleux S., Baker A. J., 2008, ApJ, 674, 172

Ryan-Weber E. V., Meurer G. R., Freeman K. C., Putman M. E., Webster R. L., Drinkwater M. J., Ferguson H. C., Hanish D., Heckman T. M., Kennicutt Jr. R. C., Kilborn V. A., Knezek P. M., Koribalski B. S., 2004, AJ, 127, 1431

Sandage A., Binggeli B., 1984, AJ, 89, 919

Sanders D., Ishida C., 2004, in S. Aalto, S. Huttemeister, & A. Pedlar ed., The Neutral ISM in Starburst Galaxies Vol. 320 of Astronomical Society of the Pacific Conference Series, Luminous Infrared Galaxies: Optical Morphology and Photometry, Molecular Gas Masses, and Starburst/AGN Activity versus Infrared Luminosity. p. 230

Sanders D. B., Mirabel I. F., 1996, ARA&A, 34, 749

Saunders W., Sutherland W. J., Maddox S. J., Keeble O., Oliver S. J., Rowan-Robinson M., McMahon R. G., Efstathiou G. P., Tadros H., White S. D. M., Frenk C. S., Carramiñana A., Hawkins M. R. S., 2000, MNRAS, 317, 55

Savage B. D., Mathis J. S., 1979, ARA&A, 17, 73

Schmidt M., 1959, ApJ, 129, 243

Searle L., 1971, ApJ, 168, 327

Sheth K., Elmegreen D. M., Elmegreen B. G., Capak P., Abraham R. G., Athanassoula E., Ellis R. S., Mobasher B., Salvato M., Schinnerer E., Scoville N. Z., Spalsbury L., Strubbe L., Carollo M., Rich M., West A. A., 2008, ApJ, 675, 1141

Skillman E. D., Kennicutt R. C., Hodge P. W., 1989, ApJ, 347, 875

Skillman E. D., Terlevich R., Melnick J., 1989, MNRAS, 240, 563

Smith L. J., Norris R. P. F., Crowther P. A., 2002, MNRAS, 337, 1309

Sobral D., Best P., Smail I., Geach J., Cirasuolo M., Garn T., Dalton G. B., 2010, arXiv:astroph/1007.2642

Soifer B. T., Neugebauer G., Helou G., Lonsdale C. J., Hacking P., Rice W., Houck J. R., Low F. J., Rowan-Robinson M., 1984, ApJL, 283, L1

Soifer B. T., Rowan-Robinson M., Houck J. R., de Jong T., Neugebauer G., Aumann H. H., Beichman C. A., Boggess N., Clegg P. E., Emerson J. P., Gillett F. C., Habing H. J., Hauser M. G., Low F. J., Miley G., Young E., 1984, ApJL, 278, L71

Sparke L. S., Gallagher III J. S., 2007, Galaxies in the Universe: An Introduction. Cambridge University Press

Spergel D. N., Bean R., Doré O., Nolta M. R., Bennett C. L., Dunkley J., Hinshaw G., Jarosik N., Komatsu E., Page L., Peiris H. V., Verde L., Halpern M., Hill R. S., 2007, ApJS, 170, 377

Spitzer L., 1978, Physical processes in the interstellar medium. New York Wiley-Interscience

Stasińska G., 1990, A&AS, 83, 501

Stasińska G., 2002, arXiv:astro-ph/0207500

Stasińska G., Izotov Y., 2003, A&A, 397, 71

Tacconi L. J., Genzel R., Lutz D., Rigopoulou D., Baker A. J., Iserlohe C., Tecza M., 2002, ApJ, 580, 73

Tasca L. A. M., Kneib J.-P., Iovino A., Le Fèvre O., Kovač K., Bolzonella M., Lilly S. J., Abraham R. G., Cassata P., Cucciati O., Guzzo L., Tresse L., Zamorani G., 2009, A&A, 503, 379

Taylor A. N., Ballinger W. E., Heavens A. F., Tadros H., 2001, MNRAS, 327, 689

Toomre A., Toomre J., 1972, ApJ, 178, 623

Totani T., Takeuchi T. T., Nagashima M., Kobayashi M. A. R., Makiya R., 2011, ArXiv e-prints

Tran K.-V. H., Papovich C., Saintonge A., Brodwin M., Dunlop J. S., Farrah D., Finkelstein K. D., Finkelstein S. L., Lotz J., McLure R. J., Momcheva I., Willmer C. N. A., 2010, ApJL, 719, L126

Tremonti C. A., Heckman T. M., Kauffmann G., Brinchmann J., Charlot S., White S. D. M., Seibert M., Peng E. W., Schlegel D. J., Uomoto A., Fukugita M., Brinkmann J., 2004, ApJ, 613, 898

Trentham N., Mobasher B., 1998, MNRAS, 293, 53

Tresse L., Ilbert O., Zucca E., Zamorani G., Bardelli S., Arnouts S., Paltani S., Pozzetti L., Bottini D., Garilli B., Le Brun V., Le Fèvre O., 2007, A&A, 472, 403

Väisänen P., 1996, A&A, 315, 21

Väisänen P., Mattila S., Kniazev A., Adamo A., Efstathiou A., Farrah D., Johansson P. H., Östlin G., Buckley D. A. H., 2008, MNRAS, 384, 886

Väisänen P. S. M., 2001, PhD thesis, HELSINGIN YLIOPISTO (FINLAND)

Vega O., Clemens M. S., Bressan A., Granato G. L., Silva L., Panuzzo P., 2008, A&A, 484, 631

Veilleux S., Kim D., Sanders D. B., 1999, ApJ, 522, 113

Vila-Costas M. B., Edmunds M. G., 1992, MNRAS, 259, 121

Voit G. M., 2005, Reviews of Modern Physics, 77, 207

Wang L., Rowan-Robinson M., 2009, MNRAS, 398, 109

Warren M. S., Abazajian K., Holz D. E., Teodoro L., 2006, ApJ, 646, 881

White S. D. M., 1983, Natur, 302, 756

White S. D. M., Frenk C. S., 1991, ApJ, 379, 52

White S. D. M., Rees M. J., 1978, MNRAS, 183, 341

Whitford A. E., 1958, AJ, 63, 201

Wilcots E. M., Hunter D. A., 2002, AJ, 123, 1476

Willman B., Blanton M. R., West A. A., Dalcanton J. J., Hogg D. W., Schneider D. P., Wherry N., Yanny B., Brinkmann J., 2005, AJ, 129, 2692

Yin S. Y., Liang Y. C., Hammer F., Brinchmann J., Zhang B., Deng L. C., Flores H., 2007, A&A, 462, 535

Yoshii Y., Arimoto N., 1987, A&A, 188, 13

Young E., Low F. J., Soifer B. T., Neugebauer G., Rowan-Robinson M., Clegg P. E., Miley G., de Jong T., Gautier T. N., 1984, ApJL, 278, L75

Zabludoff A. I., Mulchaey J. S., 1998, ApJL, 498, L5

Zackrisson E., Bergvall N., Leitet E., 2008, ApJL, 676, L9

Zaritsky D., Kennicutt Jr. R. C., Huchra J. P., 1994, ApJ, 420, 87